

# SHORT COURSE I

**Advances in Multi-Neuronal Monitoring of Brain Activity**

Organized by Prakash Kara, PhD



# Short Course I

Advances in Multi-Neuronal Monitoring of Brain Activity

Prakash Kara, PhD

---

Please cite articles using the model:  
[AUTHOR'S LAST NAME, AUTHOR'S FIRST & MIDDLE INITIALS] (2014)  
[CHAPTER TITLE] In: *Advances in Multi-Neuronal Monitoring of Brain Activity*. (Prakash K, ed)  
pp. [xx-xx]. Washington, DC: Society for Neuroscience.

All articles and their graphics are under the copyright of their respective authors.

Cover graphics and design © 2014 Society for Neuroscience.

## SHORT COURSE I

### Advances in Multi-Neuronal Monitoring of Brain Activity

Organized by Prakash Kara, PhD

Friday, November 14

8:00 a.m.–6:00 p.m.

Location: Walter E. Washington Convention Center | Ballroom A | Washington, DC



TIME	AGENDA TOPICS	SPEAKER
7:30–8:00 a.m.	CHECK-IN	
8:00–8:10 a.m.	Opening Remarks	Prakash Kara, PhD <i>Medical University of South Carolina</i>
8:10–8:55 a.m.	Fluorescent Genetically Encoded Sensors for Imaging Neural Activity	Douglas Kim, PhD <i>Howard Hughes Medical School</i>
8:55–9:40 a.m.	Simultaneous Two-Photon Calcium Imaging of Entire Cortical Columns in the Mouse	Mark Andermann, PhD <i>Harvard Medical School</i>
9:40–9:55 a.m.	MORNING BREAK	
9:55–10:40 a.m.	Two-Photon Calcium Imaging in the Macaque Monkey	Kristina Nielsen, PhD <i>Johns Hopkins University</i>
10:40–11:25 a.m.	Multiplexed Two-Photon Imaging Across Extended Cortical Circuitry	Spencer Smith, PhD <i>University of North Carolina at Chapel Hill</i>
11:25 a.m.–12:10 p.m.	Fast 3D <i>In Vivo</i> Imaging of Neuronal Activity with Subcellular Resolution in Large Tissue Volumes	Balázs Rózsa, MD, PhD <i>Hungarian Academy of Sciences</i>
12:10–1:10 p.m.	LUNCH: Room 151 AB	
1:10–1:55 p.m.	Truly Simultaneous Imaging of Neural Activity in Three Dimensions	Rafael Yuste, MD, PhD <i>Columbia University</i>
1:55–2:40 p.m.	Local Circuit Analysis with Integrated Large-Scale Recording of Neuronal Activity and Optogenetics	György Buzsáki, MD, PhD <i>New York University School of Medicine</i>
2:40–3:40 p.m.	SUMMARY, DISCUSSION, BREAKOUT GUIDE	
3:40–4:00 p.m.	AFTERNOON BREAK	

AFTERNOON BREAKOUT SESSIONS \* Participants select one discussion group at 4:00 p.m. and one at 5:00 p.m.

TIME	THEME	ROOM
4:00–5:00 p.m.	<b>Group 1</b> Optimizing the Biology: Sensors, Dyes, Surgery Douglas Kim, PhD   Mark Andermann, PhD Kristina Nielsen, PhD   Prakash Kara, PhD	143A
	<b>Group 2</b> Hardware Finesse: Electrodes, Optics, Scanned Versus Scanless Imaging Spencer Smith, PhD   Rafael Yuste, MD, PhD Balázs Rózsa, MD, PhD   György Buzsáki, MD, PhD	143B
5:00–6:00 p.m.	BREAKOUT SESSIONS REPEAT	



# Table of Contents

---

Introduction .....	7
Engineering Fluorescent Calcium Sensor Proteins for Imaging Neural Activity <i>Douglas S. Kim, PhD, Vivek Jayaraman, PhD, Loren L. Looger, PhD, and Karel Svoboda, PhD.</i> .....	9
Simultaneous Two-Photon Calcium Imaging of Entire Cortical Columns <i>Glenn J. Goldey and Mark L. Andermann, PhD.</i> .....	21
Two-Photon Calcium Imaging in the Macaque Monkey <i>Kristina J. Nielsen, PhD</i> .....	33
Mesoscale Two-Photon Microscopy: Engineering a Wide Field of View with Cellular Resolution <i>Jeffrey N. Stirman, PhD, and Spencer L. Smith, PhD</i> .....	41
Acousto-optical Scanning-Based High-Speed 3D Two-Photon Imaging <i>in Vivo</i> <i>Balázs Rózsa, MD, PhD, Gergely Szalay, and Gergely Katona</i> .....	49
Simultaneous Holographic Imaging of Neuronal Circuits in Three Dimensions <i>Sean Quirin, PhD, Jesse Jackson, PhD, Darcy S. Peterka, PhD, and Rafael Yuste, MD, PhD.</i> .....	63
Local Circuit Analysis with Integrated Large-Scale Recording of Neuronal Activity and Optogenetics <i>György Buzsáki, MD, PhD.</i> .....	73



# Introduction

---

Electrophysiological recording from one neuron at a time has been invaluable in developing our current understanding of the neural basis of sensation, perception, and behavior. However, in order to develop a detailed microcircuit-scale framework of brain function, direct monitoring of hundreds to thousands of neurons within and across brain regions is necessary.

Parallel advancements in biology and optoelectronics already allow for measuring the activity of entire neuronal populations at single-cell resolution. For example, genetically encoded sensors (e.g., GCaMP6), delivered virally or transgenically, permit monitoring of spiking and synaptic activity in specific neuronal cell types. Sensors can be tweaked for the optimal sensitivity, speed, and dynamic range needed for specific brain regions or imaging modalities. Optical prisms inserted into the brain allow for simultaneous two-photon functional imaging of all layers of neocortex. In addition, deep-tissue functional imaging without optical prisms is possible using newly developed red-shifted fluorescent proteins (e.g., RCaMP, R-GECO, O-GECO, and CAR-GECO). Importantly, new strategies are also being devised for imaging in the macaque monkey brain with single neuron resolution. Moreover, single-neuron responses can now be imaged simultaneously across multiple brain areas using a new objective lens design and beam multiplexing. Three-dimensional acousto-optical scanning or scanless holographic methods attain orders of magnitude higher-speed imaging compared with conventional galvanometer scanning. Finally, considering new electrode designs and spike-sorting algorithms, state-of-the-art multielectrode recordings remain a gold standard for monitoring neuronal populations in behaving animals.

This short course will provide a comprehensive evaluation of the latest genetically encoded sensors and electrodes, experimental techniques, and optoelectronic innovations that allow investigators to monitor multineuronal activity in the brain during behavior.



# **Engineering Fluorescent Calcium Sensor Proteins for Imaging Neural Activity**

Douglas S. Kim, PhD, Vivek Jayaraman, PhD,  
Loren L. Looger, PhD, and Karel Svoboda, PhD

---

Janelia Research Campus  
Howard Hughes Medical Institute  
Ashburn, Virginia



## Introduction

Understanding neural circuit function requires making measurements of neural activity over many spatial and temporal scales. Calcium indicators have been especially useful for studying neuronal activity over these scales, especially for action potential (AP) detection. APs in most neurons are tightly coupled to large (20-fold) and rapid (rise time <1 ms) increases in intracellular free-calcium concentration. These calcium transients are proxies for the underlying electrical activity. They can be measured *in vitro* and *in vivo* as fluorescence changes of calcium indicators in neuronal somata (Stosiek et al., 2003; Reiff et al., 2005), dendrites (Svoboda et al., 1997; Seelig and Jayaraman, 2013), and axons (Cox et al., 2000; Petreanu et al., 2012). Calcium indicators are also useful in nonspiking, graded potential neurons (Haag and Borst, 2000; Seelig et al., 2010), although optimal indicator parameters may differ. Additionally, excitatory synaptic transmission is typically associated with large-amplitude (20- to 100-fold) increases in calcium concentration in small synaptic compartments (e.g., dendritic spines). These synaptic calcium transients can be used to quantify synaptic transmission *in vitro* (Yuste and Denk, 1995) and *in vivo* (Jia et al., 2010; Chen et al., 2013). Calcium imaging is useful for probing neural activity over physiological and behavioral timescales of milliseconds to months, and wide spatial ranges from micrometers to millimeters.

## Genetically Encoded Calcium Indicators

Small-molecule calcium indicators (e.g., Fura2, Fluo4, OGB1) have excellent properties in terms of kinetics and fractional fluorescence change (Tsien, 1989). However, introducing these molecules into tissue is invasive and nonspecific. Loading the molecules is destructive and incompatible with long-term imaging. Fluorescent protein-based indicators can overcome these problems. Genetically encoded calcium indicators (GECIs) can be expressed in specific types of neurons using minimally invasive methods over chronic timescales (Mank et al., 2008; Tian et al., 2009; Lutcke et al., 2010; Akerboom et al., 2012; Chen et al., 2013). Additionally, protein indicators can be targeted to subcellular locations to report specific dynamic events of interest (Miyawaki et al., 1997; Mao et al., 2008). GECIs occupy a niche that complements single-unit electrophysiology. Although single-unit methods have better sensitivity and time resolution, through optimization, GECIs have been engineered that achieve signal-to-noise ratios (SNRs) that rival electrophysiological methods.

Multiple GECI types have been developed and improved over several development cycles. GCaMP and related sensors are based on circularly permuted green fluorescent protein (cpGFP) (Baird et al., 1999) linked to calmodulin (CaM) and the M13 peptide from myosin light-chain kinase (Nakai et al., 2001; Ohkura et al., 2005; Tallini et al., 2006; Tian et al., 2009; Zhao et al., 2011; Akerboom et al., 2012; Chen et al., 2013; Wu et al., 2013). For most GCaMP sensors, fluorescence intensity increases with elevated calcium. Ratiometric GCaMP variants have also been reported (Zhao et al., 2011). Cameleons consist of a pair of fluorescent proteins linked by CaM/M13 (Miyawaki et al., 1997; Nagai et al., 2004; Palmer et al., 2006). Calcium elevations cause a change in Förster resonance energy transfer. TN-XXL and its derivatives are similar to cameleons, but use the calcium-binding protein troponin to sense calcium (Mank et al., 2008; Thestrup et al., 2014).

## Optimizing GCaMP, a GFP-based calcium indicator

GCaMP-type GECIs are widely used to provide a unique view into nervous system function. They have been used to measure the dynamics of large populations of neurons over times of weeks, even during learning (Tian et al., 2009; Akerboom et al., 2012; Huber et al., 2012; Chen et al., 2013). They can track activity in local and long-range axonal projections and provide information about the activity of neurons that are inaccessible to electrophysiological methods (Suzuki et al., 2003). Moreover, this GFP-based indicator has a large two-photon absorption cross-section at accessible excitation wavelengths for *in vivo* imaging through hundreds of microns of brain tissue.

GCaMP engineering has benefited from structure-based design (Fig. 1). GCaMP relies on a calcium-dependent interaction between CaM and the CaM-interacting M13 peptide, both fused to cpGFP. With cooperative calcium binding, the CaM/M13 interaction changes sensor conformation. This conformational shift modulates the environment of the cpGFP chromophore through formation of new domain interfaces, rearrangement of protein side chains, and reduction of solvent access to the chromophore. These rearrangements cause increased absorption and brightness with increasing calcium concentrations. The GCaMP crystal structure (Wang et al., 2008; Akerboom et al., 2009; Ding et al., 2014) revealed the importance of the CaM/cpGFP proto-interface in regulating chromophore function. Functional screening of GCaMP variants at the CaM/cpGFP interface and in other domains

## NOTES

has produced indicators with improved fluorescence changes (Akerboom et al., 2012; Chen et al., 2013).

### Sensitive GCaMP indicators

Recently, we developed the general-purpose GCaMP6 sensors for *in vivo* imaging of neuronal populations (Chen et al., 2013). We used a neuronal culture assay for GCaMP6 development (Wardill et al., 2013). The assay enabled rapid GECI characterization and optimization in the relevant cell type. Neurons have fast and small-amplitude calcium accumulations that are difficult to model in nonneuronal systems. Primary rat hippocampal cultures in multiwell plates were transduced with GECI variants and a nuclear fluorescent protein construct to control for expression level. APs were triggered using extracellular stimulation electrodes, while neurons were imaged using fluorescence microscopy. We imaged the fluorescence dynamics of multiple individual neurons responding to a variety of trains of APs. This neuronal culture assay allowed us to characterize large numbers of GECI variants under relevant conditions (Fig. 1).

The GCaMP6 variants can reliably detect a single AP stimulus, with responses that equal or exceed the fluorescence response of the synthetic calcium dye OGB1 (Fig. 1). These highly sensitive GCaMP6 indicators differ in their speed. In cultured hippocampal neurons, GCaMP6s is slowest, with a decay time of 1.8 s ( $\tau_{1/2}$  after 10 APs). GCaMP6m has faster kinetics while maintaining a high response. GCaMP6f is the fastest variant, with a 1 AP rise time-to-peak of  $\sim 50$  ms and a decay time ( $\tau_{1/2}$  after 1 AP) of  $\sim 140$  ms. The GCaMP6 indicators have basal fluorescence levels ( $F_0$ ) similar to those of GCaMP5G (Fig. 1c) (Akerboom et al., 2012).

Under favorable imaging conditions, these sensors detect single spikes in neuronal populations *in vivo* (Fig. 2) (Chen et al., 2013). GCaMP6s was expressed virally in the visual cortex of an anesthetized, adult mouse. Visual stimuli in the form of drifting gratings in different orientations of movement were shown to the mouse. The fraction of responding neurons using GCaMP6s exceeded the fraction detected with OGB1, likely because they detected weak responses missed by OGB1. In additional imaging experiments, responses

from a layer 2/3 pyramidal neuron were simultaneously imaged using two-photon microscopy and recorded by patch electrode. The orientation-selective responses to single APs at the soma were reported with high sensitivity by GCaMP6s compared with those of previous indicators. GCaMP6f exhibited large  $\Delta F/F_0$  (fluorescence change normalized by resting fluorescence) responses and a fast single-spike rise time-to-peak of  $\sim 50$  ms. The high sensitivity of GCaMP6s enabled detection of even subthreshold dendritic spine activity in response to drifting gratings. Moreover, repeated imaging of the same neuron and processes over several weeks was conducted using GCaMP6s. The stability of the orientation tuning of dendritic spines was assessed with this high-sensitivity, genetically encoded sensor. GECIs with even higher sensitivity will allow larger populations of neurons to be imaged more rapidly and under more challenging conditions (e.g., imaging in awake and behaving animals).

### Strategies for increasing GECI sensitivity

GECI sensitivity could be increased in several ways for different applications.

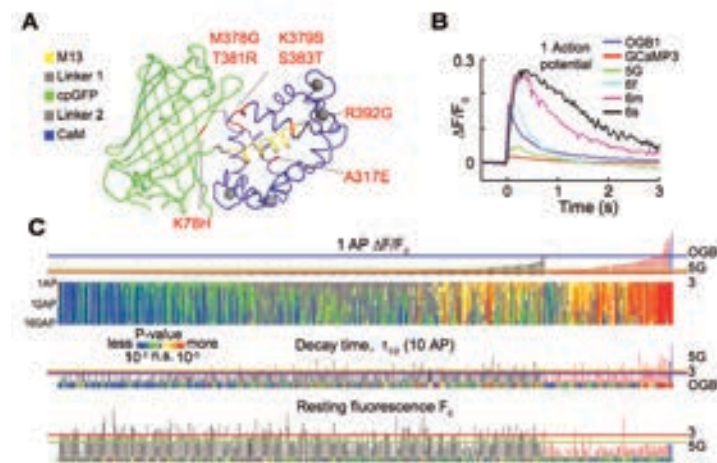


**Figure 1.** GCaMP6 engineering. **A**, GCaMP structure (Akerboom et al., 2009) and mutations in different GCaMP6 variants. M13 peptide (yellow), linker 1 (gray), cpGFP (green), linker 2 (gray), CaM (blue), and mutated positions found in GCaMP6 variants relative to GCaMP5G (red text). **B**, Responses averaged across multiple neurons and wells for GCaMP3, 5G, 6f, 6m, 6s, and OGB1-AM. Fluorescence changes in response to 1 AP. **C**, Screening results, 447 GCaMPs. Top, fluorescence change in response to 1 AP (vertical bars,  $\Delta F/F_0$ ; green bar, OGB1-AM, left; black bars, single GCaMP mutations; red bars, combinatorial mutations; blue, GCaMP6 indicators) and significance values for 1, 2, 3, 5, 10, 20, 40, 80, and 160 AP stimuli compared with GCaMP3 (color plot). Middle, half decay time after 10 APs. Bottom, resting fluorescence,  $F_0$  normalized to nuclear mCherry fluorescence. Red line, GCaMP3 level; green line, GCaMP5G level; blue line, OGB1-AM level. Figure adapted with permission from Chen et al. (2013), their Fig. 1a–c.

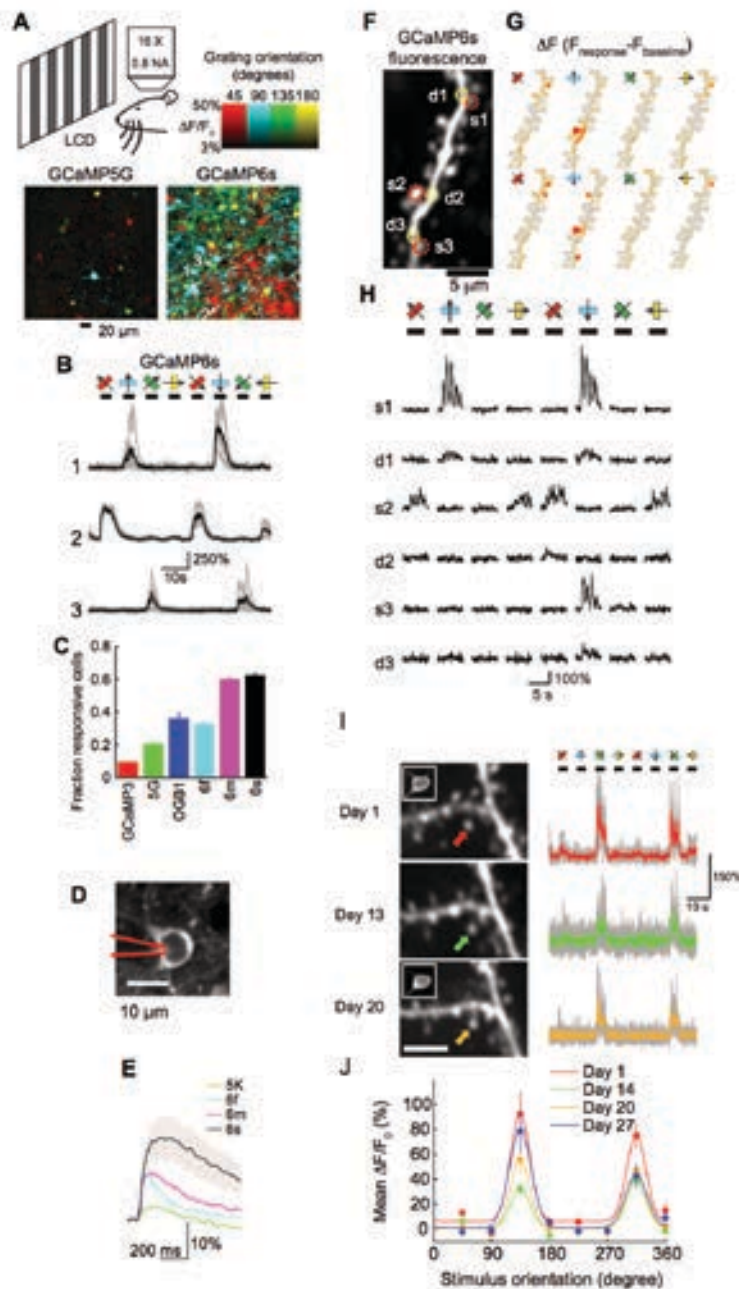


**Figure 2.** Imaging activity in neurons and dendritic spines in the mouse visual cortex. **A**, Top, schematic of the experiment. Bottom, field-of-view (FOV) showing neurons color-coded according to their preferred orientation (hue) and response amplitude (brightness) for GCaMP5G (left) and GCaMP6s (right). Scale bar, 20  $\mu\text{m}$ . **B**, Example  $\Delta F/F_0$  traces from 3 neurons expressing GCaMP6s. Single sweeps (gray) and averages of 5 sweeps (black) are overlaid. Directions of grating motion (8 directions) are shown above traces (arrows). **C**, The fraction of cells scored as responding to visual stimulation when loaded with different calcium indicators. Error bars correspond to SEM ( $n = 70, 39, 23, 38, 21, 34$  FOVs) for GCaMP3, 5G, OGB1-AM, 6f, 6m, and 6s, respectively. **D**, Simultaneous fluorescence dynamics and spikes in a GCaMP6s-expressing neuron. GCaMP6s-expressing neuron with the recording pipette indicated schematically. Scale bar, 10  $\mu\text{m}$ . **E**, Median fluorescence change in response to 1 AP for different calcium indicators. Shading corresponds to SEM,  $n = 9$  (GCaMP5K; data from Akerboom et al., 2012), 11 (GCaMP6f), 10 (GCaMP6m), and 9 (GCaMP6s) cells. **F**, Image of a layer 2/3 dendritic branch expressing GCaMP6s. Regions of interest (ROIs) are indicated as dashed circles (red, spines; yellow, dendrites). **G**, Map of fluorescence change ( $\Delta F = F_{\text{response}} - F_{\text{baseline}}$ ) in response to drifting gratings of 8 different orientations. **H**, Responses of dendritic spines (s1–s3) and neighboring dendritic shafts (d1–d3) to drifting gratings with different orientations (corresponding to ROIs indicated in F). **I**, Left, the same GCaMP6s-labeled spine imaged over weeks. Right, fluorescence responses to oriented drifting gratings. Insets, parent soma of imaged spines. **J**, Orientation selectivity of single spines measured over time (same as I). Figure adapted with permission from Chen et al. (2013), their Figs. 2–4.

## NOTES

The high sensitivity of GCaMP6s and 6f was achieved by both increasing the dynamic range (ratio of calcium-saturated fluorescence to calcium-free fluorescence;  $F_{sat}/F_{apo}$ ) and increasing calcium affinity of the sensor compared with previous GCaMP variants. The high affinity leads to saturation of these sensors at modest activity levels, making them unsuitable for monitoring activity patterns in neurons with high spike rates (>100 Hz). The saturation of GCaMP6 variants was evident in the high-frequency motor neurons of *Drosophila* larvae (Fig. 3). For example, GCaMP6m accurately tracked individual spikes in motor neuron boutons at the larval neuromuscular junction when stimulated at low frequencies (1–5 Hz), but the fluorescence responses reached a plateau at higher frequencies (40–160 Hz). Engineering GECIs with lower affinity will aid in tracking high-frequency activity and graded potential neuronal activity. In addition, GCaMP is CaM-based and contains four calcium-binding domains that cooperate in binding calcium. Reducing the binding cooperativity could increase the linear range for detecting calcium changes.

Intracellular calcium is highly buffered by endogenous proteins in some neurons and can make imaging with calcium sensors challenging. Parvalbumin-positive interneurons exhibit relatively low fluorescence responses when loaded with OGB1 compared with excitatory neurons (Kerlin et al., 2010). In contrast to the above approach, engineering GECIs with very high affinity could be particularly useful for increasing sensitivity in these neuronal subtypes. Ultrasensitive YC-nano indicators with very high calcium affinity ( $K_d \sim 15$  nM) have been reported (Horikawa et al., 2010).

Additional strategies for increasing GECI sensitivity can be explored. The SNR of GECIs can also be improved by minimizing the resting fluorescence without reducing the peak fluorescence. Lowering the background fluorescence from inactive neurons and processes while maintaining peak fluorescence will serve to increase SNR, especially

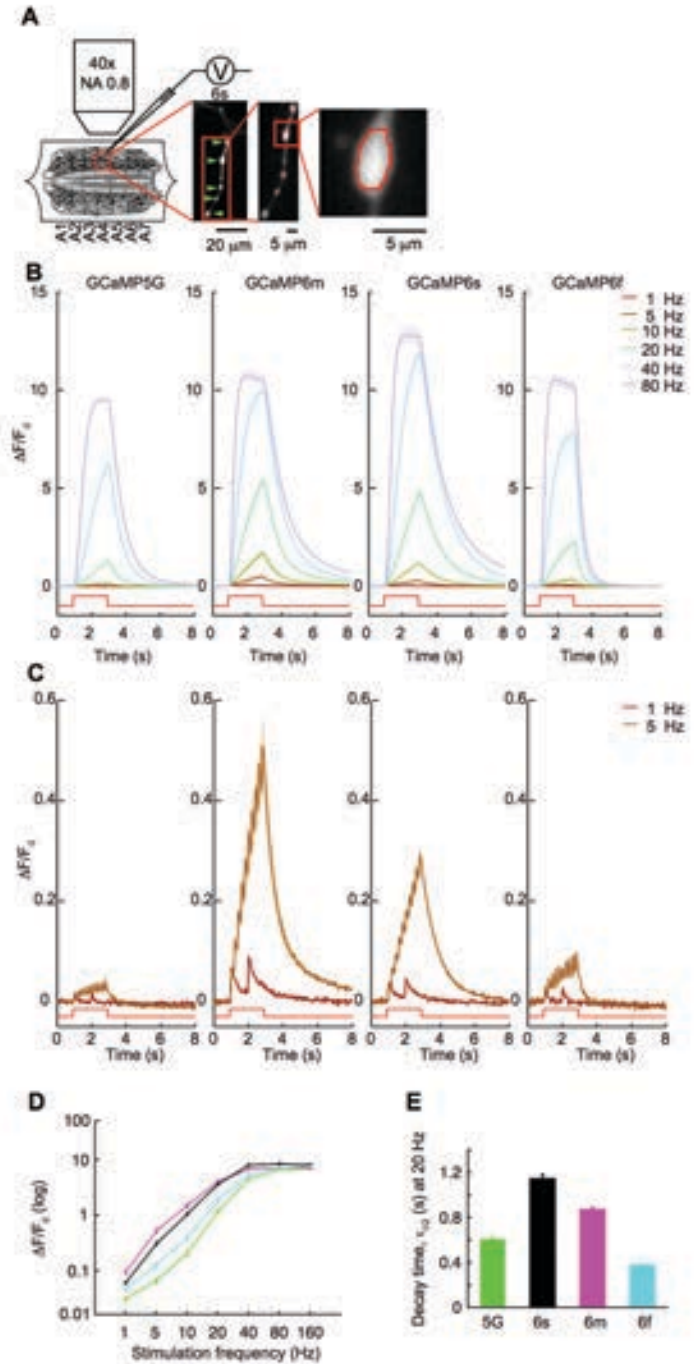


**Figure 3.** Fluorescence activity imaging in *Drosophila* larval neuromuscular junction boutons. **A**, Schematic of larval NMJ stimulation and imaging, epifluorescence (green arrow heads), and high magnification  $\Delta F/F_0$  images of Type 1b boutons from muscle 13 (segments A3–A5). **B**, Average  $\Delta F/F_0$  ( $\pm$  SEM) traces recorded after 1, 5, 10, 20, 40, and 80 Hz (green, cyan, magenta, black;  $n = 10, 12, 14, 12$  FOVs, respectively) stimulus for 2 s (red) for GCaMP5G, 6m, 6s, and 6f. **C**, Average  $\Delta F/F_0$  traces recorded after 1 and 5 Hz stimulus for 2 s. **D**, Average peak  $\Delta F/F_0$  from 1 to 160 Hz. **E**, Average half decay time after 20 Hz stimulation for 2 s. Figure adapted with permission from Chen et al. (2013), their Supplementary Fig. 3.

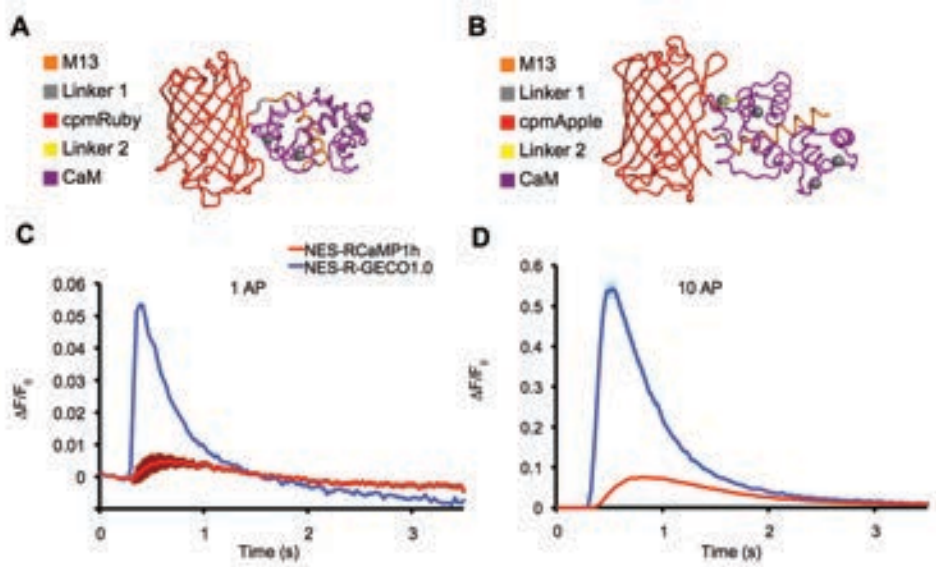


**Figure 4.** Red GECIs and their performance in cultured neurons. **A**, RCaMP1 structure including cpmRuby fluorescent protein (red), M13 peptide (orange), linker 1 (gray), CaM (purple), and linker 2 (yellow) (Akerboom et al., 2012). **B**, R-GECO1.0 structure including cpmApple fluorescent protein (red) (Akerboom et al., 2012). **C**, Averaged fluorescence response of neuronal cell bodies in culture to 1 AP stimulus. Nuclear export signal (NES)-tagged RCaMP1h (red), NES-R-GECO1.0 (blue). **D**, 10 AP stimulus.

with epifluorescence imaging of large populations of neurons. In the past, GCaMP variants with appreciable resting fluorescence were produced to enable structural imaging and identification of GECI-expressing neurons. However, transgenic animals now allow imaging in a background in which neurons, nuclei, or other structures of interest are labeled with a red fluorescent protein (RFP), obviating the need for substantial GCaMP resting fluorescence. Reducing resting fluorescence even by a factor of two while maintaining high peak fluorescence levels will have a substantial impact on SNR, increasing the yield in cellular imaging experiments by several-fold. In this manner, the scale of monitored neurons could be increased.

### Fast GCaMP sensors

Existing GECIs are relatively slow compared with the speed of APs in part because of sensor protein dynamics. Calcium binds and unbinds cooperatively to the CaM EF-hand domains 100- to 1000-fold faster than the onset and offset of GCaMP fluorescence (Faas et al., 2011). GCaMP response kinetics have been improved, particularly with GCaMP6f, which has relatively fast rise ( $\sim 50$  ms, 1 AP  $\tau_{peak}$ ) and decay ( $\sim 140$  ms, 1 AP  $\tau_{1/2}$ ) times while maintaining OGB1-like SNR (Chen et al., 2013). GCaMP6f incorporates a mutation that is predicted to disrupt the M13/CaM interaction (A317E, Fig. 1). The M13/CaM interaction is likely a slow step downstream of calcium binding that affects the rate of fluorescence onset (Sun et al., 2013). The M13/CaM interaction affects calcium binding and unbinding, and thus,

changing this interaction can also affect fluorescence offset rate.

GCaMP6f reports AP timing in neurons better than other GECIs. For example, GCaMP6f accurately tracked spiking at moderate frequencies (20 Hz) better than GCaMP6s at the *Drosophila* neuromuscular junction (NMJ) (Fig. 3). The decay time was inversely related to calcium  $K_d$ . GCaMP6f ( $K_d \sim 375$  nM) is also faster than GCaMP6s ( $K_d \sim 144$  nM). Faster variants can be engineered without altering affinity (Sun et al., 2013). In the future, fast GECIs with appropriate affinity, high SNR, and broad dynamic range will be most useful.

### Optimizing red GECIs, RCaMP, and R-GECO

GECIs based on red-shifted fluorescent proteins have been made, including RCaMP, R-GECO, O-GECO, and CAR-GECO (Fig. 4) (Zhao et al., 2011; Akerboom et al., 2013; Wu et al., 2013). Red indicators are of particular interest for several reasons. First, longer wavelength excitation light penetrates deeper into tissue. In addition, red fluorescence is absorbed much less than green fluorescence, especially in mammalian tissue, giving red fluorophores a competitive advantage for *in vivo* imaging. Red GECIs therefore enable deeper and less invasive imaging than green GECIs. Second, combinations of red and green GECIs promise simultaneous imaging of multiple distinct neural structures (Li et al., 2013). Third, red GECIs are more easily combined with channelrhodopsin-2 (ChR2)-based manipulations

## NOTES

of neural circuits because their excitation spectra are separated. Finally, many transgenic animals with green fluorescence have been created; red GECIs can be used in these animals. Optimized red GECIs will thus be useful individually or in combination with green GECIs.

Multicolor neuronal imaging ideally employs sensors with matched performance in each channel. The first-generation red GECIs, RCaMP1h and R-GECO1.0, underperformed green GECIs, such as GCaMP6s and GCaMP6f, in several ways (Figs. 1, 4). Both had inferior maximal dynamic range in solution measurements and responses after 160 AP stimulation at 83 Hz (Table 1). The red GECIs also had lower apparent calcium affinity compared with the green GECIs. The 1 AP fluorescence response was worse than that of GCaMP sensors. The red sensors were also slower than GCaMP6f. In general, RCaMP1h and R-GECO1.0 were less sensitive than GCaMP6s.

Newer red GECIs are improved and have begun to approach GCaMP6 sensitivity levels (Ohkura et al., 2012; Wu et al., 2013). R-GECO1.2 has improved dynamic range ( $F_{\text{calcium-saturated}}/F_{\text{calcium-free}} = 33$ ) compared with R-GECO1.0 but has lower affinity ( $K_d \sim 1200$  nM) than GCaMP6 variants (Wu et al., 2013). The orange GECI, O-GECO1 (based on mOrange) has excellent dynamic range ( $F_{\text{calcium-saturated}}/F_{\text{calcium-free}} = 14$ ) but lower affinity ( $K_d \sim 1500$  nM). Further optimization of these and other red GECIs will enable multicolor imaging with GCaMP6. Improved red GECIs will also enhance single red-channel imaging.

Red GECIs have been more challenging to engineer because of photophysical limitations of RFPs related to brightness and bleaching. Ideally, the brightness of the calcium-bound state would be maximized.

Dim GECIs have lower SNR and require more laser power. Among red GECIs, RCaMP is the brightest molecule (extinction coefficient\*quantum yield =  $33 \text{ mM}^{-1} \text{ cm}^{-1}$ ) relative to GCaMP6s ( $42 \text{ mM}^{-1} \text{ cm}^{-1}$ ) (Table 2). The calcium-saturated brightnesses of R-GECO1.0, R-GECO1.2, O-GECO1, and CAR-GECO1 are all less than half that of RCaMP1h.

Under two-photon excitation, RFPs and red GECIs tend to bleach rapidly and/or show reversible dark states. The peak brightness per molecule (an experimental quantity proportional to quantum efficiency and inversely related to bleaching rate) (Mutze et al., 2012) is substantially smaller for R-GECO1.0 and RCaMP1h compared with GCaMP ( $\sim 33\%$  and  $\sim 50\%$ , respectively) (Akerboom et al., 2013). In addition, R-GECO1.0 is transiently induced to become red fluorescent after exposure to blue light, which makes it incompatible with the action spectrum of ChR2 (Akerboom et al., 2013; Wu et al., 2013). Engineering to increase chromophore brightness, stability, and spectral purity could improve red GECIs substantially.

## Conclusion

For more than 15 years, fluorescent proteins have been engineered to report neural activity. Although GECIs are now routinely used to image neuronal activity *in vivo*, they still have limitations. Quantitative testing of GECIs in neurons has accelerated calcium-sensor optimization in terms of sensitivity, speed, and dynamic range. GECI photostability and expression systems for *in vivo* imaging await further improvement. Better indicators will enable the dissection of neural circuits through the correlation of specific neuronal activity with behavior at higher resolution and over wider populations of neurons. Activity indicators for other neuronal state variables

Table 1. GECI sensitivity and kinetic parameters (Akerboom et al., 2012; Chen et al., 2013)

GECI	$F_{\text{calcium-saturated}}/F_{\text{calcium-free}}$	$\Delta F/F_0$ (160 AP)	$K_d$ (nM)	$\Delta F/F_0$ (1 AP)	Decay $\tau_{1/2}$ (10 AP) (s)
RCaMP1h	11	3	1300	0.02	1.8
R-GECO1.0	16	8	449	0.08	0.8
GCaMP6s	63	17	144	0.23	1.8
GCaMP6f	52	13	375	0.19	0.4

Table 2. GECI brightness measured in solution (Akerboom et al., 2012; Chen et al., 2013)

GECI	Brightness (extinction coefficient*quantum yield, $\text{mM}^{-1} \text{ cm}^{-1}$ )
GCaMP6s	42
RCaMP1h	33
R-GECO1.0	11
R-GECO1.2	15
O-GECO1	14
CAR-GECO1	8

(e.g., membrane voltage) and light-gated effectors that alter activity will also be critical for *in vivo*, light-based neurophysiology.

## Acknowledgments

The Genetically-Encoded Neuronal Indicator and Effector (GENIE) Project at the Janelia Research Campus is funded by the Howard Hughes Medical Institute. Primary data included here were produced by past and present members and collaborators with the project, including Tsai-Wen Chen, Trevor J. Wardill, Yi Sun, Hod Dana, Jasper Akerboom, Stefan R. Pulver, Ronak Patel, John J. Macklin, Eric R. Schreiter, Benjamin F. Fosse, and Douglas S. Kim. Technical expertise was provided by Jeremy P. Hasseman, Getahun Tsegaye, Reza Behnam, Brenda C. Shields, Zijuan Ma, Amy Hu, Melissa Ramirez, and Kimberly Ritola. We thank other collaborators including Sabine L. Renninger, Michael B. Orger, Amy Baohan, Lin Tian, and Bruce E. Kimmel. The project was supervised by Douglas S. Kim, Rex A. Kerr, Vivek Jayaraman, Loren L. Looger, and Karel Svoboda. We thank our many colleagues at Janelia and elsewhere who have contributed to this work through helpful discussions and sharing reagents. Parts of this chapter were adapted from Akerboom et al., 2013; Chen et al., 2013; and Wardill et al., 2013.

## References

- Akerboom J, Rivera JD, Guilbe MM, Malave EC, Hernandez HH, Tian L, Hires SA, Marvin JS, Looger LL, Schreiter ER (2009) Crystal structures of the GCaMP calcium sensor reveal the mechanism of fluorescence signal change and aid rational design. *J Biol Chem* 284:6455–6464.
- Akerboom J, Chen TW, Wardill TJ, Tian L, Marvin JS, Mutlu S, Calderón NC, Esposti F, Borghuis BG, Sun XR, Gordus A, Orger MB, Portugues R, Engert F, Macklin JJ, Filosa A, Aggarwal A, Kerr RA, Takagi R, Kracun S, et al. (2012) Optimization of a GCaMP Calcium Indicator for Neural Activity Imaging. *J Neurosci* 32:13819–13840.
- Akerboom J, Carreras Calderón N, Tian L, Wabnig S, Prigge M, Tolö J, Gordus A, Orger MB, Severi KE, Macklin JJ, Patel R, Pulver SR, Wardill TJ, Fischer E, Schüler C, Chen TW, Sarkisyan KS, Marvin JS, Bargmann CI, Kim DS, et al. (2013) Genetically encoded calcium indicators for multi-color neural activity imaging and combination with optogenetics. *Front Mol Neurosci* 6:2.
- Baird GS, Zacharias DA, Tsien RY (1999) Circular permutation and receptor insertion within green fluorescent proteins. *Proc Natl Acad Sci USA* 96:11241–11246.
- Chen TW, Wardill TJ, Sun Y, Pulver SR, Renninger SL, Baohan A, Schreiter ER, Kerr RA, Orger MB, Jayaraman V, Looger LL, Svoboda K, Kim DS (2013) Ultrasensitive fluorescent proteins for imaging neuronal activity. *Nature* 499:295–300.
- Cox CL, Denk W, Tank DW, Svoboda K (2000) Action potentials reliably invade axonal arbors of rat neocortical neurons. *Proc Natl Acad Sci USA* 97:9724–9728.
- Ding J, Luo AF, Hu L, Wang D, Shao F (2014) Structural basis of the ultrasensitive calcium indicator GCaMP6. *Science China Life Sci* 57:269–274.
- Faas GC, Raghavachari S, Lisman JE, Mody I (2011) Calmodulin as a direct detector of Ca<sup>2+</sup> signals. *Nat Neurosci* 14:301–304.
- Haag J, Borst A (2000) Spatial distribution and characteristics of voltage-gated calcium signals within visual interneurons. *J Neurophysiol* 83:1039–1051.
- Horikawa K, Yamada Y, Matsuda T, Kobayashi K, Hashimoto M, Matsu-ura T, Miyawaki A, Michikawa T, Mikoshiba K, Nagai T (2010) Spontaneous network activity visualized by ultrasensitive Ca(2+) indicators, yellow Cameleon-Nano. *Nat Methods* 7:729–732.
- Huber D, Gutnisky DA, Peron S, O'Connor DH, Wiegert JS, Tian L, Oertner TG, Looger LL, Svoboda K (2012) Multiple dynamic representations in the motor cortex during sensorimotor learning. *Nature* 484:473–478.
- Jia H, Rochefort NL, Chen X, Konnerth A (2010) Dendritic organization of sensory input to cortical neurons *in vivo*. *Nature* 464:1307–1312.
- Kerlin AM, Andermann ML, Berezovskii VK, Reid RC (2010) Broadly tuned response properties of diverse inhibitory neuron subtypes in mouse visual cortex. *Neuron* 67:858–871.
- Li H, Li Y, Lei Z, Wang K, Guo A (2013) Transformation of odor selectivity from projection neurons to single mushroom body neurons mapped with dual-color calcium imaging. *Proc Natl Acad Sci USA* 110:12084–12089.

## NOTES

- Lutcke H, Murayama M, Hahn T, Margolis DJ, Astori S, Zum Alten Borgloh SM, Gobel W, Yang Y, Tang W, Kugler S, Sprengel R, Nagai T, Miyawaki A, Larkum ME, Helmchen F, Hasan MT (2010) Optical recording of neuronal activity with a genetically-encoded calcium indicator in anesthetized and freely moving mice. *Front Neural Circ* 4:9.
- Mank M, Santos AF, Drenth S, Mrcic-Flogel TD, Hofer SB, Stein V, Hendel T, Reiff DF, Levelt C, Borst A, Bonhoeffer T, Hubener M, Griesbeck O (2008) A genetically encoded calcium indicator for chronic *in vivo* two-photon imaging. *Nat Methods* 5:805–811.
- Mao T, O'Connor DH, Scheuss V, Nakai J, Svoboda K (2008) Characterization and subcellular targeting of GCaMP-type genetically-encoded calcium indicators. *PLoS One* 3:e1796.
- Miyawaki A, Llopis J, Heim R, McCaffery JM, Adams JA, Ikura M, Tsien RY (1997) Fluorescent indicators for  $Ca^{2+}$  based on green fluorescent proteins and calmodulin. *Nature* 388:882–887.
- Mutze J, Iyer V, Macklin JJ, Colonell J, Karsh B, Petrusek Z, Schwille P, Looger LL, Lavis LD, Harris TD (2012) Excitation spectra and brightness optimization of two-photon excited probes. *Biophys J* 102:934–944.
- Nagai T, Yamada S, Tominaga T, Ichikawa M, Miyawaki A (2004) Expanded dynamic range of fluorescent indicators for  $Ca^{2+}$  by circularly permuted yellow fluorescent proteins. *Proc Natl Acad Sci USA* 101:10554–10559.
- Nakai J, Ohkura M, Imoto K (2001) A high signal-to-noise  $Ca^{2+}$  probe composed of a single green fluorescent protein. *Nat Biotechnol* 19:137–141.
- Ohkura M, Matsuzaki M, Kasai H, Imoto K, Nakai J (2005) Genetically encoded bright  $Ca^{2+}$  probe applicable for dynamic  $Ca^{2+}$  imaging of dendritic spines. *Anal Chem* 77:5861–5869.
- Ohkura M, Sasaki T, Sadakari J, Gengyo-Ando K, Kagawa-Nagamura Y, Kobayashi C, Ikegaya Y, Nakai J (2012) Genetically encoded green fluorescent  $Ca^{2+}$  indicators with improved detectability for neuronal  $Ca^{2+}$  signals. *PLoS one* 7:e51286.
- Palmer AE, Giacomello M, Kortemme T, Hires SA, Lev-Ram V, Baker D, Tsien RY (2006)  $Ca^{2+}$  indicators based on computationally redesigned calmodulin-peptide pairs. *Chem Biol* 13:521–530.
- Petreaanu L, Gutnisky DA, Huber D, Xu NL, O'Connor DH, Tian L, Looger L, Svoboda K (2012) Activity in motor-sensory projections reveals distributed coding in somatosensation. *Nature* 489:299–303.
- Reiff DF, Ihring A, Guerrero G, Isacoff EY, Joesch M, Nakai J, Borst A (2005) *In vivo* performance of genetically encoded indicators of neural activity in flies. *J Neurosci* 25:4766–4778.
- Seelig JD, Jayaraman V (2013) Feature detection and orientation tuning in the *Drosophila* central complex. *Nature* 503:262–266.
- Seelig JD, Chiappe ME, Lott GK, Dutta A, Osborne JE, Reiser MB, Jayaraman V (2010) Two-photon calcium imaging from head-fixed *Drosophila* during optomotor walking behavior. *Nat Methods* 7:535–540.
- Stosiek C, Garaschuk O, Holthoff K, Konnerth A (2003) *In vivo* two-photon calcium imaging of neuronal networks. *Proc Natl Acad Sci USA* 100:7319–7324.
- Sun XR, Badura A, Pacheco DA, Lynch LA, Schneider ER, Taylor MP, Hogue IB, Enquist LW, Murthy M, Wang SSH (2013) Fast GCaMPs for improved tracking of neuronal activity. *Nat Commun* 4:2170.
- Suzuki H, Kerr R, Bianchi L, Frokjaer-Jensen C, Slone D, Xue J, Gerstbrein B, Driscoll M, Schafer WR (2003) *In vivo* imaging of *C. elegans* mechanosensory neurons demonstrates a specific role for the MEC-4 channel in the process of gentle touch sensation. *Neuron* 39:1005–1017.
- Svoboda K, Denk W, Kleinfeld D, Tank DW (1997) *In vivo* dendritic calcium dynamics in neocortical pyramidal neurons. *Nature* 385:161–165.
- Tallini YN, Ohkura M, Choi BR, Ji G, Imoto K, Doran R, Lee J, Plan P, Wilson J, Xin HB, Sanbe A, Gulick J, Mathai J, Robbins J, Salama G, Nakai J, Kotlikoff MI (2006) Imaging cellular signals in the heart *in vivo*: Cardiac expression of the high-signal  $Ca^{2+}$  indicator GCaMP2. *Proc Natl Acad Sci USA* 103:4753–4758.
- Thestrup T, Litzlbauer J, Bartholomaeus I, Mues M, Russo L, Dana H, Kovalchuk Y, Liang Y, Kalamakis G, Laukat Y, Becker S, Witte G, Geiger A, Allen T, Rome LC, Chen TW, Kim DS, Garaschuk O, Griesinger C, Griesbeck O (2014) Optimized ratiometric calcium sensors for functional *in vivo* imaging of neurons and T lymphocytes. *Nat Methods* 11:175–182.

- Tian L, Hires SA, Mao T, Huber D, Chiappe ME, Chalasani SH, Petreanu L, Akerboom J, McKinney SA, Schreiter ER, Bargmann CI, Jayaraman V, Svoboda K, Looger LL (2009) Imaging neural activity in worms, flies and mice with improved GCaMP calcium indicators. *Nat Methods* 6:875–881.
- Tsien RY (1989) Fluorescent probes of cell signaling. *Annu Rev Neurosci* 12:227–253.
- Wang Q, Shui B, Kotlikoff MI, Sonderrmann H (2008) Structural basis for calcium sensing by GCaMP2. *Structure* 16:1817–1827.
- Wardill TJ, Chen TW, Schreiter ER, Hasseman JP, Tsegaye G, Fosque BF, Behnam R, Shields BC, Ramirez M, Kimmel BE, Kerr RA, Jayaraman V, Looger LL, Svoboda K, Kim DS (2013) A neuron-based screening platform for optimizing genetically-encoded calcium indicators. *PloS one* 8:e77728.
- Wu J, Liu L, Matsuda T, Zhao Y, Rebane A, Drobizhev M, Chang YF, Araki S, Arai Y, March K, Hughes TE, Sagou K, Miyata T, Nagai T, Li WH, Campbell RE (2013) Improved orange and red Ca<sup>2+</sup>/– indicators and photophysical considerations for optogenetic applications. *ACS Chem Neurosci* 4:963–972.
- Yuste R, Denk W (1995) Dendritic spines as basic functional units of neuronal integration. *Nature* 375:682–684.
- Zhao Y, Araki S, Wu J, Teramoto T, Chang YF, Nakano M, Abdelfattah AS, Fujiwara M, Ishihara T, Nagai T, Campbell RE (2011) An expanded palette of genetically encoded Ca<sup>2+</sup> indicators. *Science* 333:1888–1891.



# **Simultaneous Two-Photon Calcium Imaging of Entire Cortical Columns**

Glenn J. Goldey and Mark L. Andermann, PhD

---

Division of Endocrinology, Department of Medicine  
Beth Israel Deaconess Medical Center  
Harvard Medical School  
Boston, Massachusetts



## Introduction

Two parallel approaches have dominated the physiological study of cortical columns. The first approach involves electrophysiological recordings in living coronal brain slices (typically ~400  $\mu\text{m}$  thick). Even though many long-range axonal inputs to cortical columns within each slice are severed, this reductionist approach has provided a wealth of insight into layer-specific physiological properties of neurons and interlaminar flow of neural impulses. This approach makes use of multiple intracellular and extracellular recordings (Sanchez-Vives and McCormick, 2000; Adesnik and Scanziani, 2010; Thomson, 2010), two-photon calcium imaging (MacLean et al., 2006), and voltage-sensitive dye imaging (Petersen and Sakmann, 2001).

The second approach involves making neuronal recordings from the intact brain, where it is possible to correlate neural activity with sensory perception and behavior. As in recordings in brain slices, simultaneous neuronal recordings across cortical layers have been achievable *in vivo*, typically via extracellular recordings that use laminar electrode arrays (Niell and Stryker, 2008; Sakata and Harris, 2009; Adesnik and Scanziani, 2010; Berenyi et al., 2014). However, these methods are typically limited in their ability to achieve a combination of fine spatial resolution, extended recording durations, and elaborate identification of cell types.

As an alternative, two-photon calcium imaging has provided a complementary assay for monitoring activity in awake animals (albeit at lower time resolution) in large numbers of identified neurons across days and weeks (Trachtenberg et al., 2002; Dombeck et al., 2007; Mank et al., 2008; Andermann et al., 2010). However, for all its strengths, this method suffers from two important limitations: (1) high-speed imaging is often confined to a single focal plane parallel to the cortical surface, and (2) light scattering makes it difficult to image deep cortical layers, such as layer 6, which plays a major role both in regulating response amplitudes in superficial layers (Olsen et al., 2012) and in distributing information to a variety of cortical and subcortical targets (Thomson, 2010).

In this chapter, we review the pros and cons of recent methods for deep-layer two-photon imaging. We then describe our recent efforts, in collaboration with the laboratory of Dr. Michael Levene, to employ chronic two-photon calcium imaging through a microprism. This novel strategy combines the optical access of *ex vivo* brain slice preparations with *in vivo* behavioral context and long-range connectivity that is relatively intact.

## Previous Methods for Deep-Layer Two-Photon Imaging in Cortex

Optical scattering degrades image quality at increasing imaging depths within brain tissue. Regenerative amplifiers (Theer et al., 2003; Mittmann et al., 2011) and long-wavelength (1300–1700 nm) Ti:Sapphire lasers (Horton et al., 2013) have both been used to extend the imaging depth of multiphoton microscopy, but practical limitations have restricted their use. Blunt-ended gradient index (GRIN) lenses have been used as implantable micro-optical probes for deep imaging (Jung et al., 2004; Levene et al., 2004; Barretto et al., 2011) but suffer from limited fields of view and significant optical aberrations. Because of the damage incurred above the imaging plane, such probes are more effective when positioned directly above intact structures, such as hippocampus (Barretto et al., 2011), than when placed directly above deep layers of cortex. Traditional multiphoton imaging in certain thinner cortical areas in mice (e.g., mouse primary visual cortex [V1]) (Glickfeld et al., 2013) can reach layers 4 and 5, but this solution often requires high average laser power and/or sparse labeling of neurons. Half-millimeter prisms have been used with one-photon excitation to measure the net fluorescence emission from layer 5 apical dendrites in superficial cortical layers in rats (Murayama et al., 2007), but these fluorescence images lack cellular or subcellular resolution. Current methods allow two-photon imaging of small volumes typically spanning 50–250  $\mu\text{m}$  in depth within a cortical layer, using piezoelectric scanners (Gobel et al., 2007; Kerlin et al., 2010), tunable lenses (Grewe et al., 2011), or multibeam systems (Amir et al., 2007; Cheng et al., 2011). Faster *in vivo* volume imaging methods using single-photon excitation are also emerging, but are currently limited to weakly scattering or sparsely labeled brain tissue (Quirin et al., 2014).

## Microprism Imaging: A Synthesis of *in Vivo* and *ex Vivo* Approaches

To rapidly obtain two-photon imaging data from a larger range of depths, Levene and colleagues have previously shown that inserting a sharp 1 mm glass microprism into the neocortex of an anesthetized mouse can be used for acute, single-session two-photon imaging of anatomical structures across all six cortical layers, including the soma and dendrites of cortical layer 5 pyramidal cells, in a single field of view (Chia and Levene, 2009a, b, 2010). The hypotenuse of the microprism is coated with aluminum and thus serves as a right-angled mirror or “micro-periscope,” with a vertical field of view parallel to the prism face (Fig. 1A). The use of a reflective glass microprism minimizes the distance that excitation photons must travel through scattering tissue to reach deep cortical

## NOTES

tissue, allowing high spatial resolution across layers while requiring only moderate laser power.

Dr. Levene's lab and our lab each developed versions of this approach that are suitable for chronic, large-scale and simultaneous two-photon imaging *in vivo* (Andermann et al., 2013). Here, we focus on our lab's efforts using microprisms to achieve chronic two-photon calcium imaging across all layers of visual cortex in awake mice. Acutely implanted microprisms have been used for wide-field epifluorescence imaging of bulk calcium activity of the apical dendrites of layer 5 neurons (Murayama et al., 2007), following acute insertion into superficial cortical layers. However, the use of epifluorescence imaging precluded visualization of individual neurons. While our current microprism approach provides a means for chronic monitoring of activity in individual neurons and processes using two-photon calcium imaging, it is also compatible with chronic epifluorescence imaging simultaneously across a large,  $1 \times 1$  mm field of view, providing a useful means for rapid mapping of bulk calcium or autofluorescence signals across all cortical layers.

### Overview of microprism implant procedure for chronic two-photon calcium imaging

The procedure we use for implanting a chronic microprism into cortex for the purpose of awake functional imaging has been described elsewhere in great detail (Andermann et al., 2013; Goldey et al., 2014) and is summarized below (Fig. 1B). A critical first surgery involves the implant of a two-armed headpost and a large (3–5 mm diameter) cranial window and imaging well (Fig. 1C), which we have used in previous studies for stable imaging of posterior cortex of anesthetized (Kerlin et al., 2010; Bock et al., 2011; Bonin et al., 2011) or awake (Andermann et al., 2010, 2011, 2013; Glickfeld et al., 2013) mice with high-NA objectives across weeks or months. Following recovery from surgery, mice are trained to tolerate several hours of head restraint (Andermann et al., 2011). Cortical areas are then delineated using wide-field intrinsic autofluorescence imaging in awake mice (Andermann et al., 2011; Glickfeld et al., 2013).

During a subsequent surgery, the window is removed and replaced following viral injection of a genetically encoded calcium indicator (GECI, e.g.,

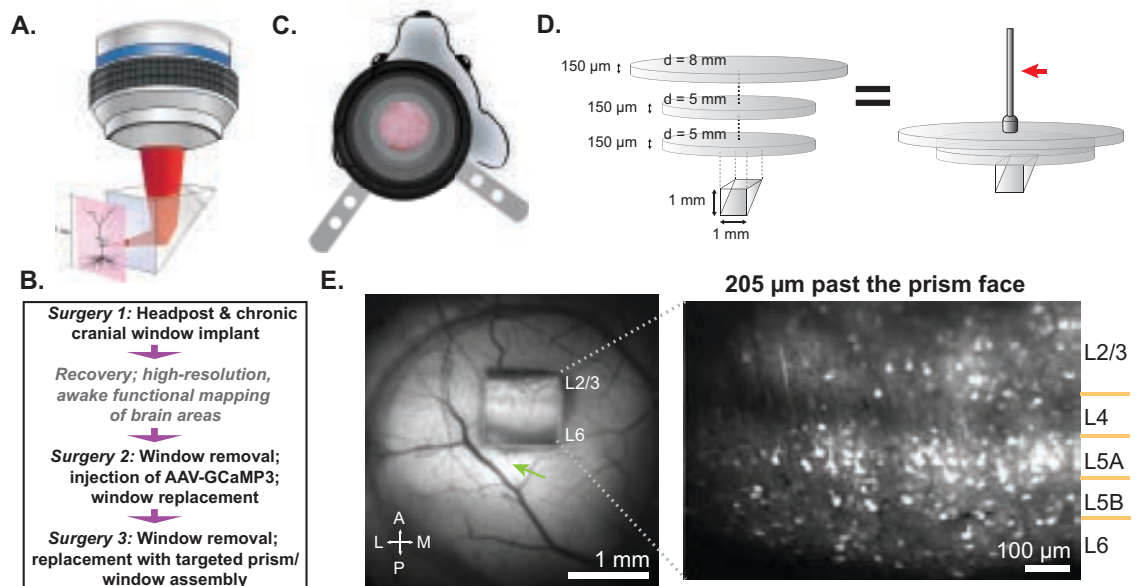


**Figure 1.** Chronic functional imaging across cortical layers using a microprism. **A**, Illustration of laser beam path through a prism implanted into neocortex. The reflective hypotenuse of the prism converts the horizontal imaging plane into a vertical plane. **B**, Flowchart of surgical procedures. Surgeries are separated by  $\geq 7$ –10 d recovery. **C**, Initial cranial window and headpost implant. Headpost and imaging well are designed to permit an unobstructed visual field, access to high-NA water-immersion objectives, and effective light shielding. **D**, Microprism and cranial window assembly and positioning using vacuum line (red arrow). **E**, Left, Wide-field epifluorescence image of a 1 mm prism implanted in visual cortex, focused 1 mm below the cortical surface. Fluorescent expression of AAV-GCaMP3 can be seen through the cranial window (green arrow) and through the prism. Scale bar, 1 mm. Right, Two-photon image taken through the same prism (maximum intensity projection across 15 min of recording) at 205  $\mu\text{m}$  away from the microprism imaging face, 21 d after prism implant. Images spanned  $600 \times 900 \mu\text{m}^2$  of cortex (1 Hz acquisition, 960 nm laser excitation, 45 mW power at sample). Scale bar, 100  $\mu\text{m}$ . This figure was adapted with permission from Goldey et al. (2014) and Andermann et al. (2013), their Fig. 1B.

AAV–GCaMP3) into a precisely targeted region of cortex, and the animal is allowed to recover. In a third surgery, the cranial window is again removed under anesthesia and replaced by a microprism assembly consisting of a microprism glued to three layers of coverglass (Fig. 1D). To improve surgical insertion and the quality of subsequent imaging, a small (~1 mm), a targeted cortical incision is made at the insertion site, and the prism is lowered into the cortex, orthogonal to the plane spanned by the headpost. During insertion, the prism assembly is held from above using a micromanipulator equipped with a custom-made vacuum line (Fig. 1D, right).

Figure 1E (left panel) demonstrates an epifluorescence image focused at the prism face (i.e., 1 mm below the cortical surface), in which the various layers of cortex are visible (Andermann et al., 2013). Subsequent two-photon imaging through the prism reveals individual GCaMP3-expressing neurons throughout the depth of cortex, several hundred microns beyond the imaging face (Fig. 1E, right). The laminar identity of each neuron was estimated by comparing *ex vivo* images of GCaMP3, diamino-phenyl-indol (DAPI), and Nissl staining with *in vivo* baseline GCaMP3 images, which displayed a characteristic laminar expression pattern that peaked in layer 2/3 and in upper layer 5 (Andermann et al., 2013).

Several considerations regarding the above procedure are worth noting in respect to microprism functional imaging. First, while our chronic window implant has some similarities with previous methods (Dombeck et al., 2007; Mostany and Portera-Cailliau, 2008; Holtmaat et al., 2009; Kelly and Majewska, 2010), it allows subsequent removal and replacement of the window, which facilitates several additional surgical procedures. Second, it allows precisely targeted viral delivery and prism insertion into cortical areas that have previously been delineated using epifluorescence imaging in awake mice (Andermann et al., 2011, 2013; Glickfeld et al., 2013). Similarly, replacing our cranial window with one that is glued to a microprism positioned in a predetermined orientation and location has several advantages. This method permits targeted insertion (e.g., in Figure 1E, to posterior V1 near the site of GCaMP3 expression); minimizes damage to large surface vasculature; and allows precise orientation (e.g., toward posterior and lateral cortex; Fig. 1E) to minimize damage to thalamocortical axons from the lateral geniculate nucleus, which traverse cortex from lateral to medial, below layer 6, before ascending into their target cortical column (Antonini et al., 1999). Further, installing the initial cranial window is advantageous before prism implantation, because there is little to

no edema at time of prism implant, thus decreasing bleeding and making insertion more precise.

### Effects of microprism insertion on anatomical and functional properties of nearby neurons

The implantation of a 1 mm prism for chronic imaging involves severing some horizontal cortical connections. Thus, as with live imaging studies of coronal brain sections, it is important to carefully assess whether the local cortical circuitry near the prism imaging face is sufficiently preserved to provide meaningful anatomical and functional data. We therefore undertook a multitiered approach, using functional and anatomical imaging, microelectrode recordings, and histological staining (Andermann et al., 2013). Histological evaluation with staining for hematoxylin and eosin (H&E), Nissl, and DAPI indicated that the imaged regions were comparable with more distant brain tissue 400–500  $\mu\text{m}$  away, and to neurons from nonimplanted mice. Small but significant increases in cell density were observed within the first 50  $\mu\text{m}$  from the prism face, followed by small but significant decreases at 50–100  $\mu\text{m}$  and 100–150  $\mu\text{m}$  away, and a return to normal density beyond 150  $\mu\text{m}$  from the prism. Several weeks after surgery, staining for astrocytes (anti-GFAP) and microglia (anti-CD11b), both indicators of brain trauma, did not show evidence of chronic tissue scarring.

Perhaps the most direct evidence that the functional properties of neurons remain relatively intact following prism insertion came from an assessment of the visual response properties of the same nearby neurons, before and after prism implant (Andermann et al., 2013; Fig. 2). We first measured the visual response properties of neurons through a standard cranial window and then assessed the response properties of the same neurons following insertion of a microprism at a distance of 350  $\mu\text{m}$  away (Fig. 2A, white dashed squares). We used an identical approach across sessions: two-photon imaging of visual responses in a 3D volume of GCaMP3-expressing layer 2/3 neurons through the cranial window in an awake, head-fixed mouse that was free to run on a linear trackball. We found that orientation and direction tuning in the same neurons were mostly stable across days: 2 d before, and 1, 4, and 5 d following prism implant (Andermann et al., 2013; Fig. 2B). These data were also consistent with other multiunit electrophysiological recordings from mouse barrel cortex, which showed that cortical neurons close to the prism face were endogenously active and responsive to whisker stimulation at 10 min, 3 d, and 120 d following prism implant.

## NOTES

Epifluorescence and two-photon imaging demonstrated blood perfusion in intact radial and surface vessels at distances  $>50\ \mu\text{m}$  from the prism face (Andermann et al., 2013; Fig. 2A), which likely helped maintain the functional integrity of local circuits. The insertion of the microprism resulted in the accumulation of some blood at the brain surface and prism surface, which cleared up over the course of several days (Andermann et al., 2013). Thus, the basic cell health and sensory response properties of neurons at  $>100\text{--}150\ \mu\text{m}$  lateral to the prism face (a distance that exceeds the lateral dendritic reach of most pyramidal neurons) were qualitatively similar to what we and others have observed in experiments not involving chronically implanted prisms.

### Chronic functional imaging of cortical neurons through a microprism

Having established that superficial layer neurons located  $>150\ \mu\text{m}$  from the prism face were relatively unaffected by prism insertion, we then recorded

visual responses simultaneously from large numbers of neuronal cell bodies across all layers of mouse V1 using the prism method (Andermann et al., 2013; Fig. 3A). To visualize the density of responsive neurons, we plotted a maximum intensity projection of increases in GCaMP3 calcium indicator fluorescence across average response maps for each of the 96 visual stimulus conditions. Neurons in all cortical layers demonstrated orientation tuning curves generally similar to previous electrophysiological reports (Niell and Stryker, 2008; Fig. 3B). Orientation tuning curves imaged through the prism were stable across multiple days (Fig. 3B), consistent with previous studies in layer 2/3 of mouse V1 (Mank et al., 2008; Andermann et al., 2010). Figure 3C illustrates the orientation preference of simultaneously recorded, orientation-tuned neurons throughout the depth of mouse V1 (Andermann et al., 2013). Consistent with previous reports in superficial cortical layers, we did not find any evidence of columnar clustering of orientation preference in any cortical layer (Andermann et al., 2013).

### Microprism imaging of long-range axonal boutons

A unique advantage of two-photon imaging is the ability to monitor subcellular structures, such as axonal boutons. Recently, we and others have described functional imaging of long-range projection axons using GCaMP3 in awake mice (Petreanu et al., 2012; Glickfeld et al., 2013). Because of the small size of individual axons and synaptic boutons, functional imaging of axons has been restricted to superficial depths in cortex ( $\sim 0\text{--}150\ \mu\text{m}$  deep). However, many classes of projection neurons selectively innervate deep cortical layers (Petreanu et al., 2009).

To determine whether the use of a microprism could enable monitoring of long-range axonal activity deep within the cortex, we made a small injection of GCaMP3 into area V1 (Glickfeld et al., 2013) and inserted the prism into the posteromedial secondary visual cortical area (PM), an area densely innervated by V1 axons, with the prism oriented to face area V1 (Fig. 3D). We observed robust single-trial visual responses of individual boutons at depths of  $480\text{--}510\ \mu\text{m}$  below the cortical surface (putative layer 5) during presentation of stimuli at multiple temporal frequencies and spatial frequencies at 1 d postimplant (Fig. 3E). Thus, this method extends *in vivo* functional imaging of axonal arbors (Petreanu et al., 2012; Glickfeld et al., 2013) to arbors that innervate deeper cortical layers (Petreanu et al., 2009). Further, the study of long-range projection axons via a microprism represents a less invasive application of this method with fewer caveats than for imaging of cell bodies near the prism face. That is,

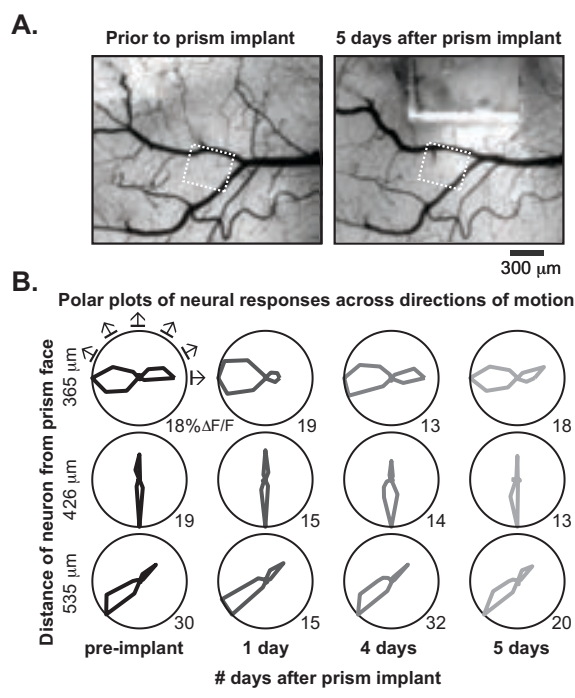


**Figure 2.** Comparison of cortical neuron visual response properties, before and following prism implant. **A**, Bright-field image through a cranial window, before and 4 d after prism implant. Scale bar,  $300\ \mu\text{m}$ . **B**, Comparison of functional properties of neurons using two-photon GCaMP3 calcium imaging through the surface cranial window, both before and following insertion of a prism at a nearby location. Polar plots of normalized visual responses to 12 directions of motion (arrows in top left polar plot) in 3 example neurons at varying distances from the prism face, across 4 sessions (2 d before, and 1, 4, and 5 d after prism implant). Peak response amplitudes (%  $\Delta F/F$ ) are noted at bottom right. This figure was adapted with permission from Andermann et al. (2013), their Fig. 2.

although damage to long-range axonal boutons near the prism face cannot be ruled out, these boutons report the activity of neurons whose dendrites are safely located millimeters from the prism implant.

### High-speed cellular imaging of endogenous activity across all cortical depths

In addition to functional mapping of average evoked responses, simultaneous imaging of all cortical layers enabled direct examination of interlaminar neural

dynamics, on a trial-by-trial basis, in awake mice that stood or ran on a linear trackball (Fig. 4). Using a fast resonance scanning two-photon microscope ( $\sim 32$  Hz frame rate,  $720 \mu\text{m} \times 720 \mu\text{m}$ ,  $256 \times 240$  pixels/frame) (Bonin et al., 2011; Andermann et al., 2013), we were able to measure endogenous neural activity simultaneously in 208 neurons spanning all 6 cortical layers of V1 (Fig. 4A). Data were collected in near complete darkness, 38 d after prism implant,  $\sim 140 \mu\text{m}$  from the prism face. This dataset provided a proof-of-principle demonstration of the capacity of chronic

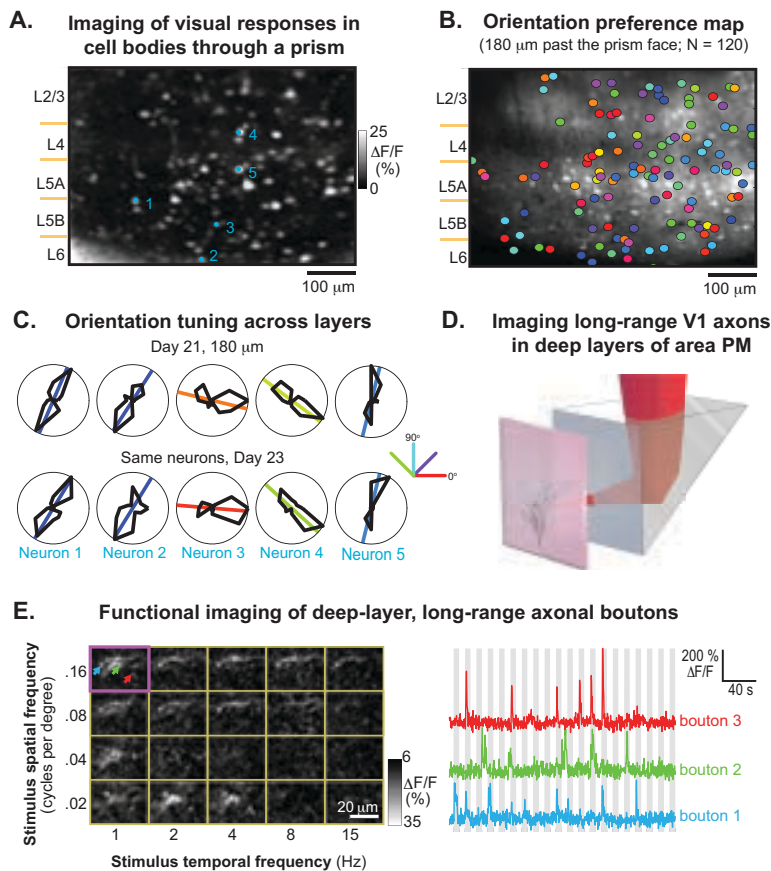


**Figure 3.** Long-term functional imaging of cell bodies and axons across all cortical layers in awake mouse V1. **A**, Maximum intensity projection of fractional change in GCaMP3 fluorescence ( $\Delta F/F$ ), computed across a stack of single-condition average visually evoked response maps for 96 different stimulus conditions (varying in stimulus location, orientation, and spatial/temporal frequency). Data were collected 23 d after prism implant,  $180 \mu\text{m}$  from the prism face. Visually responsive neurons (white spots) were evident in all cortical layers. Scale bar,  $100 \mu\text{m}$ . **B**, These data were used to generate cellular maps of visual orientation preference (colored circles) across cortical layers. Scale bar,  $100 \mu\text{m}$ . **C**, Neurons across all layers (numbered in blue in **A**) showed sharp orientation tuning that was consistent at 21 d and 23 d following prism implant. Orientation tuning curves were averaged across stimulus locations, spatial and temporal frequencies, and normalized by peak response. Colored lines and colored inset in polar plots indicate estimated orientation preference. Neurons 1–5 had strong responses in both sessions, exceeding  $30\% \Delta F/F$  for the preferred orientation. **D**, To extend functional imaging of long-range cortico-cortical axonal arbors in awake mice (Glickfeld et al., 2013) into deeper cortical layers, AAV-GCaMP3 was injected into area V1, and a microprism was subsequently inserted at the site of V1 innervation of posteromedial secondary visual area PM. **E**, Robust visually evoked activity was observed in V1 axonal boutons innervating deeper layers of area PM ( $480$ – $510 \mu\text{m}$  below the cortical surface; 1 d postimplant). Left, Response maps to upward-drifting stimuli varying in spatial and temporal frequency (Glickfeld et al., 2013). Distinct boutons (white spots) were activated by different visual stimuli. Purple square at top left: Maximum intensity projection of all response maps; colored arrows point to 3 active boutons. Right, Timecourses of these 3 individual boutons demonstrated robust single-trial responses to individual visual stimuli (gray bars) varying in spatial and temporal frequency. Minimal fluorescence cross-talk or photo-bleaching was observed. Scale bar,  $20 \mu\text{m}$ . This figure was adapted with permission from Andermann et al. (2013), their Figs. 3A–C and 5D, F, and Goldey et al. (2014).

## NOTES

microprism imaging for examining concurrent changes in neural activity across layers following the onset of running bouts. We observed neurons whose average endogenous activity increased at running onset (also observed by Keller et al., 2012) and other neurons whose activity consistently decreased at running onset. Intriguingly, the strongest suppression of endogenous activity was observed in several layer 6 neurons (Andermann et al., 2013).

To better understand these changes in neuronal activity across layers, we also examined changes in

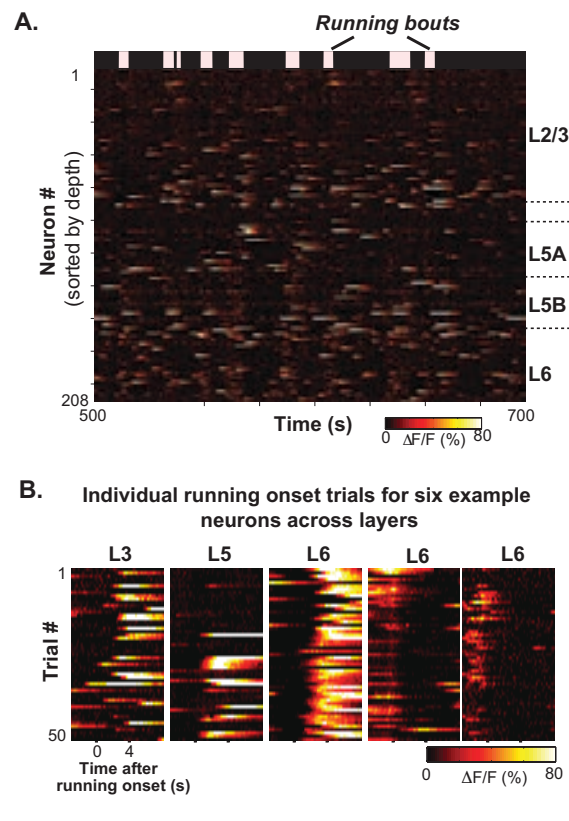


**Figure 4.** Simultaneous cellular imaging of running-related changes in activity across all cortical layers. Rapid endogenous dynamics of cortical activity, imaged at 32 Hz across entire cortical columns in awake mice that were free to run on a linear trackball in near complete darkness. The series of images recorded in a 20 min session was downsampled to 16 Hz and coregistered. **A**, >200 neurons in the field of view were endogenously active and were monitored simultaneously across layers. Pink blocks at top indicate bouts of locomotion. **B**, Diverse changes in neural activity at running onset were observed across cortical layers, including many deep-layer neurons exhibiting strong running-induced suppression. For 5 of these neurons, endogenous activity is plotted for all 53 individual locomotion onset trials (neuron depth from left to right: 288  $\mu\text{m}$ , 554  $\mu\text{m}$ , 581  $\mu\text{m}$ , 642  $\mu\text{m}$ , and 688  $\mu\text{m}$ ). Note that a neuron's activity could be highly variable across trials. Despite this high trial-to-trial variability, pairs of neurons within and across layers did not show consistently strong covariation in activity across trials (Andermann et al., 2013). This figure was adapted from Andermann et al. (2013), their Figs. 6D, G.

activity across individual running onsets (Fig. 4B). While such activity changes typically had the same sign for each neuron, different neurons demonstrated different degrees of variability among trials, and most pairs of neurons had relatively low trial-to-trial covariability both within and across layers (Andermann et al., 2013). These data illustrate the rich repertoire of interlaminar and intralaminar neural dynamics accessible using microprism-based columnar recordings in behaving animals.

### Challenges of the prism approach

We were able to routinely record from the same large set of cell bodies across all cortical layers across days and weeks in awake mice using calcium imaging through a microprism (Andermann et al., 2013). Although images could be obtained on the day of surgery (Chia and Levene, 2009b), they were sometimes less clear and required somewhat higher laser power than images obtained later on. In these cases, imaging clarity improved over subsequent days. This initial clouding could have been caused in part by gliosis (Barretto et al., 2011). However, the timecourse of immediate clouding and subsequent improvement in clarity was more consistent with clearing of blood at the prism and cortical surfaces (Chia and Levene, 2009b; Andermann et al., 2013).

As discussed in detail elsewhere (Andermann et al., 2013), the chronic insertion of a 1 mm microprism into the cortex is clearly accompanied by damage to local neural processes and to the neurovascular unit. Therefore, care must be taken when interpreting neural data and validating results against known benchmarks (Andermann et al., 2013). Importantly, concerns regarding damage to local circuitry should decrease with increasing distance from the prism face to the focal plane. This distance (currently 100–350  $\mu\text{m}$  using our approach) can likely be further extended by implementing adaptive optical correction of aberrations (Ji et al., 2012). Despite the aforementioned challenges, microprism imaging is a relatively simple and straightforward tool that can be used on any conventional multiphoton microscope at a cost of approximately \$50 per prism.

### Technical Outlook and Applications

Advances in a variety of optical techniques for neurophysiology hold promise for rapid advances in systems neuroscience research. The chronic two-photon calcium microprism imaging technique presented here can expand the capabilities of two-photon functional imaging by allowing simultaneous access to multiple genetically, chemically, and

anatomically defined neuronal populations throughout the depth of cortex. Also, the large field of view available using microprisms enables high-throughput functional imaging of hundreds of neurons within local circuits of mammalian cortex. Placing the prism face at the cortical surface of extremely medial or lateral cortical regions (Fig. 5)

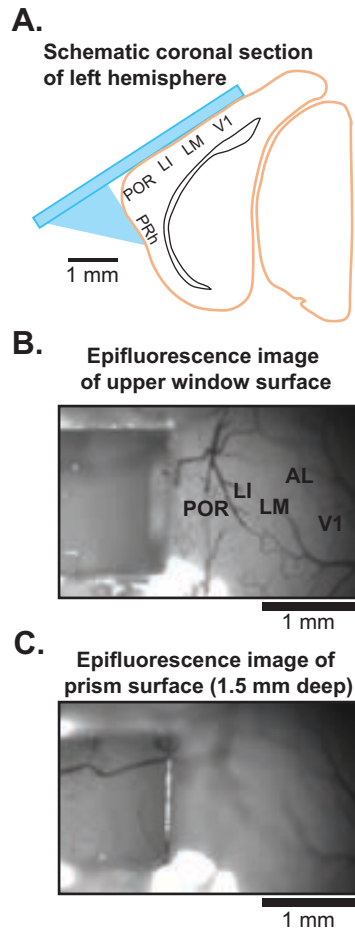


**Figure 5.** Chronic imaging of very lateral cortex using a prism pressed against the cortical surface. The lateral cortical surface is difficult to image in awake mice using standard methods because of challenges involving lateral bone structure and use of water-immersion objectives at an extreme tilt. **A**, To image more laterally, we chronically implanted a 1.5 mm microprism affixed to a standard round 5 mm diameter cranial window, such that this window allowed standard imaging of dorsal cortex, while the prism imaging face was pressed against the external surface of lateral cortex. We used an adult transgenic mouse expressing GCaMP3 in cortical pyramidal neurons (Emx1-Cre:Ai38) (Zariwala et al., 2012). **B**, Epifluorescence image of the dorsal cortical surface. Visual mapping in the awake state showed robust visual responses in dorsal cortex (not shown) and allowed delineation of cortical areas. **C**, Epifluorescence image at 1.5 mm below the dorsal cortical surface revealed intact vasculature at the lateral cortical surface (putative perirhinal cortex). AL, anterolateral; LI, laterointermediate; LM, lateromedial; POR, postrhinal; PRh, perirhinal; V1, primary visual cortex. Scale bars: **A–C**, 1 mm. Images and mapping courtesy of N. Jikomes.

should also prove useful for noninvasive imaging of superficial cortical activity in hard-to-reach brain regions. Prism implants should also be easily adaptable for reaching deeper cortical layers in carnivores and primates. Finally, efforts to combine prisms with GRIN lenses hold promise for two-photon imaging in deep subcortical brain structures with decreased tissue damage at the imaging plane (Kim et al., 2013).

Optogenetic methods for one-photon and two-photon (Fenko et al., 2011; Prakash et al., 2012; Begue et al., 2013) excitation or suppression of individual neurons or local neural populations are also improving rapidly. Such methods stand to benefit greatly from the technique presented here, which should enable repeated photo-stimulation of neurons across cortical layers, in combination with concurrent monitoring of local neural activity. Ultimately, continued integration of microprism imaging with the above methods should provide a powerful yet relatively simple strategy for understanding interlaminar flow of information through cortical circuits in behaving animals.

In the future, the use of higher-speed two-photon imaging, coupled with expression of recent, promising genetically encoded voltage indicators (Han et al., 2013; St-Pierre et al., 2014), may allow observation of the electrical flow of neural signals at cellular resolution in a behaving animal. In addition, future analyses of trial-to-trial covariability in activity of neurons across cortical layers *in vivo* may help identify interlaminar assemblies within a cortical column.

## Acknowledgments

The authors would like to thank the Levene lab (M. Levene, N. Gilfoy, M. Wölfel), McCormick lab (D. McCormick, R. Sachdev), Reid lab (in particular, R.C. Reid, A. Kerlin, L. Glickfeld, V. Bonin, D. Roumis), and Andermann lab (in particular, N. Jikomes) for their collaborative contributions toward the development of two-photon functional imaging of cortical neurons using microprisms, and for useful discussions. We thank J. Maunsell for sharing his surgical rig during initial stages of these procedures' development. We thank Loren L. Looger and the Janelia Farm Research Campus of the Howard Hughes Medical Institute for providing AAV-GCaMP3 via the Penn Vector Core at University of Pennsylvania's Perelman School of Medicine.

The writing of this manuscript was supported by grants from the Smith Family Foundation, the Pew Scholars Program in the Biomedical Sciences, the Klarman Family Foundation, the Boston Nutrition and Obesity Research Center, the Association for Aging Research

## NOTES

New Investigator Award in Alzheimer's Disease, and the Harvard–MIT Joint Research Grants Program (M.A.). Sections of this chapter were adapted from two recently published articles: Andermann et al. (2013) and Goldey et al. (2014).

## References

- Adesnik H, Scanziani M (2010) Lateral competition for cortical space by layer-specific horizontal circuits. *Nature* 464:1155–1160.
- Amir W, Carriles R, Hoover EE, Planchon TA, Durfee CG, Squier JA (2007) Simultaneous imaging of multiple focal planes using a two-photon scanning microscope. *Opt Lett* 32:1731–1733.
- Andermann ML, Kerlin AM, Reid RC (2010) Chronic cellular imaging of mouse visual cortex during operant behavior and passive viewing. *Front Cell Neurosci* 4:1–16.
- Andermann ML, Kerlin AM, Roumis DK, Glickfeld LL, Reid RC (2011) Functional specialization of mouse higher visual cortical areas. *Neuron* 72:1025–1039.
- Andermann ML, Gilfoy NB, Goldey GJ, Sachdev RN, Wolfel M, McCormick DA, Reid RC, Levene MJ (2013) Chronic cellular imaging of entire cortical columns in awake mice using microprisms. *Neuron* 80:900–913.
- Antonini A, Fagiolini M, Stryker MP (1999) Anatomical correlates of functional plasticity in mouse visual cortex. *J Neurosci* 19:4388–4406.
- Barretto RP, Ko TH, Jung JC, Wang TJ, Capps G, Waters AC, Ziv Y, Attardo A, Recht L, Schnitzer MJ (2011) Time-lapse imaging of disease progression in deep brain areas using fluorescence microendoscopy. *Nat Med* 17:223–228.
- Begue A, Papagiakoumou E, Leshem B, Conti R, Enke L, Oron D, Emiliani V (2013) Two-photon excitation in scattering media by spatiotemporally shaped beams and their application in optogenetic stimulation. *Biomed Opt Express* 4:2869–2879.
- Berenyi A, Somogyvari Z, Nagy AJ, Roux L, Long JD, Fujisawa S, Stark E, Leonardo A, Harris TD, Buzsáki G (2014) Large-scale, high-density (up to 512 channels) recording of local circuits in behaving animals. *J Neurophysiol* 111:1132–1149.
- Bock DD, Lee WC, Kerlin AM, Andermann ML, Hood G, Wetzel AW, Yurgenson S, Soucy ER, Kim HS, Reid RC (2011) Network anatomy and *in vivo* physiology of visual cortical neurons. *Nature* 471:177–182.
- Bonin V, Histed MH, Yurgenson S, Reid RC (2011) Local diversity and fine-scale organization of receptive fields in mouse visual cortex. *J Neurosci* 31:18506–18521.
- Cheng A, Goncalves JT, Golshani P, Arisaka K, Portera-Cailliau C (2011) Simultaneous two-photon calcium imaging at different depths with spatiotemporal multiplexing. *Nat Methods* 8:139–142.
- Chia TH, Levene MJ (2009a) *In vivo* imaging of deep cortical layers using a microprism. *J Vis Exp* 30. doi:10.3791/1509.
- Chia TH, Levene MJ (2009b) Microprisms for *in vivo* multilayer cortical imaging. *J Neurophysiol* 102:1310–1314.
- Chia TH, Levene MJ (2010) Multi-layer *in vivo* imaging of neocortex using a microprism. *Cold Spring Harb Protoc* 2010;8:pdb.prot5476.
- Dombeck DA, Khabbaz AN, Collman F, Adelman TL, Tank DW (2007) Imaging large-scale neural activity with cellular resolution in awake, mobile mice. *Neuron* 56:43–57.
- Fenko L, Yizhar O, Deisseroth K (2011) The development and application of optogenetics. *Annu Rev Neurosci* 34:389–412.
- Glickfeld LL, Andermann ML, Bonin V, Reid RC (2013) Cortico-cortical projections in mouse visual cortex are functionally target specific. *Nat Neurosci* 16:219–226.
- Gobel W, Kampa BM, Helmchen F (2007) Imaging cellular network dynamics in three dimensions using fast 3D laser scanning. *Nat Methods* 4:73–79.
- Goldey GJ, Roumis DK, Glickfeld LL, Kerlin AM, Reid RC, Bonin V, Schafer D, Andermann ML. Long-term imaging in awake mice using removable cranial windows. *Nat Protocols*, in press. doi:10.1038/nprot.2014.165.
- Grewe BF, Voigt FF, van 't Hoff M, Helmchen F (2011) Fast two-layer two-photon imaging of neuronal cell populations using an electrically tunable lens. *Biomed Opt Express* 2:2035–2046.
- Han Z, Jin L, Platasa J, Cohen LB, Baker BJ, Pieribone VA (2013) Fluorescent protein voltage probes derived from ArcLight that respond to membrane voltage changes with fast kinetics. *PLoS One* 8:e81295.

- Holtmaat A, Bonhoeffer T, Chow DK, Chuckowree J, De Paola V, Hofer SB, Hubener M, Keck T, Knott G, Lee WC, Mostany R, Mrsic-Flogel TD, Nedivi E, Portera-Cailliau C, Svoboda K, Trachtenberg JT, Wilbrecht L (2009) Long-term, high-resolution imaging in the mouse neocortex through a chronic cranial window. *Nat Protoc* 4:1128–1144.
- Horton NG, Wang K, Kobat D, Clark CG, Wise FW, Schaffer CB, Xu C (2013) *In vivo* three-photon microscopy of subcortical structures within an intact mouse brain. *Nature Photonics* 7:205–209.
- Ji N, Sato TR, Betzig E (2012) Characterization and adaptive optical correction of aberrations during *in vivo* imaging in the mouse cortex. *Proc Natl Acad Sci USA* 109:22–27.
- Jung JC, Mehta AD, Aksay E, Stepnoski R, Schnitzer MJ (2004) *In vivo* mammalian brain imaging using one- and two-photon fluorescence microendoscopy. *J Neurophysiol* 92:3121–3133.
- Keller GB, Bonhoeffer T, Hubener M (2012) Sensorimotor mismatch signals in primary visual cortex of the behaving mouse. *Neuron* 74:809–815.
- Kelly EA, Majewska AK (2010) Chronic imaging of mouse visual cortex using a thinned-skull preparation. *J Vis Exp* 44:2060.
- Kerlin AM, Andermann ML, Berezovskii VK, Reid RC (2010) Broadly tuned response properties of diverse inhibitory neuron subtypes in mouse visual cortex. *Neuron* 67:858–871.
- Kim JK, Choi JW, Yun SH (2013) 350- $\mu\text{m}$  side-view optical probe for imaging the murine brain *in vivo* from the cortex to the hypothalamus. *J Biomed Opt* 18:50502.
- Levene MJ, Dombek DA, Kasischke KA, Molloy RP, Webb WW (2004) *In vivo* multiphoton microscopy of deep brain tissue. *J Neurophysiol* 91:1908–1912.
- MacLean JN, Fenstermaker V, Watson BO, Yuste R (2006) A visual thalamocortical slice. *Nat Methods* 3:129–134.
- Mank M, Santos AF, Drenth S, Mrsic-Flogel TD, Hofer SB, Stein V, Hendel T, Reiff DF, Levelt C, Borst A, Bonhoeffer T, Hubener M, Griesbeck O (2008) A genetically encoded calcium indicator for chronic *in vivo* two-photon imaging. *Nat Methods* 5:805–811.
- Mittmann W, Wallace DJ, Czubayko U, Herb JT, Schaefer AT, Looger LL, Denk W, Kerr JN (2011) Two-photon calcium imaging of evoked activity from L5 somatosensory neurons *in vivo*. *Nat Neurosci* 14:1089–1093.
- Mostany R, Portera-Cailliau C (2008) A craniotomy surgery procedure for chronic brain imaging. *J Vis Exp* 12:680.
- Murayama M, Perez-Garci E, Luscher HR, Larkum ME (2007) Fiberoptic system for recording dendritic calcium signals in layer 5 neocortical pyramidal cells in freely moving rats. *J Neurophysiol* 98:1791–1805.
- Niell CM, Stryker MP (2008) Highly selective receptive fields in mouse visual cortex. *J Neurosci* 28:7520–7536.
- Olsen SR, Bortone DS, Adesnik H, Scanziani M (2012) Gain control by layer six in cortical circuits of vision. *Nature* 483:47–52.
- Petersen CC, Sakmann B (2001) Functionally independent columns of rat somatosensory barrel cortex revealed with voltage-sensitive dye imaging. *J Neurosci* 21:8435–8446.
- Petreaanu L, Mao T, Sternson SM, Svoboda K (2009) The subcellular organization of neocortical excitatory connections. *Nature* 457:1142–1145.
- Petreaanu L, Gutnisky DA, Huber D, Xu NL, O'Connor DH, Tian L, Looger L, Svoboda K (2012) Activity in motor-sensory projections reveals distributed coding in somatosensation. *Nature* 489:299–303.
- Prakash R, Yizhar O, Grewe B, Ramakrishnan C, Wang N, Goshen I, Packer AM, Peterka DS, Yuste R, Schnitzer MJ, Diesseroth K (2012) Two-photon optogenetic toolbox for fast inhibition, excitation and bistable modulation. *Nat Methods* 9:1171–1179.
- Quirin S, Jackson J, Peterka DS, Yuste R (2014) Simultaneous imaging of neural activity in three dimensions. *Front Neural Circuits* 8:29.
- Sakata S, Harris KD (2009) Laminar structure of spontaneous and sensory-evoked population activity in auditory cortex. *Neuron* 64:404–418.
- Sanchez-Vives MV, McCormick DA (2000) Cellular and network mechanisms of rhythmic recurrent activity in neocortex. *Nat Neurosci* 3:1027–1034.
- St-Pierre F, Marshall JD, Yang Y, Gong Y, Schnitzer MJ, Lin MZ (2014) High-fidelity optical reporting of neuronal electrical activity with an ultrafast fluorescent voltage sensor. *Nat Neurosci* 17:884–889.

## NOTES

Theer P, Hasan MT, Denk W (2003) Two-photon imaging to a depth of 1000  $\mu\text{m}$  in living brains by use of a Ti:Al<sub>2</sub>O<sub>3</sub> regenerative amplifier. *Opt Lett* 28:1022–1024.

Thomson AM (2010) Neocortical layer 6, a review. *Front Neuroanat* 4:13.

Trachtenberg JT, Chen BE, Knott GW, Feng G, Sanes JR, Welker E, Svoboda K (2002) Long-term *in vivo* imaging of experience-dependent synaptic plasticity in adult cortex. *Nature* 420:788–794.

Zariwala HA, Borghuis BG, Hoogland TM, Madisen L, Tian L, De Zeeuw CI, Zeng H, Looger LL, Svoboda K, Chen TW (2012) A Cre-dependent GCaMP3 reporter mouse for neuronal imaging *in vivo*. *J Neurosci* 32:3131–3141.

# **Two-Photon Calcium Imaging in the Macaque Monkey**

Kristina J. Nielsen, PhD

---

Zanvyl Krieger Mind/Brain Institute  
Department of Neuroscience  
Johns Hopkins University, Baltimore, Maryland



## Introduction

The nonhuman primate has proven to be an invaluable animal model for neuroscience research. Nonhuman primates such as the Rhesus macaque have a complex brain that is organized similarly to the human brain (Sereno and Tootell, 2005). In addition, monkeys can be trained on the complex tasks necessary to study the neural underpinnings of such complicated processes as perception, cognition, and decision making. Because these are the types of behaviors affected by mental disorders, the monkey will remain a crucial animal model for investigating brain function. To date, a wealth of research has established which areas in the monkey brain are likely to be involved in a particular task, as well as the tuning properties of neurons in these areas. Going forward, we will have to build on this knowledge to pursue questions such as: How are the neural circuits within and between these areas organized? What is the function of their individual elements, and how do they interact? Only by solving these puzzles will we be able to address what goes awry in mental disorders.

Investigating these issues is complicated by the fact that neural circuits are formed with a high degree of specificity and on very fine scales. Thus, we will need tools that operate at a resolution appropriate to appreciate the fine-scale organization of neural circuits. Two-photon microscopy (Goeppert-Mayer, 1931; Denk et al., 1990) fills an important technological gap in this respect. At its coarsest resolution, two-photon calcium imaging allows the simultaneous recording of activity of tens to hundreds of neighboring neurons while maintaining single-neuron resolution. At the finest resolution, responses of individual spines on a single dendrite can be investigated. (General reviews of two-photon microscopy can be found in So et al., 2000; Helmchen and Denk, 2005; Svoboda and Yasuda, 2006; and Kerr and Denk, 2008.) No other technique currently is able to operate at these resolutions *in vivo*.

Two-photon calcium imaging is by now routinely used in anesthetized and even awake mice. In contrast, only few studies have applied two-photon imaging to investigate brain functions in larger animals, in particular, monkeys (Nauhaus et al., 2012a; Ikezoe et al., 2013). This chapter will describe the necessary steps to perform two-photon microscopy in monkeys, including some of the commonly encountered complications, and discuss how to interpret the data. Most of the text will focus on an established imaging paradigm using an injectable calcium dye, Oregon Green BAPTA-1AM (OGB), in acute experiments in anesthetized animals. Genetically encoded calcium indicators (GECIs) and experiments in

awake animals are discussed in the last section. This text does not include more general details on how to perform acute experiments in anesthetized monkeys, such as the choice of anesthesia, paralysis, or vital-sign monitoring. For more information on these issues, refer, for example, to Nauhaus et al. (2012a).

## Setup

### Choice of two-photon microscope

A large number of two-photon microscopes are commercially available, and are used to perform calcium imaging in mice. However, the size and curvature of the monkey brain place specific demands on the two-photon microscope. In the monkey, most brain areas are located laterally or posteriorly enough that their surface is at a significant angle relative to the horizontal plane in which imaging is typically performed. In some cases, it may be feasible to rotate the animal's head to bring the brain area of interest into the horizontal plane. Often, this is not possible, either because the angle difference is too large (e.g., posterior V1 is tilted approximately 50° relative to the horizontal) or because rotating the animal's head would interfere with stimulus presentation (e.g., rotating the head downward poses problems for visual stimulus presentation). In these cases, the only solution is to rotate the microscope and to image in a plane tilted relative to the horizontal plane. Increasingly more commercial two-photon microscopes offer this capability. Another important consideration in selecting a two-photon microscope for imaging in larger animals, such as the monkey, is the amount of space available under the objective. This space has to be large enough to fit the animal's head, or (as in our typical setup) the animal and a stereotaxic frame.

### Specific imaging equipment

In addition to the usual equipment necessary for acute experiments in anesthetized animals, we use two specially designed pieces of hardware: an imaging well and a simplified stereotaxic frame. The imaging well serves the following purpose: The objectives typically used for two-photon microscopy are water-immersion objectives, and therefore require water or artificial CSF (ACSF) between imaging region and objective. This can be relatively easily achieved when imaging in the horizontal plane. However, once the microscope has been rotated and imaging is performed at an angle, a specially designed imaging well becomes necessary to hold water between imaging region and objective. Our imaging well consists of a large metal plate with a hole in the center (Fig. 1A). This metal plate is attached to the skull using dental cement. During imaging, a plastic

## NOTES

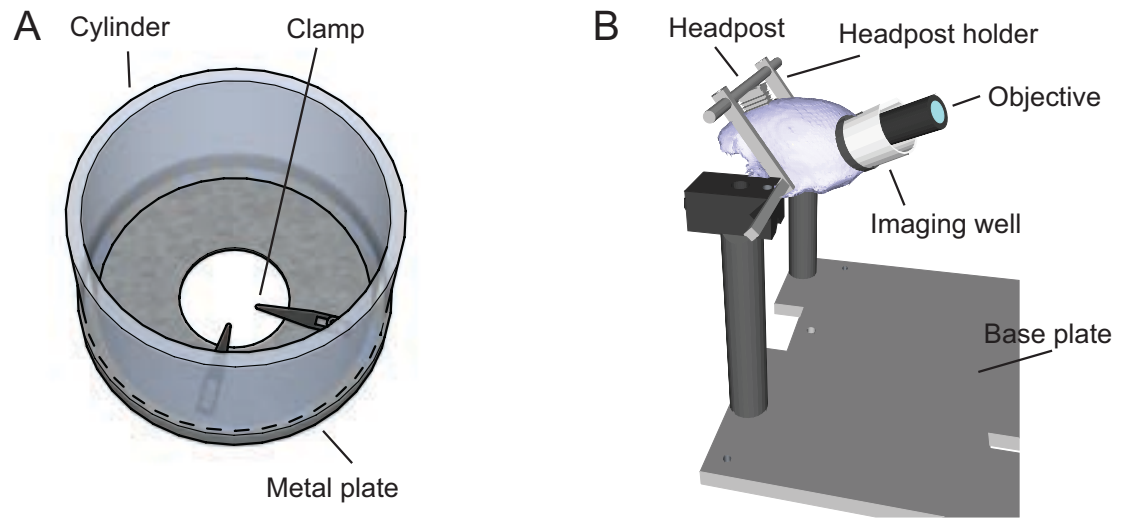


**Figure 1.** Imaging equipment. **A**, Imaging well, showing the metal plate cemented to the animal's head, clamps used to stabilize the brain, and the cylinder used for water immersion of the objective. **B**, Imaging stereotax. The drawing illustrates how stereotax, head holder, and imaging well are configured during an imaging experiment.

cylinder is fitted into the well, and the interface of cylinder and well is sealed with bone wax to prevent water leakage. The cylinder can then be filled with enough ACSF to cover the imaging region. The cylinder can be removed for easy access to the skull for surgical and other procedures. We also use the imaging well to stabilize the brain during imaging (see Minimizing Movement Artifacts, below).

The second specialized piece of equipment in the imaging setup is a simplified version of a stereotaxic frame (Fig. 1B). The stereotaxic frame is designed to rigidly hold the animal's head while being small enough not to interfere with the two-photon microscope. It consists of a metal base plate, large enough to support the animal's body, and two posts at one end. These posts initially hold the animal's head via attachments for ear bars, eye bars, and a palate bar. This setup provides sufficient stability to perform initial surgeries. To further increase stability during imaging, we cement a headpost to the skull at the beginning of each acute experiment. For the remainder of the experiment, the head is then rigidly held in place by connecting the headpost to the stereotax posts.

### Dye Loading

Multiple calcium dyes are available, of which OGB has been most commonly used. OGB has been the calcium dye of choice because of a number of advantages over other dyes: Labeling neurons with OGB is feasible via pressure injection into the brain (Stosiek et al., 2003). Furthermore, because of its acetoxymethyl (AM) ester group, OGB is not

fluorescent until it is transferred into cells and the AM group is cleaved, which helps to reduce background fluorescence (Tsien, 1981). OGB is stable in the cells for a relatively long period of time (in some cases, up to 12 h) and has a signal-to-noise ratio (SNR) sufficient to detect even single action potentials (Kerr et al., 2005; Chen et al., 2013). The basic protocol for OGB injections has been described in depth previously (Stosiek et al., 2003; Garaschuk et al., 2006) and widely applies to monkeys. Listed below are the most important steps of OGB injections in the monkey:

- (1) *OGB and SR101 solution*: OGB labels both neurons and astrocytes. Sulforhodamine 101 (SR101), a red fluorescent dye that selectively labels astrocytes (Nimmerjahn et al., 2004), is therefore often added to the OGB injection solution. For the monkey, our typical injection solution consists of 2 mM OGB with 10% DMSO, 2% Pluronic F-127, and 25% SR101 (all from Life Technologies, Grand Island, NY).
- (2) *Craniotomy*: The hole in the imaging well allows access to a large skull region. We usually make small craniotomies ( $\sim 5 \times 5$  mm) within its perimeter. Each craniotomy is used once to attempt dye loading. If the dye loading is unsuccessful, or after completion of data collection, the next craniotomy is made. Craniotomies are kept relatively small to help stabilize the brain (see Minimizing Movement Artifacts, below). It is important to thin the skull around the perimeter of each craniotomy to be

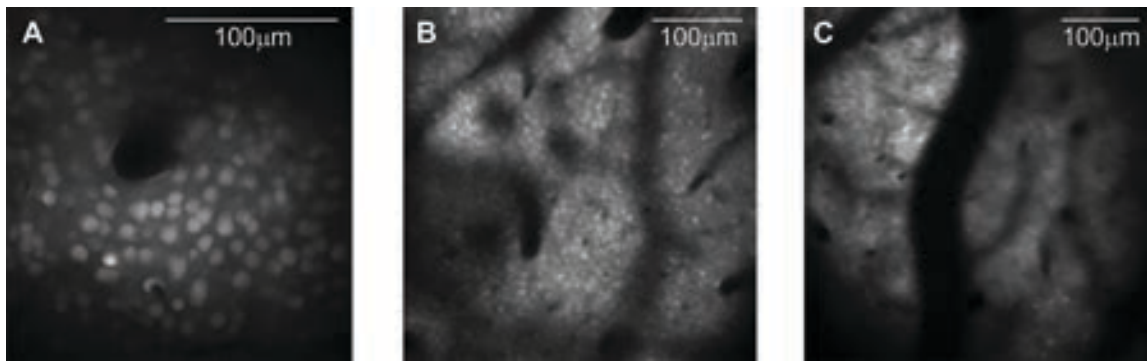


**Figure 2.** Example OGB loading in monkey V1. *A*, Fine-scale imaging using a 40 $\times$  objective, showing a large number of labeled neurons. *B*, Large-scale imaging using a 16 $\times$  objective. *C*, Failure of OGB loading. Notice the uniform label in *C* versus the visible cell bodies in *B*. Data collected as part of Nauhaus et al. (2012a). Scale bars, *A–C*, 100  $\mu$ m.

able to place the objective close enough (within its working distance [WD]) from the brain.

- (3) *Durotomy*: Monkey dura is opaque and needs to be removed before imaging. Usually, one durotomy of approximately  $3 \times 3$  mm is made per craniotomy, trying to avoid major blood vessels in the dura. Care needs to be taken to avoid bleeding while cutting through the last layer of dura: Blood touching the brain seems to interfere with dye loading.
- (4) *Dye injection*: Dyes are pressure-injected into the brain using a Picospritzer (Parker Hannifin, Hollis, NH) and glass pipettes with a relatively blunt taper and a tip size of  $\sim 5$   $\mu$ m. We have found that the blunt taper helps with preventing backflow of the dye along the track of the pipette and onto the surface of the brain. Tip sizes smaller than  $\sim 4$   $\mu$ m tend to clog, whereas larger tip sizes tend to lead to backflow. Pipettes are inserted into the brain at an angle of  $35^\circ$ – $45^\circ$  relative to the surface of the brain, and the dye is injected at a depth of  $\sim 300$ – $400$   $\mu$ m. The progress of each injection is monitored by observing the flow of SR101 into the brain. This is a crucial step of the procedure, as it ensures that (a) the pipette is not clogged, and (b) dye is not flowing back onto the surface of the brain. The latter needs to be avoided, as staining the surface of the brain with SR101 drastically degrades imaging quality. Unlike OGB, SR101 is fluorescent before entering a cell. Monitoring the dye spread during injection is thus feasible by observing SR101 fluorescence using the two-photon microscope. Alternatively, most two-photon microscopes have an epifluorescence path that will allow observation of the dye using low power, dry objectives. Multiple injections can be made within the same durotomy, as long as they

are done within a short amount of time ( $\sim 1$  h) after each other and after making the durotomy. Reloading OGB into a previously labeled, “old” durotomy appears to not be feasible.

The biggest challenge with OGB loading in monkeys is the observation that, in many cases, OGB is taken up not only by neurons, but also by the neuropil that makes up the extracellular space. This results in uniform OGB fluorescence throughout the entire imaging region (Fig. 2). As a consequence, neurons can no longer be discriminated from the surrounding neuropil. It appears that the likelihood of excessive OGB label in the neuropil strongly increases with animal age, making younger animals better suited for two-photon microscopy. Similar observations have been made in mice (Eichhoff et al., 2008). The reason for this increased label in the neuropil is unclear, but one possible explanation is an increase in acetylcholinesterase activity in the neuropil with age. It remains to be seen whether coinjection of esterase blockers such as eserine, which has been used to improve loading of OGB in the retina (Kurth-Nelson et al., 2009; Srien et al., 2012), could prevent the neuropil loading of OGB without interfering with brain function.

### Minimizing Movement Artifacts

Besides complications with OGB loading, the largest challenge in performing two-photon microscopy in monkeys is posed by artifacts caused by brain movements. In the anesthetized monkey, the largest sources of movement are breathing and pulse. Breathing usually causes vertical displacements of the brain, whereas the pulse tends to be correlated with horizontal displacements. Of these two artifacts, the vertical movements are particularly disruptive for imaging because they cause cells to move in and out of the imaging plane. Because data cannot be collected from a cell outside the imaging plane, vertical artifacts

## NOTES

cannot be corrected offline. It is thus necessary to eliminate at least the vertical brain movements as much as possible before collecting data.

In our experience, vertical brain movements can be minimized using the following approach: First, the brain region to be imaged is covered with a thin layer of 1.5% agarose (Type-III agarose, Sigma-Aldrich) in ACSF, followed by a small coverslip. It is important to avoid using too much agarose, as it interferes with imaging. The coverslip can be placed either on top of the bone, or between bone and dura. Second, the coverslip is held in place by small clamps attached to the imaging well (Fig. 1), which should be set up to provide gentle pressure on the brain. Care needs to be taken that neither coverslip nor clamps block the objective's access to the brain.

The goal of the mechanical stabilization is to eliminate vertical movements. Remaining horizontal movements can then be corrected offline after data collection. A successful strategy for offline motion correction has been to use a two-stage process described in detail in Nauhaus et al. (2012a): First, slow drifts are corrected by computing the average image in every trial and aligning these average images to the average of the first trial using two-dimensional (2D) cross-correlation. Second, fast movements are corrected using an optic flow-based method. Other approaches are also possible and have been described in the literature (Greenberg and Kerr, 2009).

Offline motion correction is feasible only if data are acquired in raster scan format. In this acquisition mode, the laser beam is systematically swept over a 2D region. As a consequence, the collected data consist of a series of frames that show cell bodies and other structures, and horizontal displacements can be corrected by spatial transformations of the collected frames. Other acquisition modes increase acquisition speed by no longer sampling the entire 2D region. In random access scanning, for example, the laser beam “jumps” from one preselected point in the imaging region to the next (Reddy et al., 2008; Grewe et al., 2010). Because no data are recorded outside of the preselected points, data collected in this way cannot be corrected offline. Thus, these acquisition modes place more stringent requirements on brain stability.

### Data Analysis

The acquisition system of the two-photon microscope records raw fluorescence time courses  $F(t)$  for every pixel. Usually, raw fluorescence time courses are first transformed into  $\Delta F(t) = (F(t) - F_0)/F_0$ , where  $F_0$  is

the average fluorescence during some baseline period, e.g., a time period preceding stimulus onset. In a second step,  $\Delta F(t)$  is then averaged across all pixels falling within a neuron. Any further analyses are then based on the  $\Delta F(t)$  time courses for every cell. In these analyses, it is important to take into account how the measured changes in OGB fluorescence relate to the underlying changes in neural firing rates. The spike-to-fluorescence transfer function of OGB can be modeled as a linear–nonlinear cascade (Nauhaus et al., 2012b; Fig. 4): Each spike causes a transient influx in calcium, whose time course is characterized by a sharp rise followed by a slow exponential decay with a time constant of  $\sim 0.5$ – $1$  s (Helmchen et al., 1996; Kerr et al., 2005; Sasaki et al., 2008; Smith and Häusser, 2010; Chen et al., 2013). This signal is then transformed into the observed fluorescence signal via a saturating nonlinearity (Yasuda et al., 2004; Yaksi and Friedrich, 2006; Hendel et al., 2008).

The first important consequence of the spike-to-fluorescence transfer function of OGB is the temporal summation of action potentials caused by the slow exponential decay of the linear stage. As long as firing rates are low enough, individual spikes lead to clearly visible calcium transients, and spike times can be identified. However, from firing rates  $>5$  Hz on, the calcium transients of individual spikes can no longer be resolved because of the slow decay kinetics of the OGB signal (Sasaki et al., 2008). Thus, for firing rates  $>5$  Hz, spike times cannot be computed from the OGB data. In most areas of the monkey brain, firing rates will be well beyond this rate even under anesthesia.

The second important consequence of the spike-to-fluorescence transfer function of OGB is the distortion in signal caused by the saturating nonlinearity. We have demonstrated that this saturation can have a significant impact on measurements of tuning functions by clipping the fluorescence signal at higher firing rates (Nauhaus et al., 2012b). Distortions caused by the saturating nonlinearity were observed not only in ferret visual cortex, which has neurons with high firing rates, but also in mouse visual cortex, where firing rates are significantly lower. It is critical to keep these distortions in mind when interpreting OGB data. While some measurements (e.g., the tuning curve maximum) may not be affected by a monotonic nonlinearity, other measurements (e.g., tuning curve width) can be strongly distorted. As a consequence, differences among neuron groups or conditions with different firing rates could be artificially enhanced or diminished.

## Future Developments

So far, we have focused on how to perform two-photon calcium imaging in anesthetized animals using an injectable calcium dye. Although extremely valuable data can be collected under these conditions, it will be important for future research to be able to perform two-photon experiments in awake monkeys performing a task. A number of technical hurdles need to be overcome to make these experiments feasible. First, injectable calcium dyes will likely no longer be useful in an awake animal, in which repeated measurements will need to be carried out. As described earlier, injectable dyes can be used only in young animals, once per durotomy, and only in “fresh” durotomies. Instead, GECIs appear to be a better choice because they can be stably expressed in cells. The most recent generation of these indicators (GCaMP6s, 6m, and 6f) show great promise for future experiments because of their relatively fast response kinetics and good SNR (Chen et al., 2013).

GECIs require the injection of a virus into the brain to be expressed. Thus, going forward, we will need to identify which virus (e.g., different serotypes of AAV, lentivirus) will lead to sufficient expression in terms of spatial spread, expression density, as well as expression level within each cell. In addition, an appropriate promoter will need to be chosen. Another issue with respect to the use of GECIs is their impact on cell health. All GECIs are calcium buffers. Because calcium is important for many “housekeeping” functions in a cell (Berridge et al., 2000, 2003), excessive calcium buffering leads to cell death. How long cells remain viable after virus infection will depend on the particular indicator used and the rate at which it is expressed, which will in part depend on the virus chosen for expression. In the mouse, stable expression of GCaMP6 over several months has been demonstrated (Chen et al., 2013). Whether similar durations are possible in the monkey will need to be determined.

The switch from OGB to GECIs is one important issue that needs to be solved to be able to perform two-photon microscopy in awake monkeys. Other hurdles are the development of an imaging well, and the development of strategies to deal with brain movement. The largest engineering challenge with respect to the imaging well is the fact that most two-photon objectives are very large (diameters  $\leq 3$  cm) and need to be placed quite close to the brain (typical WD  $\sim 3$  mm). Thus, large implants are required. In addition, because monkey dura is opaque, it will need to be removed and replaced with an artificial dura. So far, one two-photon implant

has been developed (Stettler et al., 2006); implant designs similar to the ones used for optical imaging may be another possibility (Roe, 2007). Because of the necessary size of the well, and the removal of the dura, motion artifacts will be further exacerbated beyond the inevitable increase caused by using an awake animal. Thus, imaging wells likely will have to include provisions to stabilize the brain. Additionally, it may be necessary to develop ways to track brain movements online and to move the microscope in synchrony with the brain.

To summarize, two-photon microscopy is a promising addition to the toolkit available for research in the macaque monkey. Because of its unique capabilities—high resolution and high sampling density—it will open important novel avenues to study local circuit function. Two-photon calcium imaging in the anesthetized monkey is feasible today, but experiments in the awake monkey will require further technical developments.

## References

- Berridge M, Lipp P, Bootman M (2000) The versatility and universality of calcium signalling. *Nat Rev Mol Cell Biol* 1:11–21.
- Berridge MJ, Bootman MD, Roderick HL (2003) Calcium signalling: dynamics, homeostasis and remodelling. *Nat Rev Mol Cell Bio* 4:517–529.
- Chen T-W, Wardill TJ, Sun Y, Pulver SR, Renninger SL, Baohan A, Schreier ER, Kerr RA, Orger MB, Jayaraman V, Looger LL, Svoboda K, Kim DS (2013) Ultrasensitive fluorescent proteins for imaging neuronal activity. *Nature* 499:295–300.
- Denk W, Strickler J, Webb W (1990) Two-photon laser scanning fluorescence microscopy. *Science* 248:73–76.
- Eichhoff G, Busche M, Garaschuk O (2008) *In vivo* calcium imaging of the aging and diseased brain. *Eur J Nucl Med Mol Imaging* 35:S99–106.
- Garaschuk O, Milos R-I, Konnerth A (2006) Targeted bulk-loading of fluorescent indicators for two-photon brain imaging *in vivo*. *Nat Protoc* 1:380–386.
- Goeppert-Mayer M (1931) Über Elementarakte mit zwei Quantensprüngen. *Ann Phys* 401:273–294.
- Greenberg DS, Kerr JND (2009) Automated correction of fast motion artifacts for two-photon imaging of awake animals. *J Neurosci Methods* 176:1–15.

## NOTES

- Grewe BF, Langer D, Kasper H, Kampa BM, Helmchen F (2010) High-speed *in vivo* calcium imaging reveals neuronal network activity with near-millisecond precision. *Nat Methods* 7:399–405.
- Helmchen F, Denk W (2005) Deep tissue two-photon microscopy. *Nat Methods* 2:932–940.
- Helmchen F, Imoto K, Sakmann B (1996)  $\text{Ca}^{2+}$  buffering and action potential-evoked  $\text{Ca}^{2+}$  signaling in dendrites of pyramidal neurons. *Biophys J* 70:1069–1081.
- Hendel T, Mank M, Schnell B, Griesbeck O, Borst A, Reiff D (2008) Fluorescence changes of genetic calcium indicators and OGB-1 correlated with neural activity and calcium *in vivo* and *in vitro*. *J Neurosci* 28:7399–7411.
- Ikezoe K, Mori Y, Kitamura K, Tamura H, Fujita I (2013) Relationship between the local structure of orientation map and the strength of orientation tuning of neurons in monkey V1: a 2-photon calcium imaging study. *J Neurosci* 33:16818–16827.
- Kerr JND, Denk W (2008) Imaging *in vivo*: watching the brain in action. *Nat Rev Neurosci* 9:195–205.
- Kerr JN, Greenberg D, Helmchen F (2005) Imaging input and output of neocortical networks *in vivo*. *Proc Natl Acad Sci USA* 102:14063–14068.
- Kurth-Nelson ZL, Mishra A, Newman EA (2009) Spontaneous glial calcium waves in the retina develop over early adulthood. *J Neurosci* 29:11339–11346.
- Nauhaus I, Nielsen KJ, Disney AA, Callaway EM (2012a) Orthogonal micro-organization of orientation and spatial frequency in primate primary visual cortex. *Nat Neurosci* 15:1683–1690.
- Nauhaus I, Nielsen KJ, Callaway EM (2012b) Nonlinearity of two-photon  $\text{Ca}^{2+}$  imaging yields distorted measurements of tuning for V1 neuronal populations. *J Neurophysiol* 107:923–936.
- Nimmerjahn A, Kirchhoff F, Kerr JND, Helmchen F (2004) Sulforhodamine 101 as a specific marker of astroglia in the neocortex *in vivo*. *Nat Methods* 1:31–37.
- Reddy G, Kelleher K, Fink R, Saggau P (2008) Three-dimensional random access multiphoton microscopy for functional imaging of neuronal activity. *Nat Neurosci* 11:713–720.
- Roe AW (2007) Long-term optical imaging of intrinsic signals in anesthetized and awake monkeys. *Appl Opt* 46:1872–1880.
- Sasaki T, Takahashi N, Matsuki N, Ikegaya Y (2008) Fast and accurate detection of action potentials from somatic calcium fluctuations. *J Neurophysiol* 100:1668–1676.
- Sereno MI, Tootell RBH (2005) From monkeys to humans: what do we now know about brain homologies? *Curr Opin Neurobiol* 15:135–144.
- Smith SL, Häusser M (2010) Parallel processing of visual space by neighboring neurons in mouse visual cortex. *Nat Neurosci* 13:1144–1149.
- So P, Dong C, Masters B, Berland K (2000) Two-photon excitation fluorescence microscopy. *Annu Rev Biomed Eng* 2:399–429.
- Srienc AI, Kornfield TE, Mishra A, Burian MA, Newman EA (2012) Assessment of glial function in the *in vivo* retina. *Methods Mol Biol* 814:499–514.
- Stettler D, Yamahachi H, Li W, Denk W, Gilbert C (2006) Axons and synaptic boutons are highly dynamic in adult visual cortex. *Neuron* 49:877–887.
- Stosiek C, Garaschuk O, Holthoff K, Konnerth A (2003) *In vivo* two-photon calcium imaging of neuronal networks. *Proc Natl Acad Sci USA* 100:7319–7324.
- Svoboda K, Yasuda R (2006) Principles of two-photon excitation microscopy and its applications to neuroscience. *Neuron* 50:823–839.
- Tsien RY (1981) A non-disruptive technique for loading calcium buffers and indicators into cells. *Nature* 290:527–528.
- Yaksi E, Friedrich R (2006) Reconstruction of ring rate changes across neuronal populations by temporally deconvolved  $\text{Ca}^{2+}$  imaging. *Nat Methods* 3:377–383.
- Yasuda R, Nimchinsky EA, Scheuss V, Pologruto TA, Oertner TG, Sabatini BL, Svoboda K (2004) Imaging calcium concentration dynamics in small neuronal compartments. *Sci STKE* 2004:pl5.

# **Mesoscale Two-Photon Microscopy: Engineering a Wide Field of View with Cellular Resolution**

Jeffrey N. Stirman, PhD, and Spencer L. Smith, PhD

---

Neuroscience Center and Department of Cell Biology and Physiology  
University of North Carolina at Chapel Hill  
Chapel Hill, North Carolina



## Introduction

Information is widely distributed in neuronal networks. Patterns of activity across multiple brain areas act in concert to support sensory processing and behavior. Mapping this activity with cellular resolution can reveal principles of neural function but presents technical challenges.

Electrodes offer unsurpassed temporal resolution and can easily record from spatially separate populations. However, this approach is invasive, cannot be genetically targeted to record from specific cell types, and only sparsely samples local populations. By contrast, two-photon imaging of free calcium is less invasive, can be genetically targeted, and offers dense sampling of local populations. Two-photon imaging (Denk et al., 1990) is particularly suited for imaging activity in highly scattering neuropil, such as mammalian cortex, and the latest generation of genetically encoded calcium indicators (GECIs) can provide a high-fidelity optical readout of spiking (Chen et al., 2013).

However, conventional implementations of two-photon microscopy are often limited in their primary field of view (FOV) to approximately 700  $\mu\text{m}$ . Outside of this region, limiting apertures and aberrations decreases the effectiveness of two-photon excitation, leading to dim regions (“vignetting”) and reduced resolution. Brain regions can be distributed over areas larger than this FOV. For example, cortical

areas in mice are distributed over millimeters of cortex (Fig. 1). Thus, engineering improvements are needed to enable two-photon microscopy of FOVs large enough to encompass multiple brain regions. We refer to this wide FOV imaging as “mesoscale two-photon imaging.”

In this chapter, we discuss the main factors that limit the FOV of two-photon imaging and how to engineer optimized implementations to retain cellular resolution across a large FOV. We will also discuss imaging speed, which is crucial to ensure temporal resolution sufficient to map neural activity on timescales that are relevant for coding and behavior.

## Optomechanical Considerations

There are three main optomechanical determinants of the FOV for a laser scanning microscope: the scan angles (SAs) of the beam scanning engine (SE) (e.g., galvanometer mirrors); the magnification of the beam expansion relay (the ratio of the focal lengths of the scan lens and tube lens); and the focal length of the objective used (Fig. 2). A simple formula for the full FOV is:

$$\text{FOV} = 2 \times FL_{\text{OBJ}} \times \tan \left( \text{SA} \times \frac{FL_{\text{SL}}}{FL_{\text{TL}}} \right)$$

In this equation, SA is measured from the central optical axis, and is thus half of the full scan arc. Beam expansion is crucial because at the SE, smaller beam apertures can support increased scan speeds (higher temporal resolution), but large beam diameters are needed to overfill the back focal plane of the objective, which is critical for ensuring cellular resolution along the Z-axis (Zipfel et al., 2003; Kerr and Denk, 2008).

Next, we will discuss how the practical implementation of optics to support a large FOV involves careful engineering optimizations. Many of these essentially come down to accommodating high SAs using optical elements with short focal lengths (i.e., high numerical aperture [NA]) to ensure that the beam does not get clipped at any point in the system. In a representative two-photon microscope, the SA is  $\pm 3.5^\circ$ , the  $FL_{\text{SL}} = 50$  mm, the  $FL_{\text{TL}} = 200$  mm, and the  $FL_{\text{OBJ}} = 12.5$  mm (Nikon CFI75, 16 $\times$ , 0.8 NA). This would yield a total FOV of 380  $\mu\text{m}$ .

## Scanning system

A conventional scanning system consists of two galvanometer mirrors placed in proximity to one another, on orthogonal axes (to scan in X and Y). The deflection of the first mirror will cause displacement of the beam from the center of the second mirror. This

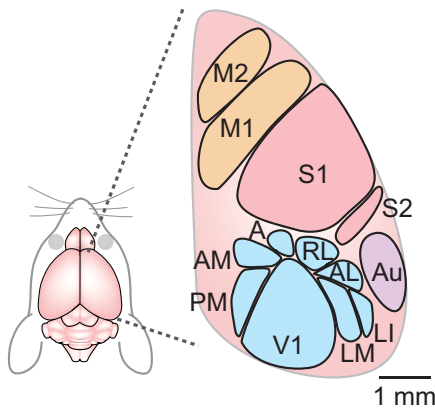


**Figure 1.** Imaging multiple cortical areas in a mouse requires an FOV that spans  $>1$  mm (scale bar). Schematic layout of a selection of cortical areas in the mouse. Primary visual cortex (V1, shaded blue) and higher visual areas (A, anterior; AL, anterolateral; AM, anteromedial; LI, laterointermediate; LM, lateromedial; PM, posteromedial; and RL, rostromedial, all shaded blue); auditory cortex (Au, shaded violet); primary and secondary sensory cortex (S1, S2, shaded pink); and primary and secondary motor cortex (M1, M2, shaded orange). Many cortical areas are  $>0.5$  mm wide, and thus a FOV  $>1$  mm wide is required to simultaneously image neurons in multiple cortical areas beyond immediate boundary regions.

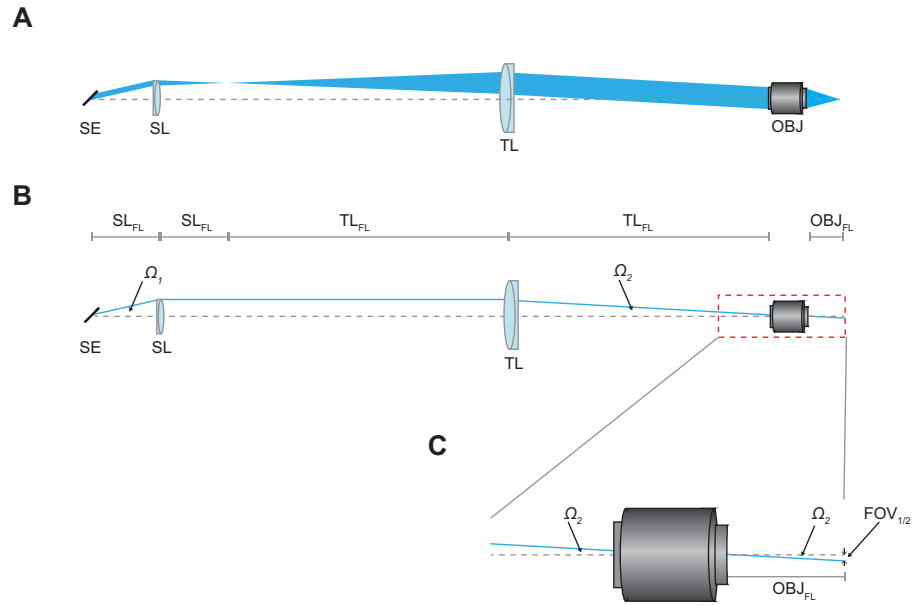


**Figure 2.** Basic optical layout for beam magnification after SE. **A**, After the SE, the deflected beam passes through the scan lens (SL) and then the tube lens (TL). This relay expands the beam and overfills the back aperture of the objective (OBJ). **B**, The distances between optics are configured in a 4f system. The final FOV is determined by the scanning angle (SA;  $\Omega_2$ ), which is determined by the SE SA ( $\Omega_1$ ), the ratio of the focal lengths of the SL and TL (this magnifies the beam and decreases the SA by reciprocal factors), and the focal length of the OBJ.

deflection is referred to as “beam walk.” At low SAs (and when the  $FL_{SL} \gg$  the distance between the two mirrors), this can be negligible (Tsai and Kleinfeld, 2009). However, at the relatively large SAs necessary for wide FOV imaging, beam walk can lead to a few millimeters of beam displacement on the second mirror, which can lead to beam clipping on either the scan lens, tube lens, or at the back focal plane of the objective. Any of these distortions would lead to vignetting and a reduction in the usable FOV. To combat this, an afocal relay can be placed between the X and Y scanning mirrors (Fig. 3). The afocal relay can be refractive (Kim et al., 1999; Vojnovic and Tullis, 2011) or reflective (Sharafutdinova et al., 2010a). In either case, high NA optics must be used to accept large SAs.

### Scan lens

To increase the FOV, relatively high SAs are used. The scan lens must have a small enough  $f$ -number (i.e., sufficiently high NA) to accept these deflections. For  $SA = 10^\circ$ , a scan lens of  $f$ -number  $\sim 2$  (NA  $\sim 0.25$ ) would be required. For a 1" diameter lens system, this translates to an effective focal length of 50 mm, to permit a 6 mm diameter beam to be scanned at  $\pm 10^\circ$ .

### Beam expansion

The ratio of the focal lengths of the scan lens and the tube lens determine the beam expansion ratio (beam magnification =  $FL_{TL}/FL_{SL}$ ). This expansion

is needed to completely fill the back aperture of the objective; therefore, decreasing the beam expansion to increase the final entrance beam angle is not always practical. Once the scan-lens focal length is chosen, it will determine the focal length of the tube lens. For example, the back aperture on the widely used Nikon CFI75 16 $\times$ /0.8 NA objective is  $\sim 22$  mm. If the input beam is 6 mm (limited by the clear aperture of the scanning system), then a 4 $\times$  beam expansion would overfill the back aperture of the objective.

### Tube lens

Since the focal length of the scan lens and the beam expansion have been chosen, the focal length of the tube lens has been determined: In this case, it is 200 mm. Because the beam is undergoing expansion, when it reaches the tube lens, if the tube lens is not sufficiently large, the beam will be clipped. The center of the beam is displaced by  $(50 \text{ mm}) * \tan(10^\circ) = \sim 9$  mm. At the point it reaches the tube lens, the radius of the beam is 12 mm, and thus the minimum radius of the tube lens must be  $9 \text{ mm} + 12 \text{ mm} = 21$  mm; otherwise, significant vignetting will occur, limiting the usable FOV. In this case, 2" optics for the tube lens are sufficient. Often optomechanical components are placed between the tube lens and the objective (e.g., a 45 $^\circ$  dichroic mirror to split excitation light and emitted fluorescence). All these elements must be large enough to prevent clipping of the beam

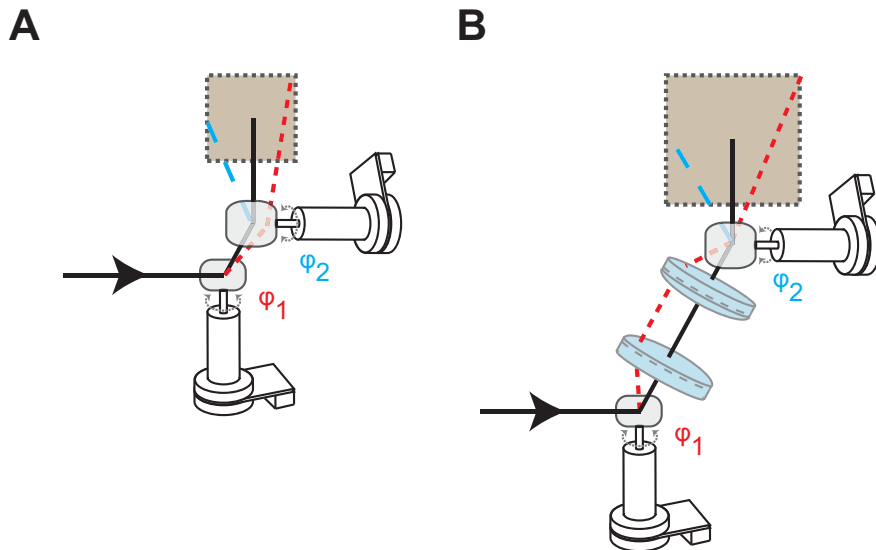


**Figure 3.** Beam walk. **A**, When scan mirrors are placed in proximity to one another, the deflection of the first mirror will cause displacement of the beam from the center of the second mirror. Called “beam walk,” this can be negligible when scanning at small angles. However, at large angles, this leads to severe beam clipping and vignetting (a restricted FOV). **B**, To combat beam walk and maintain signal quality over larger scan angles (for a larger FOV), an afocal beam relay between the two scan mirrors can be used. Here, a refractive relay is shown. Reflective relays, using off-axis parabolic mirrors, can also be used.

even at high SA. Some long-focal-length custom objectives and high NA microscope objectives have back apertures  $\sim 50$  mm in diameter—more than twice what we considered in the present analysis. Although theoretically these objectives can provide a wide FOV, implementing them in a two-photon microscope (e.g., overfilling their back apertures) can present significant challenges.

### Wavefront Considerations

In two-photon excitation, the scanning focal spot must be of high optical quality and possess sufficient photon density to achieve two-photon excitation. Although high NA objectives are important, they are not always the limiting parameter when imaging over a large FOV. Optical aberrations, which can be introduced anywhere in the optical system, can degrade the wavefront and decrease the efficiency of two-photon excitation of a microscope. When scanning at small angles, aberrations can be minimal. However, aberrations become increasingly important at high scan angles, and these can ultimately limit the FOV. An extensive optimization study of scan and tube lens designs found that when using a single achromat for the scan lens, only approximately the central third of the theoretical FOV was diffraction-limited (Negrean and Mansvelder, 2014). This limitation is mainly the result of the significant astigmatism introduced at large off-axis angles. The usable fraction of FOV is increased with compound lens design (e.g., a

Plossl lens) or completely custom scan lens systems. This study also showed that single achromats used for tube lenses can limit performance, whereas custom lens designs can again increase performance across the entire FOV (Negrean and Mansvelder, 2014).

The aberration-induced wavefront distortions must also be considered when using a relay between the scanning mirrors. Optimized relay lenses can be designed similarly to the scan lenses. The relay lenses must match the NA of the scan lens, or they will limit the usable angles. Another option is to use off-axis parabolic mirrors (Sharafutdinova et al., 2010a; Negrean and Mansvelder, 2014). Parabolic mirror-based relays can offer diffraction-limited performance across large SAs, and potentially provide lower wavefront errors compared with refractive designs or spherical mirror relays (Sharafutdinova et al., 2009, 2010a, b).

Once careful optical design has minimized most aberrations, adaptive optics can further improve performance by correcting residual aberrations, including those introduced by the preparation itself. *In vivo*, wavefronts cannot typically be measured directly; thus, various methods have been developed to determine patterns that can cancel aberrations during *in vivo* imaging and increase fluorescence yield (Debarre et al., 2009; Aviles-Espinosa et al., 2011; Ji et al., 2012).

## Imaging Speed

As the FOV increases in area, if the number of pixels per neuron is preserved, the quantity of effective pixels per image is greatly increased. For example,  $\geq 100$  neurons can be imaged in a  $250 \times 250 \mu\text{m}$  square FOV, and raster scanning requires at least  $128 \times 128$  pixels ( $2^{14}$  pixels). Thus, for a  $3 \text{ mm}^2$  image,  $\sim 4800$  neurons can be imaged (though in practice, vasculature obscures a significant fraction of these), and  $> 2^{19}$  pixels can appear in a raster scan. For conventional galvanometer scanning, the scan speed is inertia-limited to  $\sim 1 \text{ kHz}$  (1 ms/line). Since  $\sim 2^8$  lines/frame are needed for a small region, this ultimately leads to a frame rate limit of  $\sim 10$ – $15$  frames per second for a  $250 \mu\text{m}$  wide FOV. This rate limit can be sufficient

for many experiments, as the dynamics for current GECIs are  $> 100 \text{ ms}$ , and even studies of spike-count correlations often use counting windows of  $0.1$ – $1.0 \text{ s}$ . However, some experiments require (or can be enhanced by) higher scanning speeds. Moreover, scanning entire large FOVs can take several seconds per frame. Here we briefly survey some alternative approaches that can offer higher scan speeds.

## Resonant scanning

Using a resonant scanner as the fast axis and a conventional galvanometer scanner as the slow axis, scan speeds of  $\geq 30$  frames/s are possible (Nguyen et al., 2001). The resonant axis oscillates at a fixed frequency ( $4$ – $12 \text{ kHz}$ ), and thus the line scanning rate is fixed. Because the resonant scanner scans a sinusoidal path, resulting images need to be corrected for the nonlinearity. This correction can be done either by clipping the edges of the image (leaving the more linear central region) or by applying a nonlinear corrective procedure to the image (Haji-Saeed et al., 2007). Overall, resonant scanning systems can provide ample SAs,  $> 20^\circ$ , and thus are a good fit for wide FOV imaging.

## Acousto-optical deflectors

An alternative method for achieving very high scan speeds employs acousto-optical deflectors (AODs; Fig. 4C). An AOD is a crystal whose angle of diffraction can be varied using an applied acoustic wave (typically in the radiofrequency range). An AOD can raster scan a laser beam at rates  $> 100 \text{ Hz}$ . Using AODs, fully three-dimensional (3D) noninertial scanning can be used to map neural activity (Duemani Reddy et al., 2008; Kirkby et al., 2010). The two drawbacks to AODs are added dispersion (which degrades two-photon excitation) and relatively small maximum SAs, typically  $< 4^\circ$ . While the former problem has been mostly solved, the latter issue remains, and demonstrated FOVs have been only  $\sim 700 \mu\text{m}$  across (Katona et al., 2012). Custom-designed AODs may offer increased SAs.

## Arbitrary line scanning

When raster scanning, much of the FOV does not contain active neurons, and thus most of the pixels do not contain information that will be used by the experimenter. Thus, to increase the scan rate, one can utilize an arbitrary line scan (Fig. 4D). This can be supported by either conventional galvanometer scanners or AODs. In this method, a raster image is first acquired to obtain the position of all the cells of interest. Next, a scan path is generated in which the laser is directed to pass over each cell of interest. These scans can be optimized for speed and repeatability (Cotton et al., 2013).

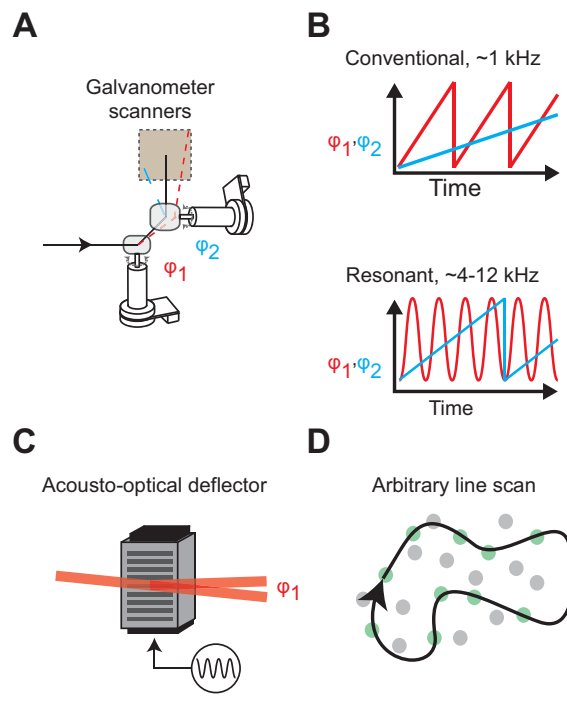


**Figure 4.** Beam SE technology. **A**, The most common SE is made from two galvanometer mirrors positioned along orthogonal axes. Scanning along one angle,  $\phi_1$ , translates the beam along the X-axis, and scanning along the other angle,  $\phi_2$ , translates the beam along the Y-axis. **B**, The basic driving waveform for dual galvanometer scanning is either a triangle or sawtooth (red) for the fast axis (typically the X-axis); the slower axis (Y-axis) is scanned using a sawtooth waveform (blue). When using a resonant scanner for the fast axis, the resulting scan is sinusoidal (red) at the fixed frequency of the resonant scanner. The slow axis is again scanned using a sawtooth waveform (blue). **C**, Another SE technology comprises AODs. These can be used in place of a galvanometer scanner for the fast axis, or multiple AODs can be used for 2D or 3D scanning. **D**, A faster alternative to raster scanning is arbitrary line scanning. Using either dual conventional galvanometers or AODs, a relatively short scan path can be defined that passes through cells of interest. This path can be retraced  $10$ – $100\times$  faster than a conventional raster scan of the same area, thereby increasing temporal resolution.

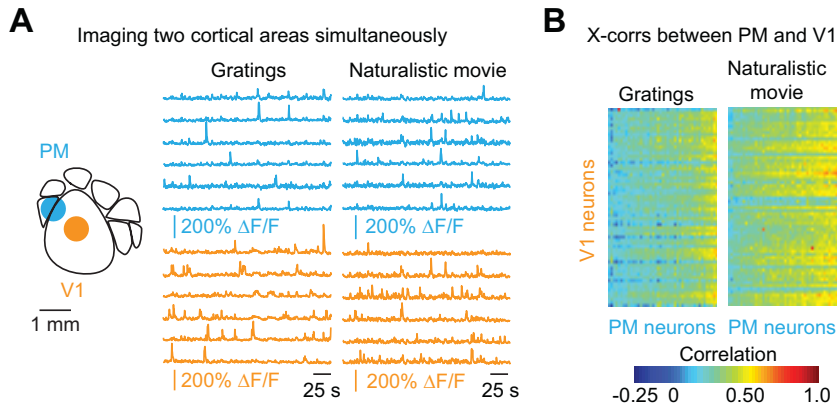


**Figure 5.** A solution for wide FOV imaging. **A**, Using a microscope with dual multiplexed beams and a wide FOV, cellular-level neural activity in two cortical areas (primary visual cortex and posteromedial [V1 and PM]) was imaged simultaneously. Signals for six neurons in each cortical area are shown. Scale bar, 1 mm. **B**, After deconvolving the fluorescence signals to obtain inferred spike rates, cross-correlations (X-corrs) were computed. X-corrs were higher during presentation of the naturalistic movie than during the drifting gratings. (The columns were ordered from low- to high-average correlation for presentation clarity.)

### Multiplexed beam scanning

Any of the above methods can be combined for multiplexed beam scanning. In this approach, pulses from multiple beams are interleaved. Each beam scans a separate area, and fluorescence is collected using a single objective and focused onto a high-bandwidth detector. Synchronization pulses are used to determine which beam caused each fluorescence event. Because each beam can scan a separate area, the imaging speed scales up by a multiple of the number of beams used (Amir et al., 2007; Cheng et al., 2011).

### Alternative Approaches

There are completely different approaches for imaging activity in multiple brain regions as well. For example, one could use two different microscopes. In this approach, the main challenge would be to place two objectives near one another, along with the rest of the optical pathways. However, with flexible positioning microscopes and low-profile objectives, it should be achievable, at a cost of increased complexity and likely limits on how close two imaged areas can be. Another simple solution would be to rapidly reposition the sample or the microscope. Movements of  $<1$  mm can be achieved with a motorized stage in  $<0.5$  s. Although this approach can be relatively simple to implement, it would suffer from severely limited maximal frame rates and low duty cycles (fraction of time spent imaging) owing to the movement time.

### Our Solution

We have recently developed a two-photon microscope that can scan a wide FOV with cellular resolution. We utilized highly corrected, low  $f$ -number optics

throughout the optical pathway to enable large FOV imaging: 1.4 mm with the Nikon CFI75  $16 \times 0.8$  NA objective, and 3.5 mm with a custom-built objective. Because conventional raster scanning over the entire FOV area ( $>9$  mm<sup>2</sup>) can take 1–10 s per frame, we developed a version of beam multiplexing with dynamic beam-steering mirrors to support simultaneous scanning of two regions of interest (ROIs) anywhere within the overall FOV (Fig. 5). This method enables smaller ROIs to be scanned at  $\sim 5$ –30 frames/s yet still preserves the ability to have these regions widely separated within or across different cortical areas.

### Conclusion

The FOV of two-photon imaging can be expanded to the mesoscale without sacrificing cellular resolution by minimizing optical aberrations and designing optomechanical systems that avoid limiting apertures. This technology will enable new kinds of experiments, in which dense samples of spatially separate populations of neurons are imaged nearly simultaneously. As a result, we will begin to map the distributed neural activity that underlies sensory processing and behavior in extended neural circuitry.

## NOTES

## References

- Amir W, Carriles R, Hoover EE, Planchon TA, Durfee CG, Squier JA (2007) Simultaneous imaging of multiple focal planes using a two-photon scanning microscope. *Opt Lett* 32:1731–1733.
- Aviles-Espinosa R, Andilla J, Porcar-Guezenec R, Olarte OE, Nieto M, Levecq X, Artigas D, Loza-Alvarez P (2011) Measurement and correction of *in vivo* sample aberrations employing a nonlinear guide-star in two-photon excited fluorescence microscopy. *Biomed Opt Express* 2:3135–3149.
- Chen TW, Wardill TJ, Sun Y, Pulver SR, Renninger SL, Baohan A, Schreiter ER, Kerr RA, Orger MB, Jayaraman V, Looger LL, Svoboda K, Kim DS (2013) Ultrasensitive fluorescent proteins for imaging neuronal activity. *Nature* 499:295–300.
- Cheng A, Goncalves JT, Golshani P, Arisaka K, Portera-Cailliau C (2011) Simultaneous two-photon calcium imaging at different depths with spatiotemporal multiplexing. *Nat Methods* 8:139–142.
- Cotton RJ, Froudarakis E, Storer P, Saggau P, Tolias AS (2013) Three-dimensional mapping of microcircuit correlation structure. *Front Neural Circuits* 7:151.
- Debarre D, Botcherby EJ, Watanabe T, Srinivas S, Booth MJ, Wilson T (2009) Image-based adaptive optics for two-photon microscopy. *Opt Lett* 34:2495–2497.
- Denk W, Strickler JH, Webb WW (1990) Two-photon laser scanning fluorescence microscopy. *Science* 248:73–76.
- Duemani Reddy G, Kelleher K, Fink R, Saggau P (2008) Three-dimensional random access multiphoton microscopy for functional imaging of neuronal activity. *Nat Neurosci* 11:713–720.
- Haji-Saeed B, Khoury J, Woods CL, Pyburn D, Sengupta SK, Kierstead J (2007) Mapping approach for image correction and processing for bidirectional resonant scanners. *Opt Eng* 46:027007.
- Ji N, Sato TR, Betzig E (2012) Characterization and adaptive optical correction of aberrations during *in vivo* imaging in the mouse cortex. *Proc Natl Acad Sci USA* 109:22–27.
- Katona G, Szalay G, Maak P, Kaszas A, Veress M, Hillier D, Chiovini B, Vizi ES, Roska B, Rózsa B (2012) Fast two-photon *in vivo* imaging with three-dimensional random-access scanning in large tissue volumes. *Nat Methods* 9:201–208.
- Kerr JN, Denk W (2008) Imaging *in vivo*: watching the brain in action. *Nat Rev Neurosci* 9:195–205.
- Kim KH, Buehler C, So PT (1999) High-speed, two-photon scanning microscope. *Appl Opt* 38:6004–6009.
- Kirkby PA, Srinivas Nadella KM, Silver RA (2010) A compact Acousto-Optic Lens for 2D and 3D femtosecond based 2-photon microscopy. *Opt Exp* 18:13721–13745.
- Negrean A, Mansvelder HD (2014) Optimal lens design and use in laser-scanning microscopy. *Biomed Opt Exp* 5:1588–1609.
- Nguyen QT, Callamaras N, Hsieh C, Parker I (2001) Construction of a two-photon microscope for video-rate Ca(2+) imaging. *Cell Calcium* 30:383–393.
- Sharafutdinova G, Holdsworth J, van Helden D (2009) Improved field scanner incorporating parabolic optics. Part 1: Simulation. *Appl Opt* 48:4389–4396.
- Sharafutdinova G, Holdsworth J, van Helden D (2010a) Improved field scanner incorporating parabolic optics. Part 2: Experimental verification and potential for volume scanning. *Appl Opt* 49:5517–5527.
- Sharafutdinova G, Holdsworth J, van Helden D (2010b) Calculated two-photon fluorescence correction factors for reflective scan engines. *Appl Opt* 49:1472–1479.
- Tsai PS, Kleinfeld D (2009) *In vivo* two-photon laser scanning microscopy with concurrent plasma-mediated ablation. In: *Methods for in vivo optical imaging*, Vol 3 (Frostig R, ed.), pp. 59–115. Boca Raton, FL: CRC Press.
- Vojnovic B, Tullis ID (2011) Optical laser beam scanner lens relay system. © Gray Institute, Department of Oncology, University of Oxford. <http://goo.gl/IqZa1W>.
- Zipfel WR, Williams RM, Webb WW (2003) Nonlinear magic: multiphoton microscopy in the biosciences. *Nat Biotech* 21:1369–1377.

# **Acousto-optical Scanning–Based High-Speed 3D Two-Photon Imaging *in Vivo***

Balázs Rózsa, MD, PhD, Gergely Szalay, and Gergely Katona

---

Institute of Experimental Medicine of the  
Hungarian Academy of Sciences  
Budapest, Hungary



## Rationale for Selecting Acousto-optical Scanning for *in Vivo* Network Measurement in Three Dimensions

Several novel technologies have been developed for the three-dimensional (3D) readout of fast populations and dendritic activities. These include liquid lenses (Grewe et al., 2011), holographic scanning (Nikolenko et al., 2008), Roller Coaster Scanning (Katona et al., 2011), piezo scanning with sinusoidal resonance (Gobel et al., 2007), deformable mirrors, temporal and spatial multiplexing (Cheng et al., 2011), axicon or planar illumination-based imaging (Holekamp et al., 2008), fast  $z$ -scanning based on an axially moving mirror (Botcherby et al., 2012), simultaneous multiview light-sheet microscopy (Tomer et al., 2012), and optical fiber acousto-optical deflector (AOD)-based 3D scanning (Rózsa et al., 2007). However, only acousto-optical scanning can increase the product of the measurement speed and the signal collection efficiency by several orders of magnitude, as compared with classical raster scanning.

More quantitatively, random-access scanning increases measurement speed and signal collection efficiency in the following way:

$$\frac{(\text{measurement speed}) * (\text{signal collection})}{(\text{total image volume})} \cong \frac{(\text{volume covered by the scanning points})}{(\text{total image volume})}$$

where “signal collection” is defined as the amount of the detected fluorescent photons in a given time interval from a given spatial location, and the “volume covered by the scanning points” is the convolution of the point spread function (PSF) and the preselected scanning points. In a typical *in vivo* measurement, when we consider using a  $450 \times 450 \times 650 \mu\text{m}^3$  scanning volume with a  $0.47\text{--}1.9 \mu\text{m}$  and  $2.49\text{--}7.9 \mu\text{m}$  axial resolution (Katona et al., 2012), and simultaneously measure approximately 100 locations, random access scanning will provide a 2,106,000–46,534-fold, on average an increase of six orders of magnitude, in the product of measurement speed and signal collection efficiency. According to the current state of the technology (which now provides an  $\sim 1 \text{mm}^3$  scanning volume with high-numerical-aperture [NA] objectives), this increase could be even larger: more than 1,000,000,000 per locations. No other available 3D method with high spatial resolution and deep penetration capability can provide a similar increase in the product of the measurement speed and the signal collection efficiency.

A further advantage of 3D acousto-optical microscope technology is that it is based on single-spot two-photon activation, which allows whole-field detection with high-quantum-efficiency photomultiplier tube (PMTs). Therefore, photons scattered from deep layers of the tissue can also be collected with high sensitivity, which is essential to realize imaging through the whole cortex. Moreover, the position of the PSF can be finely adjusted, with 50–100 nm precision (Katona et al., 2012), to any spatial coordinates during acousto-optical scanning. Therefore, there is no limitation in  $z$ -planes and coordinates, which enables a highly precise measurement of neuronal activity by eliminating neuropil contamination.

## Principles

The phrase “acousto-optic” refers to the field of optics that studies the interaction between sound and light waves. In imaging, it means especially the diffraction of a laser beam through ultrasonic grating. The acousto-optical effect is produced by the periodic change in the refractive index of the medium (usually tellurium dioxide), which results from the sound-wave-induced pressure fluctuation in the crystal. This grating diffracts the light beam just like normal optical grating.

## Acousto-optical deflection

AODs spatially control the optical beam using ultrasonic waves. During operation, the acoustic frequency is varied in a way that results in an acoustic-frequency-dependent diffraction of the laser beam. The change of the diffraction angle is given by the following formula:

$$\Delta\theta_d = \frac{\lambda}{v} \Delta f$$

where  $\lambda$  is the optical wavelength of the beam,  $v$  is the velocity of the acoustic wave, and  $\Delta f$  is the change of the sound frequency (Fig. 1).

In practice, AODs or acousto-optical modulators (AOMs) are used. AOMs modulate only the amplitude of the sound waves, whereas AODs are able to adjust both the amplitude and the frequency.

## Acousto-optical focusing

Besides deflection, AODs can be used for fast focal-plane shifting (Kaplan et al., 2001; Vucinic and Sejnowski, 2007; Katona et al., 2012; Cotton et al., 2013; Fernandez-Alfonso et al., 2014). If the optical aperture is filled with acoustic waves whose frequency increases as a function of time (chirped wave), different portions of the optical beam are deflected

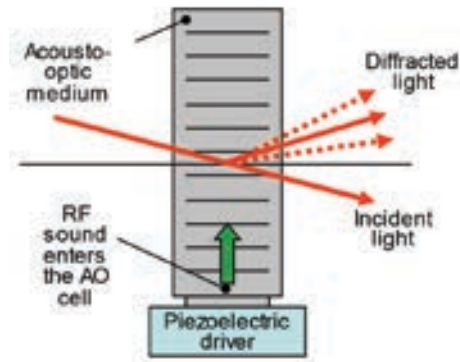


**Figure 1.** Operating principle of acousto-optical (AO) deflectors. RF, radiofrequency.

in different directions (Fig. 2); thus, a focusing or defocusing effect occurs, depending on the frequency slope (sweep rate) of the chirped acoustic wave.

The focal length of acousto-optical lens can be calculated from the sweep rate. The focal distance ( $F$ ) of the deflectors can be defined as follows:

$$F = \frac{v^2 T_{scan}}{2\lambda\Delta f}$$

where  $\lambda$  is the optical wavelength of the beam,  $v$  is the velocity of the acoustic wave,  $\Delta f$  is the change of the sound frequency, and  $T_{scan}$  is the modulation rate of the sound frequency (Kaplan et al., 2001).

To keep the focus stable, the frequency gradient should be preserved in the crystal. The frequency should therefore be continuously increased (or decreased) at the piezoelectric driver to preserve the focal distance. This will result in a lateral drift of the focal spot that can be easily compensated by a second AOD with a counterpropagating acousto-optical wave. The optical grid generated within the AOD is equivalent to a cylindrical lens. In 3D two-photon microscopy, it is necessary to scan points. Therefore, a combination of two perpendicularly oriented cylindrical lenses with the same focal distance is required. And, because both acousto-optical lenses ( $x$ ,  $y$ ) require drift compensation, 3D microscopes need at least four AO deflectors ( $x_1$ ,  $y_1$ ,  $x_2$ ,  $y_2$ ). The four AO deflectors can be optically coupled using “afocal projections” (telescopes with two lenses where the distance between the lenses is equal to the sum of each lens’s focal length) and air in different combinations. The largest scanning volume can be reached by grouping the deflectors into two functionally distinct groups ( $z$ -focusing and lateral scanning), which are coupled by one afocal projection (Katona et al., 2012).

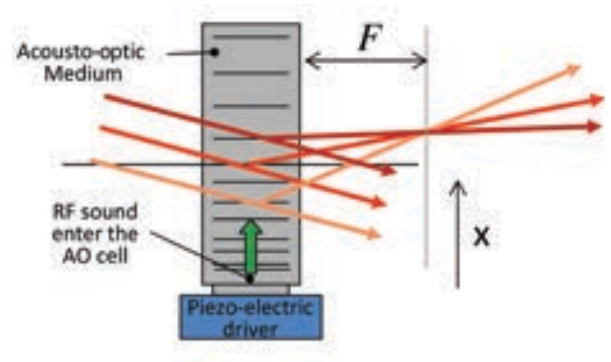


**Figure 2.** Acousto-optical (AO) focusing. RF, radiofrequency.

### Controlling 3D acousto-optical scanning

To focus the excitation beam to a given  $x, y, z$ -coordinate, the four AODs should be driven synchronously with varying frequency voltage signals. Because AODs have limited electrical bandwidths, the changing frequency can be maintained only for a limited time before the frequency has to be abruptly reset. This sudden change of frequency results in an improperly formed focal spot, and thus can be considered “dead time” (Fig. 3). The length of this period is defined by the time the acoustic wave travels through the aperture of the crystal, usually  $\sim 5\text{--}30\ \mu\text{s}$ .

The position and the movement of the focal point are determined by eight values. Four of them control the starting acoustic frequency on the four AOD drivers, while the other four define the frequency ramp speeds (chirping). All eight parameters are updated in every sweep cycle (typically  $33.6\ \mu\text{s}$  is used; the minimum is  $5\text{--}10\ \mu\text{s}$ ). The starting frequencies and the chirps together define the  $xyz$  position of the focal spot and its  $xy$  movement speed (drifting). During every sweep cycle, all PMT channels are sampled multiple times. The ratio of the dead time (offset time) to the measurement time (when the focal spot has already been formed and is ready for imaging) depends on the  $z$ -level and is optimal at the nominal focal plane of the objective.

In the simplest case, the goal is to attain a steady focal spot without lateral drifting (in random-access scanning mode). In this scanning mode, PMT data are averaged, and one value is created for each measurement cycle, corresponding to a single point in  $xyz$ . Thus, this mode enables random-access 3D point scanning, which is ideal for monitoring neuronal network activity. More complex measurement modes are possible when one lets the focal spot drift, such as during Multiple 3D Trajectory Scanning.

## The 3D Acousto-optical Microscope

### Realization of the optical pathway

In order to realize the optical pathway of a 3D microscope, one must create a 3D random-access laser scanning two-photon microscope that simultaneously satisfies two different needs in the largest possible scanning volume. The first need is to record activity across the dendritic tree of a single neuron at high spatial and temporal resolution in 3D in a central core ( $\sim 290 \times 290 \times 200 \mu\text{m}^3$ ) of the scanning volume and to do so in such a way that dendritic spines remain resolvable. The second need is to record activity in a more extensive volume (now  $>1100 \times 1100 \times 3000 \mu\text{m}^3$  in transparent samples) at high speed but at a lower resolution, in order to capture the activities of a large number of cell bodies in a neuronal population.

Following the arrangement suggested by the model, a large-aperture (15–17 mm) optical assembly was constructed (Figs. 4, 5). Here, a Ti:S laser with automated dispersion compensation provides the laser pulses. A Faraday isolator blocks the coherent backreflections. A four-prism sequence (Proctor and Wise, 1992) adds a large negative second- and third-order dispersion ( $-72,000 \text{ fs}^2$  and  $-40,000 \text{ fs}^3$ ,

respectively) in order to precompensate for pulse broadening caused by the optical elements of the system (dispersion compensation unit; Fig. 5).

An automated beam stabilization unit (see Laser Beam Stabilization, below) is necessary to precisely stabilize the laser beam of the long optical pathway and to cancel out subtle thermal drift errors. The beam stabilization unit is built from position sensors (quadrant detectors) and motorized mirrors, wired in a feedback loop. The beam is then magnified by a beam expander to match the large apertures (15 mm) of the first pair of AODs. These AODs form two orthogonal electric cylinder lenses filled with continuously changing frequency (“chirped”) acoustic waves (Kaplan et al., 2001), which are used for  $z$ -focusing (AO  $z$ -focusing unit).

Next, laser beams from the  $x$  and  $y$  cylindrical lenses are projected onto the  $x$  and  $y$  AO deflectors (17 mm apertures) of the 2D scanning unit, respectively, by telecentric projection. This 2D-AO scanning unit performs lateral scanning and compensates for the lateral drift of the focal spot generated by the cylindrical lenses during  $z$ -focusing, i.e., drift compensation (Kaplan et al., 2001). The angular

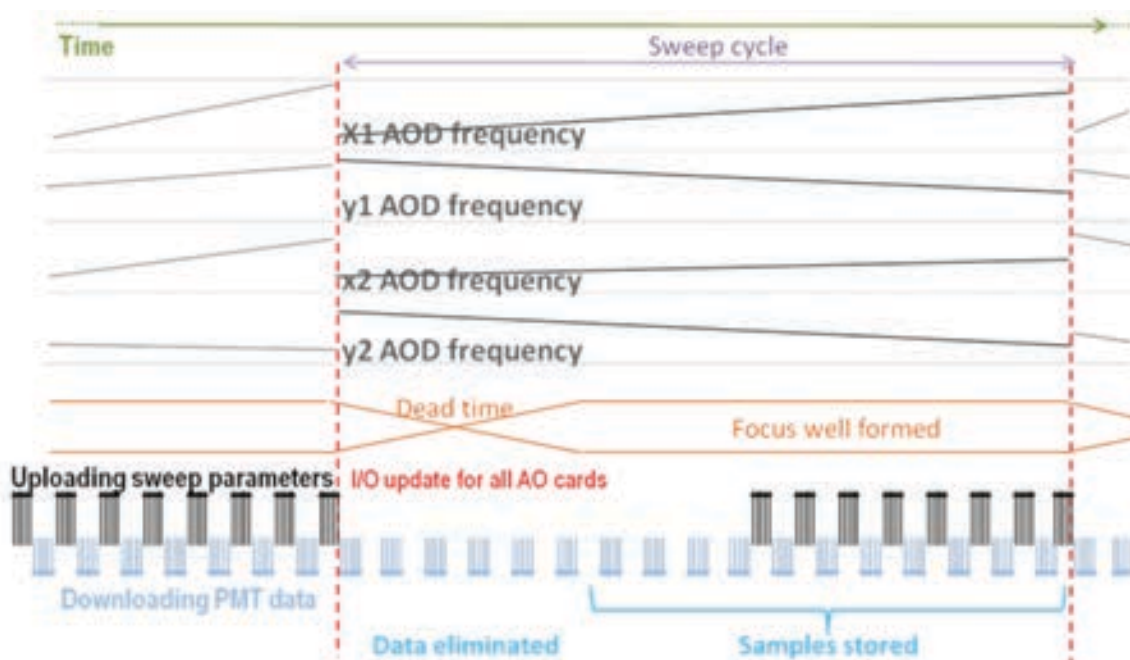


**Figure 3.** Driving functions and timing of operation of the four-deflector sequence. Top, The four upper traces show the frequency modulation of the sine wave as a function of time for the four AO deflectors ( $x_1$ ,  $y_1$ ,  $x_2$ ,  $y_2$ ) within 1.5 sweep cycles. This results in “dead” times and periods when focus is well formed (orange). Bottom, PMT data are continuously collected and transferred to the computer; however, PMT data collected during the dead time period are eliminated during the acquisition. Red dashed lines, synchronous frequency reset of all driver functions.

## NOTES

dispersion compensation unit optically links the 2D-AO scanning unit with the objective. Modeling helped us design and manufacture a custom lens made of high-dispersion glass with aspheric and conic surfaces which, combined with a telecentric projection of the AO scanner unit to the objective's back aperture, diminishes the angular dispersion introduced by the AO devices at off-axis positions ( $x, y \neq 0$ ). Then, the 3D scanning system is coupled to a 2D two-photon microscope in which fluorescent signals are collected by PMTs fixed directly onto the objective arm for high photon-collection efficiency (Fig. 5). In contrast to previous AO microscope designs, we have also taken advantage of the active optical elements to dynamically compensate for optical errors (e.g., astigmatism, field curvature, angular dispersion, chromatic aberration) that increased spatial resolution especially during AO  $z$ -focusing (at  $z \neq 0$  planes by a factor of  $\sim 2$ – $3$ ; Fig. 4).

We determined the optimal compensation parameters in advance for each point of the scanning volume and loaded them into the driver electronics accordingly. During this optimization process, we varied the parameters of the chirped sine driver function at each of the four deflectors in order to maximize the fluorescence intensity and the sharpness of the fluorescent beads used during this calibration. Spatial resolution in the whole scanning volume was also increased by the large optical apertures used

throughout the system, and  $\sim 20\%$  of this increase resulted solely from the use of large AOD apertures (Fig. 4). In contrast to the dominantly  $z$ -focusing-dependent effect of dynamic error compensation, the angular dispersion compensation unit decreased the PSF in off-axis positions when compared with a simple two-lens telecentric projection (Fig. 4b). These factors that decrease the PSF inherently increase the lateral field of view (Fig. 4a).

One difference between the system described here and previous designs is that the AODs form functionally and physically different groups.  $Z$ -focusing is carried out by the first AO pair, whereas lateral scanning is performed entirely by the second pair (2D-AO scanning unit). This arrangement increased the diameter of the lateral scanning range by a factor of  $\sim 2.7$  (Fig. 4a). Furthermore, not only electronic driver function but also deflector geometry,  $\text{TeO}_2$  crystal orientation, and bandwidth differed between deflectors of the  $z$ -focusing and the 2D-AO scanning unit. Altogether, these factors increased the diameter of the lateral scanning range by  $\leq 720 \mu\text{m}$  using the Olympus  $20\times$  objective and  $>1100 \mu\text{m}$  using the Nikon  $16\times$  objective.

## Materials and methods

Figure 5 is a schematic block diagram of the microscope, which was realized according to detailed optical modeling (Katona et al., 2012). Laser pulses

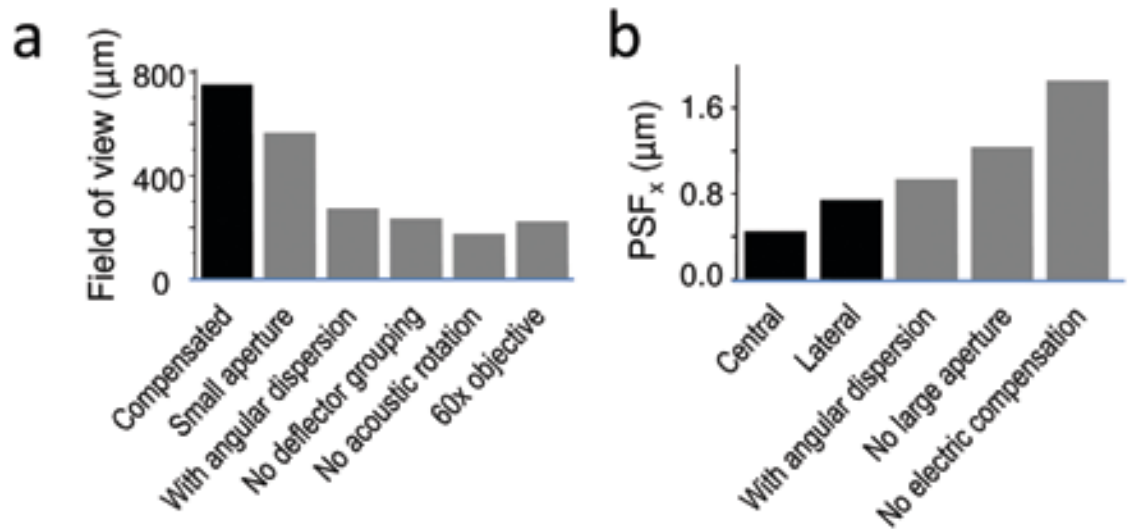


**Figure 4.** Characterization of the two-photon AO microscope setup. **a**, The maximal field of view (“compensated”) is shown when both deflector pairs were used for deflection (“no deflector grouping”) or when optically rotated deflectors (“no acoustic rotation”), small aperture objectives ( $60\times$ ), no angular dispersion compensation (“with angular dispersion”) or small aperture AODs were used (“small aperture”). **b**, The compensated PSF size along the  $x$ -axis ( $\text{PSF}_x$ ) (“central”) at  $(x, y, z) = (150, 150, 100) \mu\text{m}$  coordinates (“lateral”) or when no angular dispersion compensation (“with angular dispersion”), no electronic compensation (“no electric compensation”), or reduced AO apertures (“no large apertures”) were applied. Reprinted with permission from Katona et al. (2012), their Fig. 1b, c.

are provided by a Mai Tai DeepSee femtosecond laser (Spectra-Physics, Santa Clara, CA). The optimal wavelength range is 740–880 nm (but can also be extended  $\leq 1064$  nm). Pulse backreflection to the laser source is eliminated by a Faraday isolator (BB8-5I, Electro-Optics Technology, Traverse City, MI). Next, the beam position is stabilized using two motorized mirrors (m, Fig. 5) (Agilis Series, AG-M100N, Newport), which stabilize the position of the light transmitted by two backside custom-polished broadband mirrors (BB2-E03, Thorlabs, Newton, NJ) on the surface of two quadrant detectors (q, Fig. 5) (PDQ80A, Thorlabs). The positioning feedback loop (U12, LabJack Corporation, Lakewood, CO) is controlled by a program written in LabVIEW

(National Instruments). The beam is expanded by two achromatic lenses arranged in a Galilean telescope ( $f = -75$  mm, ACN254-075-B, Thorlabs;  $f = 200$  mm, NT47319, Edmund Optics; distance = 125.62 mm) to match the large apertures of the first pair of AODs (15 mm). Mirrors,  $\lambda/2$  wave plates and holders, are purchased from Thorlabs and Newport. AODs have been custom designed and manufactured at the Budapest University of Technology and Economics. Achromatic telecentric relay lenses were purchased from Edmund Optics ( $f_{TC} = 150$  mm, NT32-886). Achromatic scan and tube lenses were chosen from Edmund Optics ( $f = 250$  mm, NT45-180) and Olympus ( $f = 210$  mm), respectively. The AO-based 3D scanner system is attached to the top of a

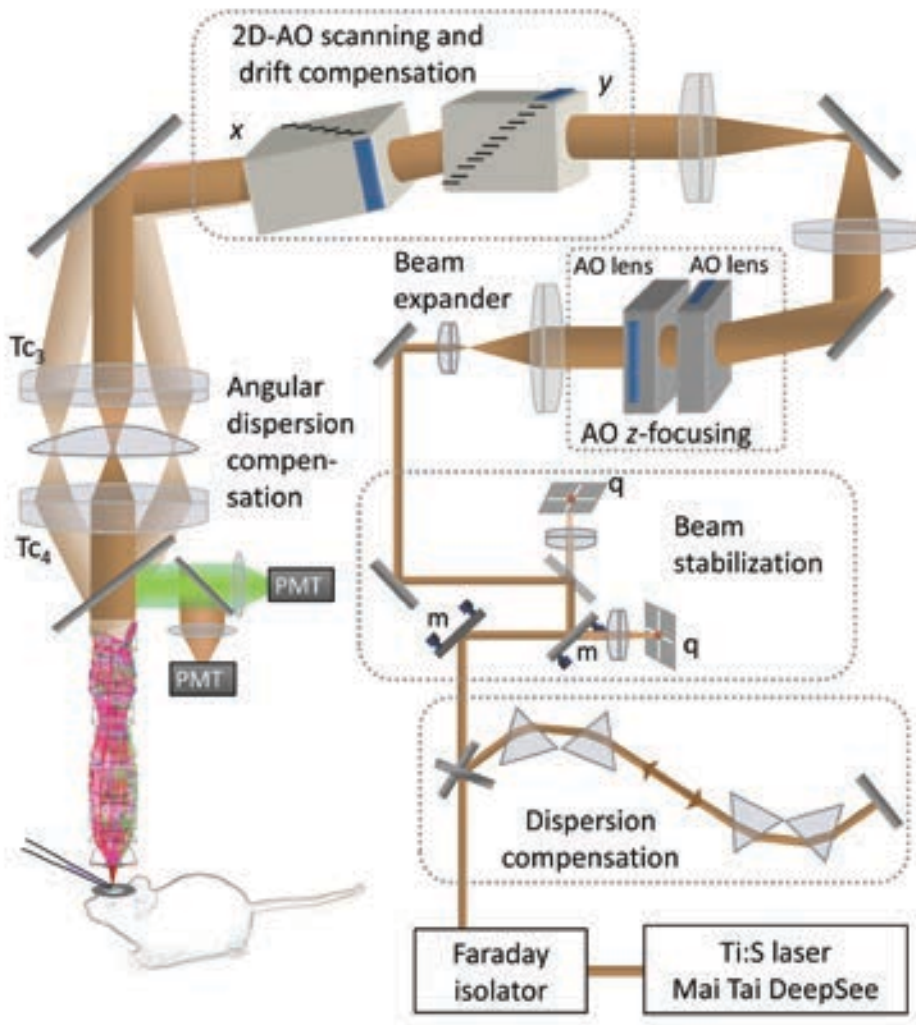


**Figure 5.** Design and characterization of the two-photon AO microscope setup. Material-dispersion compensation is adjusted using a four-prism compressor and a Ti:S laser. A Faraday isolator eliminates coherent backreflections, while a Ti:S laser with automated dispersion compensation provides the laser pulses. Motorized mirrors (m) stabilize the position of the beam light on the surface of two quadrant detectors (q) before the beam expander. Two AODs optimized for diffraction efficiency control the z-focusing of the beam (AO z-focusing). A 2D-AO scanner unit performs x–y scanning and drift compensation during z-scanning. A spherical field lens in the second telecentric lens system ( $Tc_{3,4}$ ) provides additional angular dispersion compensation. Reprinted with permission from Katona et al. (2012), their Fig. 1a.

## NOTES

galvanometer-based, upright two-photon microscope (Femto2D Alba, Femtonics, Budapest) using custom-designed rails. AO sweeps are generated by direct digital synthesizer chips (AD9910, 1 GSPS, 14-bit, Analog Devices, Norwood, MA) integrated into the modular electronics system of the microscope using FPGA elements (Xilinx).

Red and green fluorescence are separated by a dichroic filter (39 mm, 700dcxru, Chroma Technology, Bellows Falls, VT) and are collected by GaAsP PMTs custom-modified to efficiently collect scattered photons (PMT, H7422P-40-MOD, Hamamatsu Photonics, Hamamatsu City, Japan), fixed directly onto the objective arm (traveling detector system). In *in vitro* experiments, the forward-emitted fluorescence can also be collected by 2 inch aperture detectors positioned below the condenser lens (Femto2D Alba, Femtonics). Signals of the same wavelength

measured at the epifluorescent and transfluorescent positions are added. The large aperture objectives, XLUMPlanFI20×/0.95 (Olympus, 20×, NA = 0.95) and CFI75 LWD 16×W (Nikon, 16×, NA = 0.8), provide the largest scanning volume (Katona et al., 2012). The maximal output laser power in front of the objective is ~400 mW (at 875 nm).

### Laser beam stabilization

The role of the laser beam stabilization loop is to compensate for the thermal drift and small vibration of the laser resonator and optical elements. The system comprises several elements that are highly sensitive to the incidence angle. To compensate for the translation and angle deviation of the beam, a pair of two-axis piezo mirrors with two quadrant detectors act as a reference.

### Prism compressor

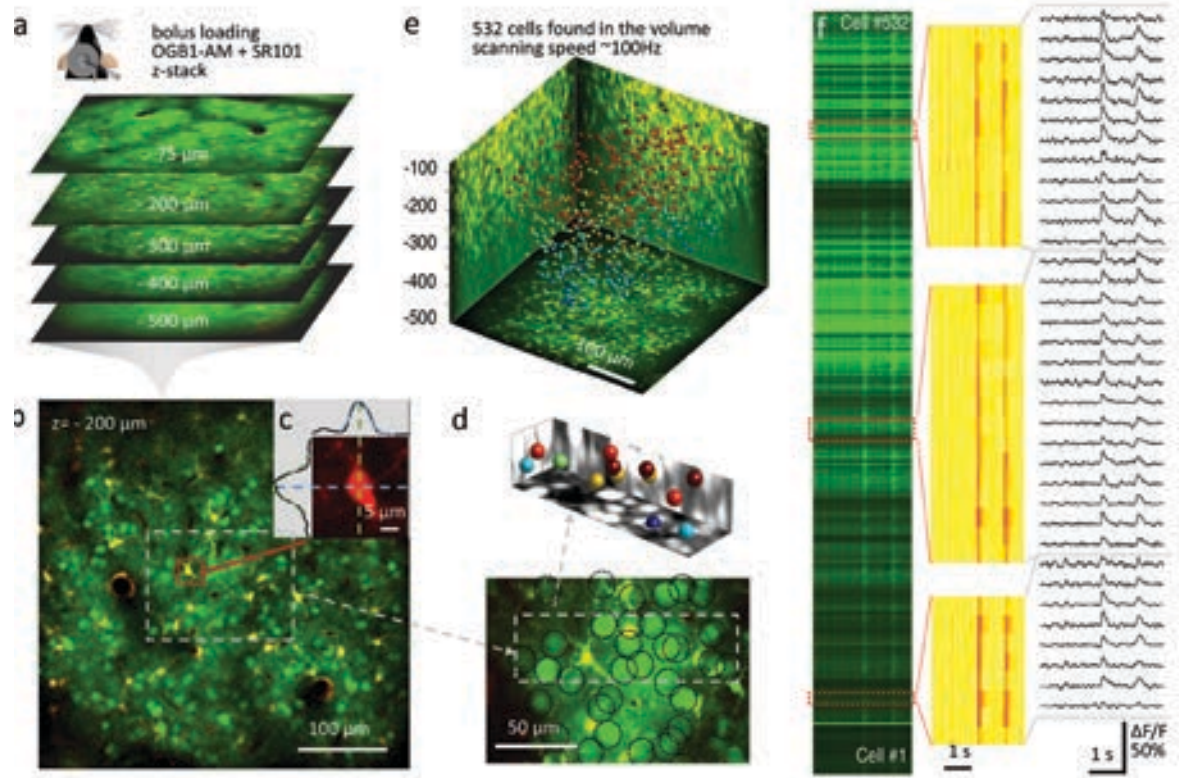


**Figure 6.** High-speed 3D calcium imaging of spontaneous neuronal network activity *in vivo*. **a**, Top, Sketch of *in vivo* experimental arrangement. Bottom, Staining by bolus loading (Oregon Green BAPTA [OGB]-1-AM and SR-101) in mouse primary visual cortex (V1). Five representative planes at different depths are imaged with 3D-AO scanning. Depths are measured relative to the pia. **b**, Example of an image plane at 200  $\mu\text{m}$  depth showing neurons (green) and glial cells (magenta and white). Scale bar, 100  $\mu\text{m}$ . **c**, Image and intensity profiles of a preselected bright glial cell used to establish the measurement coordinate system. Scale bar, 5  $\mu\text{m}$ . **d**, Bottom, 35  $\mu\text{m}$  z-projection of the region marked in **b**. Scale bar, 50  $\mu\text{m}$ . Top, Neuronal somata detected with the aid of an algorithm in a subvolume (shown with projections, neurons in white and glial cells in black). **e**, Maximal intensity side- and z-projections of the entire z-stack ( $400 \times 400 \times 500 \mu\text{m}^3$ ) with autodetected cell locations (spheres) color-coded in relation to depth. The set detection threshold yields 532 neurons. Scale bar, 100  $\mu\text{m}$ . **f**, Spontaneous neuronal network activity measured in the 532 cells in **e**. Left, example of a raw trace in which each line corresponds to a cell. Spatially normalized traces (middle) and corresponding  $\text{Ca}^{2+}$  transients (right). Calibration, 1 s. Reprinted with permission from Katona et al. (2012), their Fig. 4.

The material dispersion compensation problem is solved by a motorized prism compressor. The four-prism unit (Fig. 5) adds a large negative dispersion to precompensate the pulse broadening caused by the optical elements of the system. Total compensation depends on the given wavelength. Approximately  $72,000 \text{ fs}^2$  second-order group delay dispersion (GDD) and  $\sim 40,000 \text{ fs}^3$  third-order dispersion (TOD) compensation is required; the precise amount depends on the objective used and the central wavelength. We also added a two-pass, four-prism compressor (Proctor and Wise, 1992; Rózsa et al., 2007) that provides a fixed compensation amount at a given wavelength. A mechanically fixed compressor unit could be combined with the variable compensation provided by the DeepSee unit of the Mai Tai laser (Spectra-Physics) to confer dynamically adjustable dispersion compensation for an optimum fluorescence signal. Alternatively, motorizing the four-prism sequences would enable the omission of the DeepSee unit and thereby provide  $\sim 10\%$  higher infrared transmission.

## Experiments

AO scanning technology can be beneficial in biological experiments in which one would like to perform functional imaging in 3D from sparse regions of interest (ROIs) relatively far from each other. For example, it is beneficial when one would like to

follow the activity of multiple dendritic segments of a single neuron (Chiovini et al., 2014), to measure activity from large neuronal networks (Katona et al., 2012; Cotton et al., 2013; Fernandez-Alfonso et al., 2014), or to perform simultaneous measurements of somas and dendritic spines (Katona et al., 2012; Fernandez-Alfonso et al., 2014).

## Acousto-optical scanning methods

Multiple scanning modes have been developed for AO scanning that can also be used in different combinations as needed by the experimental protocol.

### Random-access point scanning

Random-access point scanning is one of the most convenient applications for imaging neuronal networks in 3D. In the first step, a reference  $z$ -stack image is acquired (Fig. 6a). In the second step, points can be preselected for fast 3D measurements (Figs. 6b–e). Once a region with well-stained cells is identified, one can select one or more reference structures (typically, a brightly red-fluorescing glial cell), scan it in 3D, and define the 3D origin [(0, 0, 0) coordinate] of the recording as the center of this glial cell (Fig. 6). In order to compensate for tissue drift, one needs to rescan the “origin-glia” cell regularly during an experiment and move it back into the original position (0,0,0) by moving the microscope table and the objective. 3D  $\text{Ca}^{2+}$  responses recorded

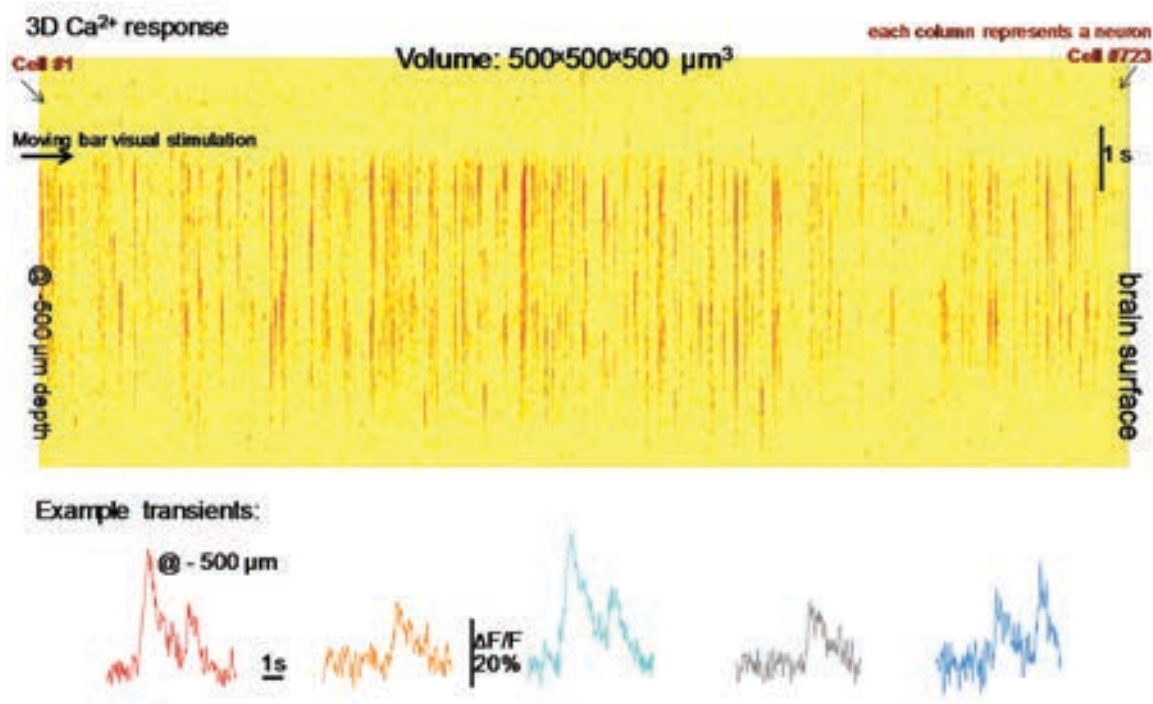


**Figure 7.** High-speed 3D random-access *in vivo* recording of 723 neurons that were simultaneously recorded. The exemplified transients demonstrated that the signal-to-noise ratio is preserved even at the bottom of the scanning volume (at  $-500 \mu\text{m}$  depth from the surface in this example). Calibration, 1 s.

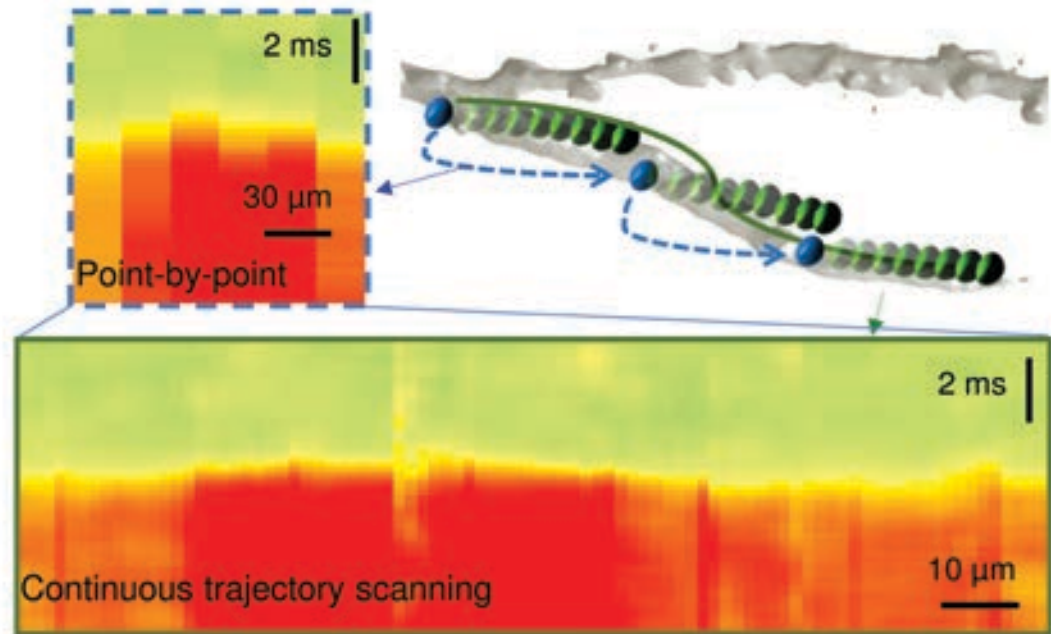


**Figure 8.** Point-by-point and continuous 3D trajectory scanning of dendritic segments. Top right, Schema of the scanning modes (blue point-by-point scanning; green, continuous scanning). Top left, Example of  $\text{Ca}^{2+}$  responses measured by point-by-point. Scale bar,  $30\ \mu\text{m}$ . Bottom, continuous trajectory modes. Traces were spatially normalized. Scale bar,  $10\ \mu\text{m}$ ; calibration, 2 ms. Reprinted with permission from Katona et al. (2012), their Fig. 3f.

simultaneously in multiple points can be plotted as curves (Fig. 6f, right panel), or alternatively, responses following spatial normalization can be shown as images (Fig. 6f, middle panel; Fig. 7).

#### Frame scanning in 3D

One of the basic measurement modes that can be realized with a 3D-AO microscope is frame scanning. In this mode, one can freely move or rotate arbitrary areas in 3D using the real (by moving the objective) and virtual (by focusing with the AODs at a fixed objective position)  $z$  for focusing. Because frame-scanning mode is relatively slow in 3D, this mode can be used to find and preselect ROIs for the subsequent fast 3D measurements. Multiple areas situated in multiple layers can be selected and measured simultaneously.

#### Multiple 3D trajectory scanning

Multiple 3D trajectory scanning mode was developed for simultaneously measuring multiple neuronal processes. There are two realizations of 3D trajectory scanning. In the continuous trajectory scanning mode, instead of jumping between preselected points (as during point scanning), one lets the focal spot drift along neuronal processes (Fig. 8). In this way, information is collected with a much higher spatial discretization within the same time interval.

#### XYZ or volume imaging

It is possible to capture volumetric data by successively capturing  $xy$  images at different  $z$  positions. The jump between the  $z$ -planes can be obtained by using either the real or the virtual focus. The first will result in better optical quality; therefore, it can be used at the end of experiments if only volume information is acquired. However, if one would like to perform fast 3D line scanning, 3D frame scanning, or random-access scanning, the  $z$ -stack should be obtained with virtual focusing in order to precisely preserve the coordinates of the cells for the fast 3D-AO scanning because the coordinate system of 3D-AO microscopes is distorted. Alternatively, a coordinate transformation is needed to match the two types of  $z$ -stacks to each other.

#### Movement correction

During long *in vivo* measurements, sample drifting can cause problems. Because in the random-access scanning paradigm one usually measures from a single point per cell or dendritic segment, the imaging quality can be very sensitive to sample movements. Quick timescale movements can be reduced only by preparation techniques. However, slow timescale drifts can be compensated for using software tools. For this compensation, reference objects are needed, which can consist of bright, well-defined objects in

the sample (Fig. 6c). These can be either a bright nonspecific object or a bright cell from which one does not expect activity-dependent fluorescence change. During compensation, one keeps the  $xyz$  center of this object in a given point inside the volume. Using this compensation method, a slow drift of the sample can be compensated for because, in this case, all points move together along the  $xyz$  coordinates; however, torsion of the sample cannot be compensated. In practice, this means that from one set of points, it is possible to take measurements for a couple of hours without significant drop in the image quality. This compensation can be performed manually or with software tools.

#### Automatic cell finding

In the simplest cases, cells can be categorized according to their dye content as measured by fluorescence, which is possible on multiple channels. In the most straightforward case, OGB1-AM and SR-101 dyes are bolus-loaded into the animal. In this technique, neuronal cells can be detected from their elevated green fluorescence and decreased red fluorescence. We normalize green and red fluorescent channel data from each image in the stack and then scale and shift them so that its 10th and 90th percentiles match 0 and 1. Background correction is done by oversmoothing an image and subtracting it from the original. Next, we subtract the red-channel data from the green and filter each layer of the stack again. The resulting stack is then searched for local maxima with an adaptive threshold. If two selected locations are closer than a given distance threshold, only one is kept.

In the algorithmically most complex cases, cell coordinates should be found according to their response to a (visual) stimulus (e.g., when using currently available channelrhodopsin [ChR] variants). In such cases, as a first step, random-access volume scanning is done on locations evenly spread over the field of view, sampling the space at approximately every 10  $\mu\text{m}$  so that one point is sampled from each cell. Visual stimulation is then presented to the animal to drive the normally silent cells and reveal their location. In a second step, a finer mesh is scanned around the active locations to more precisely outline the cell locations and their center.

#### Simultaneous cell-attached recording

The decay time of currently available calcium indicators is usually not fast enough in *in vivo* conditions to resolve bursts of action potentials (APs); single AP resolution is also problematic in most instances. However, the amplitudes of the  $\text{Ca}^{2+}$  peaks are proportional to the number of the APs. To measure this relationship, one needs to detect APs preferentially using juxtacellular recording, which is a relatively noninvasive method. Such measurements show that although the amplitude of the  $\text{Ca}^{2+}$  signal is linearly proportional to the number of APs, the proportion coefficient for the different dyes (and even for different loading levels) can be quite variable (Fig. 9). Similar variability can be detected in GCaMP6 animals.

#### 3D acousto-optical imaging of dendrites

The second main field of application for AO microscopes is dendritic imaging. This method can be used to measure propagation speeds; to simultaneously

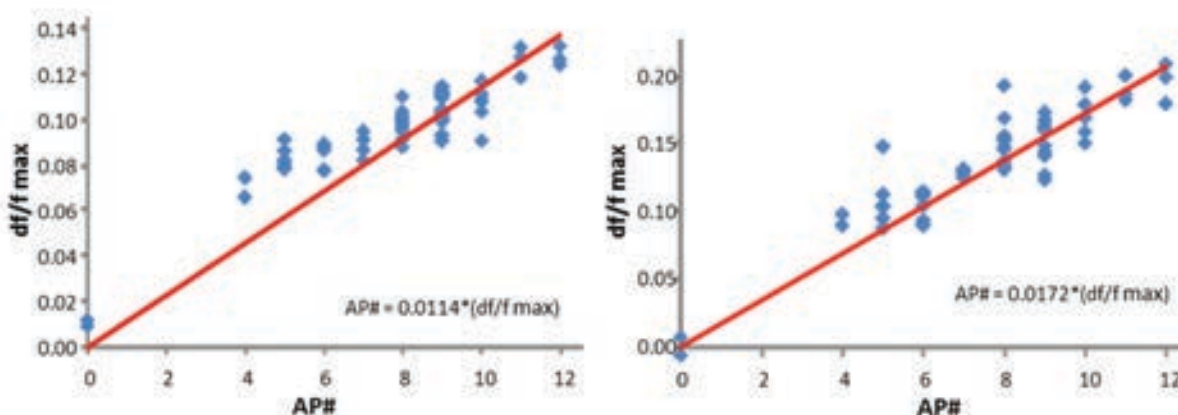


**Figure 9.** Maximum  $df/f_{max}$ -dependent AP number for two different cells in two different types of OGB bolus loading. Note the difference in the slope of the responses.

## NOTES

follow large-scale spontaneous dendritic events, such as sharp-wave-associated dendritic spikes in multiple dendritic segments (Chiovini et al., 2014); to study dendritic plasticity; or to measure dendritic spines *in vivo*. 3D fluorescence measurements and two-photon uncaging experiments in thin dendritic segments and spines are very sensitive to spatial misalignments because even displacements below the resolution limit can induce significant changes in responses. It is possible to compensate for these errors using high-resolution motion artifact compensation. Once a region for dendritic measurements has been identified, one can select two or more reference lines with high angular deviation that cross both the imaged and the neighboring bright dendritic structures. Fluorescence data are collected preferentially in the red channel. To compensate for tissue drift, one needs to repeatedly measure the spatial distribution of fluorescence along these reference lines; one should also minimize the discrepancy relative to the original distributions using cross-correlation, using either an automatic or a manual process. Alternatively, a set of reference points depicting fluorescent local maxima in the sample need to be selected at the beginning of the measurement and their  $x, y, z$ -coordinates continuously optimized during measurements in order to obtain the maximum average fluorescence level.

#### Measuring propagation speed along dendrites

Random-access AO scanning enables the measurement of, for example, fast-propagating calcium waves both along the dendrites (by measuring a few points relatively far from each other) and along the dendrites with fast temporal resolution. Cells need to be loaded with a high-concentration, low-affinity calcium sensor (Fluo-5F, 400  $\mu\text{M}$ ) in whole-cell

patch-clamp arrangement to perform measurements with good signal-to-noise ratio with fast onset times of the calcium events. In this example, we selected points along the dendritic tree of one pyramidal neuron in 3D (Fig. 9). We held the cell in current-clamp mode and evoked APs by somatic current injection. At the same time, we near-simultaneously measured dendritic  $\text{Ca}^{2+}$  signals associated with the backpropagating action potential (BAP) by repetitively scanning the selected 3D coordinates at several tens of kHz. We calculated the velocity of the BAP from the latency of the  $\text{Ca}^{2+}$  transients and the distance from the soma. Average BAP propagation speed differed at 23°C and 33°C ( $164 \pm 13 \mu\text{m ms}^{-1}$  [ $n = 9$ ] versus  $227 \pm 14 \mu\text{m ms}^{-1}$  [ $n = 13$ ];  $p = 0.006$ ,  $t$ -test, Fig. 10).

### Looking to the Future

Although the “hardware” for the AO microscope is nearing a theoretical maximum that can be realized with a given objective lens, there is a strong untapped potential in AO scanning still to be worked out:

- Developing novel software algorithms that could realize complex measurement modes;
- Applying the technology to larger FOV objectives;
- Developing novel correction methods for eliminating movement artifacts;
- Implementing adaptive optics;
- Improving lasers and fluorescent dyes to gain access to the entire thickness of the cortex;
- Simplifying the system to lower its costs and maintenance requirements;
- Improving wavelength tunability; and
- Providing simultaneous imaging and photostimulation in multiple regions.

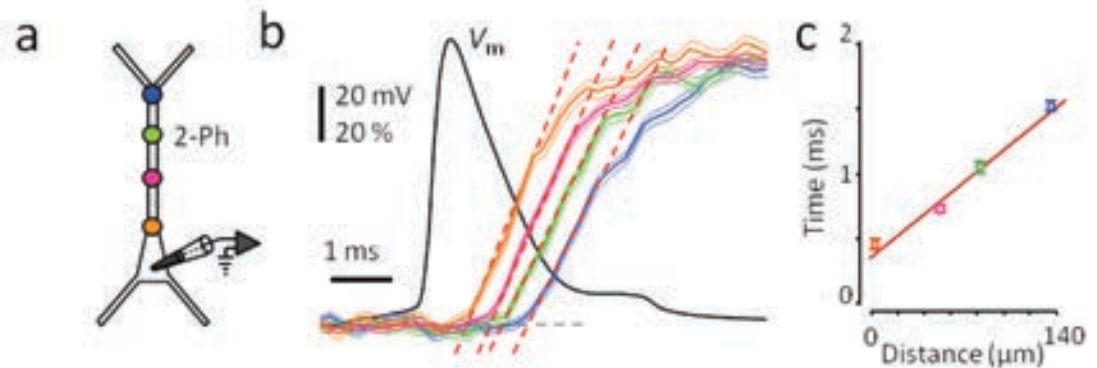


**Figure 10.** Measurement of propagation speed of BAP in apical dendrites. **a**, Experimental arrangement for signal propagation experiments. Signal propagation speed was measured by somatic whole-cell current-clamp ( $V_m$ , black) and 3D two-photon calcium imaging (orange, pink, green, and blue). **b**, AP peak triggered average of normalized dendritic  $\text{Ca}^{2+}$  transients induced by bAPs (mean  $\pm$  SEM;  $n = 54$ ; top). Linear fits (red dashed lines) define onset latency times. **c**, Onset latency times (mean  $\pm$  SEM;  $n = 54$ ) of  $\text{Ca}^{2+}$  transients in **b** as a function of dendritic distance. Linear fit = average propagation speed. Reprinted with permission from Katona et al. (2012), their Figs. 2c, d, g.

In addition to these improvements, 3D recordings will need to be performed in symbiosis with neuronal network and dendritic modeling; 3D recorded data must be explained by neuronal network and dendritic modeling; and, conversely, measurements must be performed according modeling predictions (Almog and Korngreen, 2014; Chiovini et al., 2014).

## Acknowledgment

Parts of this chapter were published in Katona et al. (2012), Fast two-photon *in vivo* imaging with three-dimensional random-access scanning in large tissue volumes. *Nat Methods* 9:201–208.

## References

- Almog M, Korngreen A (2014) A quantitative description of dendritic conductances and its application to dendritic excitation in layer 5 pyramidal neurons. *J Neurosci* 34:182–196.
- Botcherby EJ, Smith CW, Kohl MM, Debarre D, Booth MJ, Juskaitis R, Paulsen O, Wilson T (2012) Aberration-free three-dimensional multiphoton imaging of neuronal activity at kHz rates. *Proc Natl Acad Sci U S A* 109:2919–2924.
- Cheng A, Goncalves JT, Golshani P, Arisaka K, Portera-Cailliau C (2011) Simultaneous two-photon calcium imaging at different depths with spatiotemporal multiplexing. *Nat Methods* 8:139–142.
- Chiovini B, Turi GF, Katona G, Kaszas A, Palfi D, Maak P, Szalay G, Szabo MF, Szabo G, Szadai Z, Kali S, Rózsa B (2014) Dendritic spikes induce ripples in parvalbumin interneurons during hippocampal sharp waves. *Neuron* 82:908–924.
- Cotton RJ, Froudarakis E, Storer P, Saggau P, Tolias AS (2013) Three-dimensional mapping of microcircuit correlation structure. *Front Neural Circuits* 7:151.
- Fernandez-Alfonso T, Nadella KM, Iacaruso MF, Pichler B, Ros H, Kirkby PA, Silver RA (2014) Monitoring synaptic and neuronal activity in 3D with synthetic and genetic indicators using a compact acousto-optic lens two-photon microscope. *J Neurosci Methods* 222:69–81.
- Gobel W, Kampa BM, Helmchen F (2007) Imaging cellular network dynamics in three dimensions using fast 3D laser scanning. *Nat Methods* 4:73–79.
- Grewe BF, Voigt FF, van 't Hoff M, Helmchen F (2011) Fast two-layer two-photon imaging of neuronal cell populations using an electrically tunable lens. *Biomedical optics express* 2:2035–2046.
- Holekamp TF, Turaga D, Holy TE (2008) Fast three-dimensional fluorescence imaging of activity in neural populations by objective-coupled planar illumination microscopy. *Neuron* 57:661–672.
- Kaplan A, Friedman N, Davidson N (2001) Acousto-optic lens with very fast focus scanning. *Opt Lett* 26:1078–1080.
- Katona G, Kaszas A, Turi GF, Hajos N, Tamas G, Vizi ES, Rózsa B (2011) Roller Coaster Scanning reveals spontaneous triggering of dendritic spikes in CA1 interneurons. *Proc Natl Acad Sci U S A* 108:2148–2153.
- Katona G, Szalay G, Maak P, Kaszas A, Veress M, Hillier D, Chiovini B, Vizi ES, Roska B, Rózsa B (2012) Fast two-photon *in vivo* imaging with three-dimensional random-access scanning in large tissue volumes. *Nat Methods* 9:201–208.
- Nikolenko V, Watson BO, Araya R, Woodruff A, Peterka DS, Yuste R (2008) SLM Microscopy: Scanless Two-Photon Imaging and Photostimulation with Spatial Light Modulators. *Front Neural Circuits* 2:5.
- Proctor B, Wise F (1992) Quartz prism sequence for reduction of cubic phase in a mode-locked Ti:Al(2)O(3) laser. *Opt Lett* 17:1295–1297.
- Rózsa B, Katona G, Vizi ES, Varallyay Z, Saghy A, Valenta L, Maak P, Fekete J, Banyasz A, Szipocs R (2007) Random access three-dimensional two-photon microscopy. *Appl Opt* 46:1860–1865.
- Tomer R, Khairy K, Amat F, Keller PJ (2012) Quantitative high-speed imaging of entire developing embryos with simultaneous multiview light-sheet microscopy. *Nat Methods* 9:755–763.
- Vucinic D, Sejnowski TJ (2007) A compact multiphoton 3D imaging system for recording fast neuronal activity. *PLoS One* 2:e699.



# **Simultaneous Holographic Imaging of Neuronal Circuits in Three Dimensions**

Sean Quirin, PhD, Jesse Jackson, PhD,  
Darcy S. Peterka, PhD, and Rafael Yuste, MD, PhD

---

Department of Biological Sciences  
Columbia University  
New York, New York



## Introduction

In this chapter, we introduce a scanless optical method for simultaneously imaging neuronal activity in three dimensions (3D). Using a spatial light modulator and a custom-designed phase mask, we collect light simultaneously (as opposed to serially) from different focal planes and perform holographic calcium imaging of neuronal activity *in vitro* and *in vivo*. This method could be used as a technological platform for brain activity mapping.

Optical imaging of neural activity has several advantages over alternative strategies for monitoring neurons, such as patch electrodes and electrode arrays. First, it is minimally invasive and allows for the monitoring of large ensembles of neurons with single-cell resolution (Yuste and Katz, 1991). Also, it is compatible with a large variety of functional and chemical sensors (e.g., voltage indicators, calcium indicator, metabolic sensors), with genetically encoded indicators, and thus can be used for chronic imaging of genetically defined cell populations (Chen et al., 2013).

However, several key weaknesses remain for functional imaging of neuronal cell activity. First, from the very first microscope designed by A. van

Leeuwenhoek, image acquisition has been limited typically to a single plane, whereas nearly all interesting biological structures are 3D, requiring sequential scanning for volumetric imaging. Second, as a result of this sequential scanning, the sampling rate over the volume data is slow (normally a few Hz) relative to neuronal activity (1 kHz). Moreover, in highly scattering tissue, although two-photon excitation has afforded single-cell resolution and imaging below superficial layers (Horton et al., 2013), images are normally generated by serially scanning a single beam. More recent attempts have been made to circumvent this limitation (Gobel et al., 2007; Nikolenko et al., 2008; Cheng et al., 2011; Katona et al., 2012), but despite recent advances that increase the image acquisition speed, few proposed strategies are scalable toward meeting the challenge of fast, population voltage imaging with single-cell resolution in scattering tissue in 3D. Such a task would require milliseconds of temporal resolution across wide spatial areas (Alivisatos et al., 2012; Kralj et al., 2012).

## Volume Projection Imaging

As one solution to this problem, we propose here a scanless structured illumination microscope coupled to a custom imaging system with wavefront coding. This coded imaging system creates a projection of

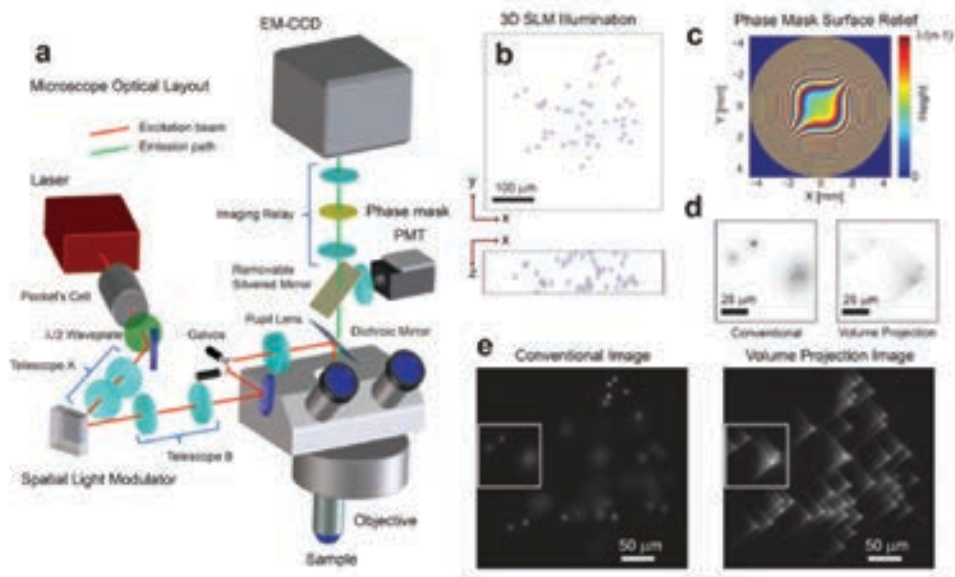


**Figure 1.** Optical path and characteristics of 3D projection-based imaging. **A**, The optical configuration comprises an illumination path which incorporates an SLM for 3D illumination and a modified imaging path using a phase mask to suppress the imaging effect of defocus. PMT, photomultiplier tube. **B**, An example 3D illumination pattern using a  $20\times/0.5\text{NA}$  objective. Scale bar,  $100\ \mu\text{m}$ . **C**, Ideal surface profile modulation of the phase mask. **D**, Experimental imaging results using a transparent fluorescent slab show that the volume projection imaging path results in clearer separation of the target signals when compared with the conventional imaging path. Note that the contrast conserves the number of photons in each image. Scale bars,  $25\ \mu\text{m}$ . **E**, Wide-field imaging results comparing the conventional and volume projection imaging techniques. Note that each image is normalized to the respective peak signal. Scale bars,  $50\ \mu\text{m}$ . Reprinted with permission from Quirin et al. (2014), their Fig. 1.

## NOTES

an extended sample volume onto a two-dimensional (2D) image plane and is therefore optimized for high-speed, 3D data acquisition. We use a phase-only spatial light modulator (SLM) to create multiple well-defined beamlets of light that illuminate many neurons in parallel (Nikolenko et al., 2008), and then use a phase mask to simultaneously acquire their fluorescence with a camera (Fig. 1a) in what we call Volume Projection Imaging (Quirin et al., 2013). In this technique, cells are not restricted to a single plane and can be freely distributed throughout the 3D sample (Fig. 1b).

While SLM-based multisite excitation has been coupled to wide-field microscopy before, it has been limited to 2D acquisition (Nikolenko et al., 2008; Packer et al., 2012). Although in some samples (transparent, or effectively sparse) single-photon excitation is sufficient, we regard two-photon capabilities as essential in turbid environments and for allowing precise modulation of activity when coupled with optogenetics or caged compounds (Packer et al., 2012).

Operationally, in our method, structural volume data are first acquired with a conventional two-photon microscope in order to identify the cells to be used for SLM targeting. We then generate a hologram that targets the regions of interest (ROIs) in the volume (Quirin et al., 2013) and image the functional activity of these ROIs simultaneously in 3D using a wavefront coded imaging system (e.g., a cubic phase mask) (Dowski and Cathey, 1995; Cathey and Dowski, 2002; Quirin et al., 2013). The deterministic illumination the SLM provides imparts a priori knowledge that can be used to extract additional information from the collected image, as explained below.

For simultaneous 3D signal acquisition, the wavefront coded imaging system enhances the standard shallow depth-of-field while maintaining the full aperture of the objective. This custom imaging system uses a phase-only optical mask in the imaging path to effectively null-defocus (Dowski and Cathey, 1995). This has the effect of greatly reducing the axial dependence of the point spread function (PSF) (i.e., the image is invariant to the 3D target position) and records an aberrated line-of-sight projection of the sample volume onto the image plane. This phase mask is described by the complex amplitude profile,

$$p(x,y) = e^{i2\pi\alpha(x^3 + y^3)}, \quad (1)$$

where we used values of  $\alpha = 17$  and  $12$  for  $M = 20\times/0.5\text{NA}$  and  $40\times/0.8\text{NA}$  objectives, respectively, and  $x$  and  $y$  are the normalized coordinates of the microscope pupil (Fig. 1c).

The trade-off for this defocus invariance is a decreased contrast in the focused image (Fig. 1d) (Cathey and Dowski, 2002; Quirin et al., 2013). As a result, the acquired wide-field image exhibits a characteristic blur (e.g., an aberrated Point Spread Function) that is now invariant regardless of the 3D location of the target (Fig. 1e). This blur is nonetheless spatially restricted, and reduction of the out-of-focus PSF size compared with traditional imaging allows for a much higher local spatial density of targeted ROIs (Fig. 1d). Now, 3D fluorescence signals can be simultaneously acquired without loss of contrast owing to out-of-focus collection (Fig. 1e). As an additional benefit, the data volume is projected onto a 2D image plane, thereby reducing the total data throughput required during acquisition. In principle, this image can be digitally restored to diffraction-limited resolution by use of deconvolution methods; however, these steps are not necessary here (Cathey and Dowski, 2002). Instead, we report results using simple functional signal extraction, as described in Materials and Methods.

## Demonstration of the Imaging Technique in Animals

### Mouse models

We first demonstrated the system capabilities using a calcium indicator in *in vitro* mouse hippocampus preparations. Sections of the dentate gyrus were selected for 3D imaging, because this brain structure, with its dense ensemble of cells, provides a challenging opportunity to demonstrate single-cell resolution (Fig. 2a). Recent work has demonstrated the presence and importance of functional cell-cluster activity in 2D imaging conditions of the hippocampus (Muldoon et al., 2013; Ramirez et al., 2013); however, these events have never been observed in 3D. We present here a representative result of the 3D structure, which was first acquired and then used to identify the targets (Fig. 2a). We subsequently targeted all visually identified cells with illumination beamlets by loading the associated hologram pattern on the SLM (Quirin et al., 2013).

In one demonstration, data were acquired for 107 such targets and recorded using an EM-CCD detector at 55 volume projection images per second (VPPS) (Fig. 2b). Individual fluorescence activity from a dense 3D cluster of cells demonstrated that unique signals from individual neurons can be extracted with high signal-to-noise ratio (SNR). Before and after one identified burst, independent activity was observed in each cell body regardless of 3D position, demonstrating cellular resolution. A key advantage of this method is that minute differences in the onset

timing and calcium dynamics can be resolved with high SNR, even at these high temporal sampling rates (Fig. 2C). In slices from older animals, with less dense labeling, we demonstrated this method at sampling rates up to 125 VPPS at single-cell resolution and with high SNR. Cofiring dentate gyrus cells could represent ensembles of hippocampus neurons involved in pattern separation (Muldoon et al., 2013; Ramirez et al., 2013). Our technique thus allows for the visualization of these memory patterns with unprecedented spatiotemporal precision.

### Larval zebrafish

We also report on the reconstruction of neuronal activity of the larval zebrafish (P7) with GCaMP5G (Akerboom et al., 2012; Ahrens et al., 2013) to map the temporal record of brainwide calcium transients at high speed *in vivo*. Different spatial scales can be accessed with our optical technique by simply selecting an alternative microscope objective or modulating the phase aberration present on the wavefront coding element at the pupil (via use of  $\alpha$ , in Eq. 1). As a reference illustration, we show conventional two-photon galvanometric scanning

images that contain brainwide activity patterns in which both individual cells and neuropil are recruited and fluoresce (Figs. 3a, e) (Ahrens et al., 2013). In recent work, the temporal resolution of such whole-brain activity mapping has been limited by the axial scan speed and the camera frame rate. In contrast, the technique proposed here has no moving parts, and therefore exhibits no mechanical acquisition speed limitation, nor the potential of coupling motion into the sample.

As a test case, 49 total target locations within a  $350 \times 350 \times 150 \mu\text{m}$  volume were selected. Using these targets, a custom hologram was created and loaded to the SLM (red targets, Fig. 3b). With the two-photon SLM illumination, multiple waves of calcium transients were precisely localized as they occurred at 30 VPPS. The monitored active cells in these waves were temporally sorted based on the activity in the first wave, and we observed that this ordering was preserved in subsequent waves, with subsecond precision, despite occurring many minutes later (Fig. 3c). Within the monitored cells, the spatial distribution of the activity was dispersed throughout the sample, with varying modulation strength (Fig. 3d). This is the first demonstration of simultaneous 3D calcium activity imaging in *in vivo* zebrafish preparations with single-cell precision at a temporal resolution sufficient to resolve the dynamics of synaptic activity patterns.

Although the larval zebrafish is transparent, many organisms are not. Our method, as implemented here, still relies on direct imaging and is adversely affected in highly scattering environments. This has been a challenge for all imaging methods in neuroscience, and the described method is not immune to it. We evaluated the effect of scattering on the PSF used here and believe that this method can be applied up to 2–3 scattering lengths deep, provided that a sparse selection of 3D points is used. However, with the active development of red-shifted indicators and light sources whose longer wavelengths penetrate more deeply through tissue, this method may allow for significant and sizable volumetric imaging with high spatial and temporal resolution. Additionally, with the development of faster SLMs, or additional modulation schemes, temporal multiplexing can be added to augment the selectivity at large imaging depths (Ducros et al., 2013). This could be a critical

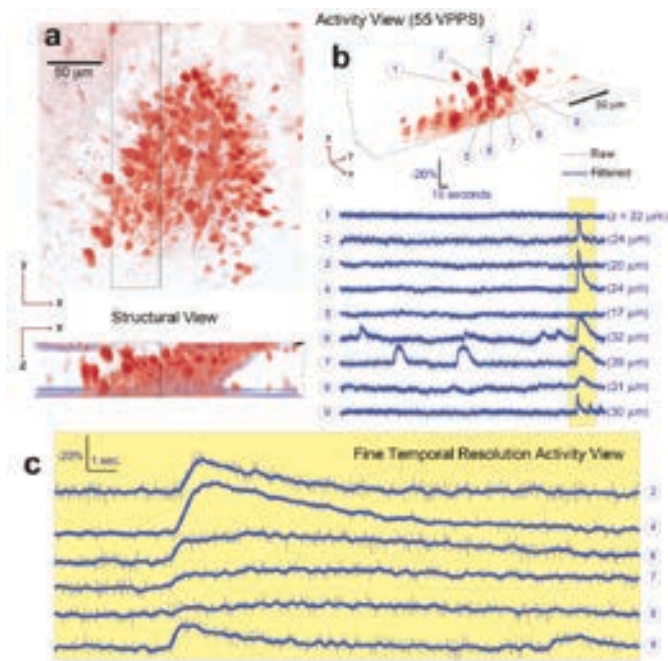


**Figure 2.** Simultaneous 3D imaging of hippocampal neuronal activity *in vitro* at 55 VPPS. **A**, 3D structural data acquired by two-photon scanning image stack. **B**, 3D imaging capability with single-cell resolution is demonstrated, where 9 of 107 total cells are selected from the 3D volume (boxed region in **A**) and their respective activity is given in **B**. Despite simultaneous burst activity in 5 of the neighboring cells, independent calcium transients were measured. The axial location of each cell is given in parenthesis behind the respective fluorescence trace. **C**, A fine-temporal resolution view of the burst activity highlights the variability in both the temporal and amplitude modulation of the calcium transients. Reprinted with permission from Quirin et al. (2014), their Fig. 3.

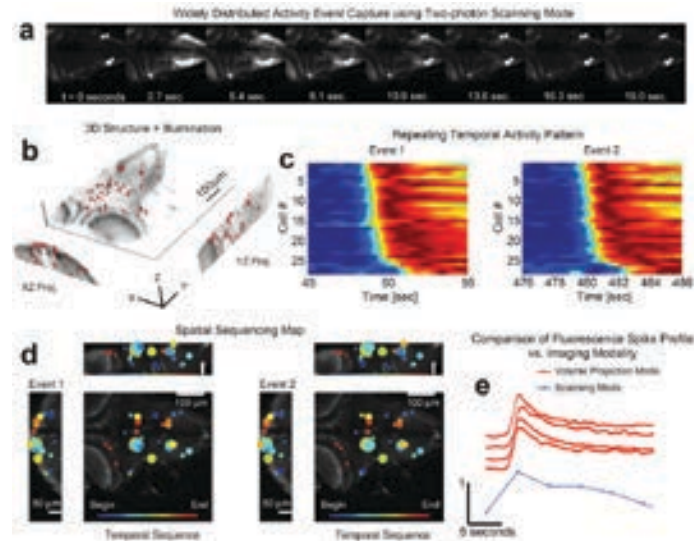


**Figure 3.** Simultaneous 3D imaging of calcium dynamics of zebrafish *in vivo* at 30 VPPS. **a**, Conventional single plane two-photon data acquisition reveals sequences of coordinated whole-brain activity. **b**, 49 targets are distributed throughout an acquisition volume of  $284 \times 270 \times 114 \mu\text{m}$  to sample activity in 3D. Scale bar,  $100 \mu\text{m}$ . **c**, Multiple repetitions of these events occur and exhibit similar time courses. **d**, The associated spatial patterns of the events confirm that the activity has repetitive structure. The size of the marker indicates the amplitude of signal modulation at each location. **e**, Comparison of the fluorescence spike profile time profile between the two imaging modalities shows the signal of the volume projection technique to be consistent with the two-photon scanning acquisition. The scanning mode data series was taken from the boxed area in **a**, while the four-volume projection mode series was taken from the  $x$ -marked areas. Note that the fluorescence signal has been normalized in each time series of **c** and **e** for visualization. Reprinted with permission from Quirin et al. (2014), their Fig. 7.

improvement, since it would allow for imaging neurons whose projections fall within the same pixels of the camera.

## Materials and Methods

### Animals

All animal experiments were performed in accordance with the regulations and guidelines of Columbia University and were approved by the institutional review board of Columbia University. Mice experiments were performed in C57BL mice aged P11–P60 using  $400\text{-}\mu\text{m}$ -thick coronal slices loaded with FURA-2AM. Zebrafish experiments were performed at ages P6–P8 and were performed in accordance with the regulations and guidelines of Columbia University. The zebrafish sample is held fixed within a bead of 2% low-melting point agarose to reduce motion artifacts.

### Setup

The structured-illumination microscope with volume projection imaging uses one laser line for exciting fluorescence of either the calcium indicator dye or genetically encoded calcium indicator (GECI). This laser line is output from a Coherent Mira-HP ( $\sim 140$  fs pulses, 80 MHz) (Coherent, Santa Clara, CA), which can be manually tuned to span an excitation wavelength from 770 nm

to 1100 nm. At  $\lambda = 800$  nm, the system provides 3.8 W, and at  $\lambda = 920$  nm, it provides 2.2 W. The output beam was steered through an electro-optic (EO) modulation device (ConOptics EO350-160, ConOptics, Danbury, CT). A broadband  $\lambda/2$  wave plate (Thorlabs AHWP05M-980, Thorlabs, Newton, NJ) was located after the EO modulator to rotate the polarization state to be parallel with the active axis of the SLM (XY-512 Spatial Light Modulator, Boulder Nonlinear Systems, Lafayette, CO) located downstream. An LS6Z2 shutter (Vincent Associates, Rochester, NY) was placed in the beam path in order to control illumination conditions. A 1:2 telescope ( $f_1 = 50$  mm,  $f_2 = 100$  mm; Thorlabs plano-convex lenses) scaled the optical beam to approximately fill the active area of the SLM (XY-512, Boulder Nonlinear Systems). The optical beam was redirected by a periscope to illuminate the SLM. The SLM has a custom lookup table that was experimentally determined at both wavelengths reported for use. The angle of incidence of the illumination beam to the SLM was  $\sim 10^\circ$ . A 4:1 telescope ( $f_3 = 300$  mm,  $f_4 = 75$  mm; Thorlabs plano-convex lenses) reduces the image of the SLM onto a set of galvanometer mirrors. The galvanometer mirrors are located conjugate to the microscope objective pupil of an Olympus BX51 microscope (Olympus America, Melville, NY) by use of an Olympus pupil transfer lens ( $f_5 = 50$  mm) and the mounted tube lens ( $f_{TL} = 180$  mm).

Two microscope objectives were tested in the manuscript: an Olympus 20×/0.5NA WI and an Olympus 40×/0.8NA WI objective. To operate in a two-photon scanning mode, Olympus Fluoview was used to control the galvos and image acquisition from a photomultiplier tube (PMT) (H7422P-40, Hamamatsu) located above the microscope. A removable silvered mirror (mounted in Thorlabs LC6W and LB4C) redirects the collected fluorescence emission into the PMT module. To operate in volume projection mode, custom software was developed for MATLAB (MathWorks, Natick, MA) to load the correct gamma map and generate a hologram with manually selected targets throughout the sample volume. When the illumination shutter is opened, the sample is illuminated with a custom pattern that is representative of where the targeted cell soma are located. For volume projection image acquisition, the silvered redirection mirror for the PMT is removed, and the fluorescence emission is passed through an optical relay system with a custom phase mask. The optical relay consists of a 1:1 telescope ( $f_{af} = 150$  mm, Thorlabs 2" achromatic doublets) with a custom-designed surface relief patterned onto a 1" diameter quartz plate, which is placed a distance  $f_{af}$  behind the first lens. Note that no amplitude modulation is necessary (i.e., the mask is transparent), which is critical for high-sensitivity imaging. Also note that in the following, the imaginary component describes the surface relief of the mask where

$$h(x,y) = \frac{\text{arg}(p(x,y))}{2\pi} \left( \frac{\lambda}{n-1} \right) \quad (2)$$

and where  $h$  is the height,  $p(x,y)$  is the complex function describing the pupil,  $\lambda$  is the emission wavelength, and  $n$  is the refractive index of the substrate (here, we used fused quartz with  $n = 1.462$  at  $\lambda = 515$  nm). The realized surface relief is representative of a discretized 8-level diffractive optic design of this profile with  $\alpha = 200$  over an 18 mm diameter and with an optimal  $\lambda \approx 505$  nm. An imaging detector (Andor iXon Ultra 897 electron-multiplying [EM] CCD, Andor Technology, Belfast, UK) is located in the imaging plane of the 1:1 relay system.

### Targeting calibration, image acquisition, and signal reconstruction

Precise targeting of the neuron cells was facilitated by a 3D calibration of the SLM projection patterns. A calibration phantom was created using a 2% agarose mixture with a dye solution (yellow highlighter dye) at a 1:1 ratio. Standard projection patterns were input to the SLM, and the captured fluorescence image was used at each  $z$  position to calculate an affine transformation from the SLM to the EM-

CCD. A third-order polynomial fit of each element from the axial-dependent affine matrix describing the axial evolution of the affine transform matrix was made and stored for later use. A pollen grain slide was used to calibrate the axial-dependent affine transformation from the EM-CCD image to the PMT image frame. The slide was translated through the volume range of interest, and an EM-CCD image and PMT image were acquired for comparison. An automated fitting routine estimated the axial-dependent affine transform matrix and, as was performed with the SLM to EM-CCD transform, a third-order polynomial fit was made to each element of the matrix. Matrix multiplication of the PMT to EM-CCD and the EM-CCD to SLM transforms yielded the coordinates to load onto the SLM for precise targeting.

Images acquired in volume projection mode on the imaging detector were processed using custom analysis software written in MATLAB (MathWorks, Natick, MA). Volume projection acquisition mode consists of generating the hologram illumination pattern, setting the EO modulator for appropriate illumination power, opening the shutter, and acquiring time-lapse images, which were stored as TIFs (image acquisition used an Andor Solis environment, Andor Technology). Because the neurons were relatively large compared with the imaging detector pixel size, pixel binning of  $4 \times 4$  was routinely used to improve SNR without any appreciable loss of spatial resolution performance. Using the targeting calibration matrices, the location of each target on the CCD was estimated and an experimentally measured PSF put in its place in order to form a basis set of images: one image for each target. Each frame from the time-lapse stack of images was decomposed into a linear superposition of this basis set using a least-squares fitting, plus one image for background estimation. Formally, this was accomplished by creating a matrix of  $N$  images,

$$B = \begin{bmatrix} (B_i(1) & \dots & B_N(1) \\ \dots & \dots & \dots \\ B_i(m * n) & \dots & B_N(m * n) \end{bmatrix} \quad (3)$$

where each column is one  $m \times n$  image, lexicographically ordered in a column, representative of the expected pattern from the target location (known from the deterministic illumination). In principle, these images can be given by simulation or found experimentally. Here, we used the experimentally determined PSF and built the library by stamping it at each target location. Given acquisition of the experimental image,  $I(t)$ , at time  $t$  and using

## NOTES

$$I(t) = \mathbf{B} \cdot \mathbf{W}(t) + \mathbf{n} \quad (4)$$

to describe the image formation, where  $\mathbf{n}$  is additive random noise, a least-squares fitting

$$\hat{\mathbf{W}}(t) = \min_{\mathbf{W}(t)} \|\mathbf{I}(t) - \mathbf{B} \cdot \mathbf{W}(t)\|^2 \quad (5)$$

quickly yields the individual fluorescence from each target,  $w_i(t)$ .

To control for systematic movements of the sample that could have been artificially interpreted as calcium transients, we ruled out the possibility of synchronous deflections in fluorescent transients in either direction. We also performed a positive movement test by gently tapping the sample stage, which resulted in the characteristic synchronous fluorescence signals.

## Conclusion

In conclusion, we have presented a technique for fast, simultaneous, two-photon optical data acquisition of neuron activity that is distributed throughout three dimensions. This has been demonstrated in multiple animal preparations, both *in vitro* and *in vivo*, that are relevant for neuroscience. Both the illumination and data acquisition are simultaneous and can target multiple ROIs throughout the volume of tissue, allowing for parallel activation and imaging. Advances in lasers and SLMs may enable more complex patterns, and faster cameras could accommodate direct imaging of voltage activity in 3D. Also, although we describe two-photon SLM-based multiple beamlet excitation here, any predetermined structured illumination could be used.

The combination of holographic illumination with volume projection imaging appears to us an ideal platform for future work on brain activity mapping.

## Acknowledgments

We thank Misha Ahrens and David Bennett for their help with the fish preparations and their comments on the manuscript. This work was supported by the National Eye Institute (DP1EY024503, R01EY011787), National Institute of Mental Health (R01MH101218), Defense Advanced Research Projects Agency (DARPA) contract W91NF-14-1-0269, and the Keck Foundation. This material is based on work supported by, or in part by, the U.S. Army Research Laboratory and the U.S. Army Research Office under contract number W911NF-12-1-0594 (Multidisciplinary University Research Initiative).

S. Q. and D. S. P. designed and built the microscope software and hardware. S.Q., J. J., D. S. P., R. Y. designed the mouse experiments. S. Q., and R. Y. designed the zebrafish experiments. S. Q. and J. J. performed the mouse experiments and analyzed data. S. Q. performed the zebrafish experiments. S. Q., D. S. P. and R. Y. wrote the paper. Parts of this chapter have been previously published in Quirin et al. (2014), Simultaneous imaging of neural activity in three dimensions, *Front Neural Circuits* 8:29.

## References

- Ahrens MB, Orger MB, Robson DN, Li JM, Keller PJ (2013) Whole-brain functional imaging at cellular resolution using light-sheet microscopy. *Nat Methods* 10, 413–420.
- Akerboom J, Chen TW, Wardill TJ, Tian L, Marvin JS, Mutlu S, Calderon NC, Esposti F, Borghuis BG, Sun XR, Gordus A, Orger MB, Portugues R, Engert F, Macklin JJ, Filosa A, Aggarwal A, Kerr RA, Takagi R, Kracun S, et al. (2012) Optimization of a GCaMP calcium indicator for neural activity imaging. *J Neurosci* 32:13819–13840.
- Alivisatos AP, Chun M, Church GM, Greenspan RJ, Roukes ML, Yuste R (2012) The brain activity map project and the challenge of functional connectomics. *Neuron* 74:970–974.
- Cathey WT, Dowski ER (2002) New paradigm for imaging systems. *Appl Opt* 41:6080–6092.
- Chen TW, Wardill TJ, Sun Y, Pulver SR, Renninger SL, Baohan A, Schreiter ER, Kerr RA, Orger MB, Jayaraman V, Looger LL, Svoboda K, Kim DS (2013) Ultrasensitive fluorescent proteins for imaging neuronal activity. *Nature* 499:295–300.
- Cheng A, Goncalves JT, Golshani P, Arisaka K, Portera-Cailliau C (2011) Simultaneous two-photon calcium imaging at different depths with spatiotemporal multiplexing. *Nat Methods* 8:139–142.
- Dowski ER, Cathey WT (1995) Extended depth of field through wave-front coding. *Appl Opt* 34:1859–1866.
- Ducros M, Houssen YG, Bradley J, de Sars V, Charpak S (2013) Encoded multisite two-photon microscopy. *Proc Natl Acad Sci USA* 110:13138–13143.
- Gobel W, Kampa BM, Helmchen F (2007) Imaging cellular network dynamics in three dimensions using fast 3D laser scanning. *Nat Methods* 4:73–79.

- Horton NG, Wang K, Kobat D, Clark C, Wise F, Schaffer C, Xu C (2013) *In vivo* three-photon microscopy of subcortical structures of an intact mouse brain. *Nat Photonics* 7:205–209.
- Katona G, Szalay G, Maak P, Kaszas A, Veress M, Hillier D, Chiovini B, Vizi ES, Roska B, Rózsa B (2012) Fast two-photon *in vivo* imaging with three-dimensional random-access scanning in large tissue volumes. *Nat Methods* 9:201–208.
- Kralj J, Douglass AD, Hochbaum DR, Maclaurin D, Cohen AE (2012) Optical recording of action potentials in mammalian neurons using a microbial rhodopsin. *Nat Methods* 9:90–95.
- Muldoon SF, Soltesz I, Cossart R (2013) Spatially clustered neuronal assemblies comprise the microstructure of synchrony in chronically epileptic networks. *Proc Natl Acad Sci USA* 110:3567–3572.
- Nikolenko V, Watson BO, Araya R, Woodruff A, Peterka DS, Yuste R (2008) SLM microscopy: scanless two-photon imaging and photostimulation with spatial light modulators. *Front Neural Circuits* 2:1–14.
- Packer AM, Peterka DS, Hirtz JJ, Prakash R, Deisseroth K, Yuste R (2012) Two-photon optogenetics of dendritic spines and neural circuits. *Nat Methods* 9:1202–1205.
- Quirin S, Peterka DS, Yuste R (2013) Instantaneous three-dimensional sensing using spatial light modulator illumination with extended depth of field imaging. *Opt Express* 21:16007–16021.
- Quirin S, Jackson J, Peterka DS, Yuste R (2014) Simultaneous imaging of neural activity in three dimensions. *Front Neural Circuits* 8:29.
- Ramirez S, Liu X, Lin P-A, Suh J, Pignatelli M, Redondo RL, Ryan TJ, Tonegawa S (2013) Creating a false memory in the hippocampus. *Science* 341:387–391.
- Yuste R, Katz LC (1991) Control of postsynaptic  $Ca^{2+}$  influx in developing neocortex by excitatory and inhibitory neurotransmitters. *Neuron* 6:333–344.



# **Local Circuit Analysis with Integrated Large-Scale Recording of Neuronal Activity and Optogenetics**

György Buzsáki

---

The Neuroscience Institute and Center for Neural Science  
New York University School of Medicine  
New York, New York



## Introduction

Numerous methods, such as macroscopic and microscopic imaging, molecular biological tools, and pharmacological manipulations, are available to study brain activity. However, all these indirect observations eventually should be converted back into a common currency—the format of neuronal spike trains—to understand the brain's control of behavior. Specific behaviors emerge from the interaction of neurons and neuronal pools. Studying these self-organized processes requires simultaneous monitoring of the activity of large numbers of individual neurons in multiple brain regions at the speed of neuronal communication in the behaving animal. Therefore, a major goal is to record from statistically representative samples of identified neurons from several local areas and to interact with them to probe their contribution to circuit function and behavior.

Local circuit analysis depends on three critical components: (1) neuron–electrode interface hardware for large-scale recording of neuronal activity, (2) effective spike-sorting methods, and (3) identification and targeted perturbation of specific neuronal types (Fig. 1). This chapter will present large-scale recording and analysis methods combined with focal optogenetic perturbations that can achieve these goals.

## Recording from Single and Multiple Single Neurons

Action potentials produce large transmembrane potentials in the vicinity of their somata. As a result, they can be sensed by placing a conductor (such as a saline-filled glass micropipette or the bare tip of an insulated wire) in proximity to a neuron (Fig. 2). Because neurons of the same class (e.g., pyramidal cells) generate identical action potentials, the only way to identify a given neuron from extracellularly recorded spikes is to move the electrode tip closer to its body ( $<20\ \mu\text{m}$  in cortex) than to any other neuron.

In general, there are three problems with this spike-amplitude-based approach using “sharp” electrodes. First, moving the electrode too close to the neuron affects its biophysical and firing properties. This is a particularly difficult problem in freely moving animals because even slight movement of the head may affect the discharge pattern. The second problem is related to the first: Because of electrode instability, long-term recordings from the same neurons are not practical with single “sharp” electrodes placed close to a single neuron. The third problem is the difficulty of simultaneously recording from large number of cells. For each neuron, a separate electrode is needed, resulting in excessive tissue damage. Because most anatomical wiring in the cortex is local, the majority of neuronal interactions, and thus computation, occurs in a small volume. In the cortex, this “small volume”

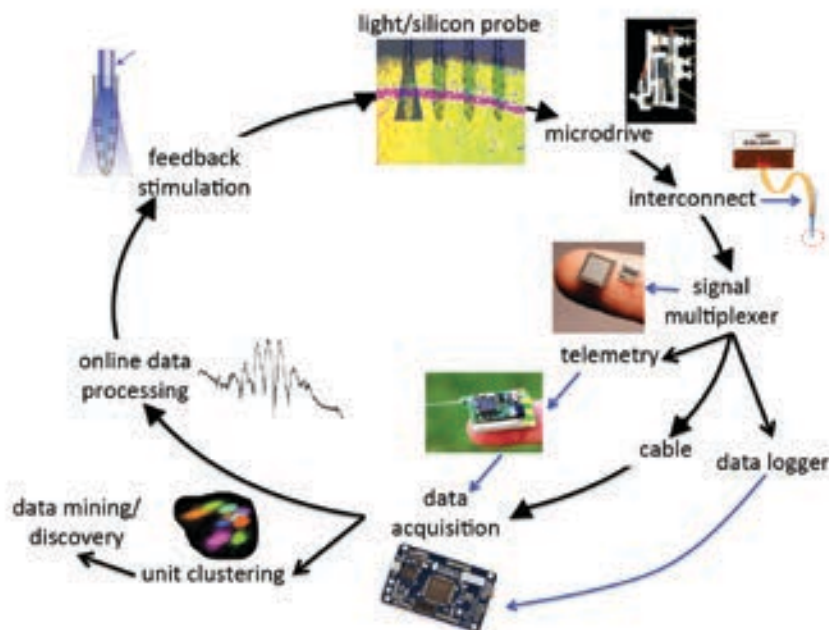


**Figure 1.** Flow chart showing components for large-scale recording of unit and LFP data, combined with optogenetic tagging of neurons and closed-loop perturbation of their activity for circuit analysis.

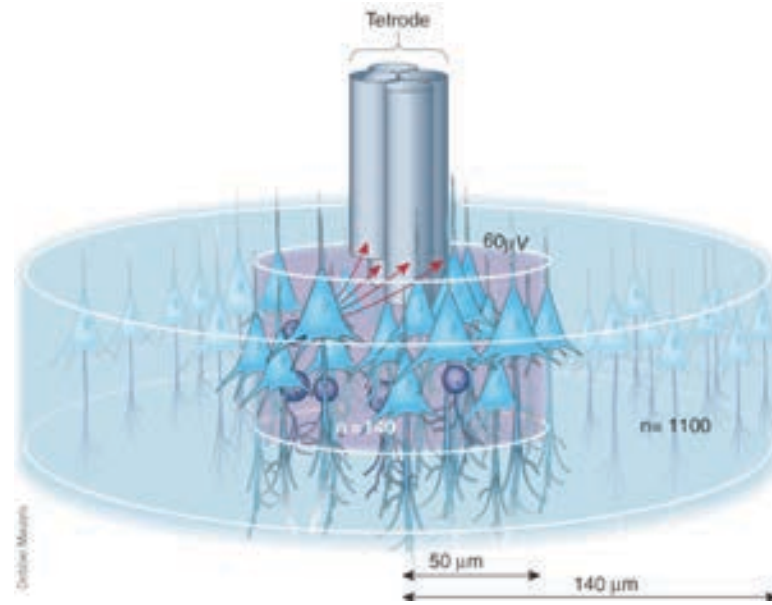


**Figure 2.** Unit isolation quality varies as a function of distance from the electrode. Multisite electrodes (e.g., wire tetrode) can estimate the position of the recorded neurons using triangulation. Distance of the visible electrode tips from a single pyramidal cell (triangles) is indicated by arrows. The spike amplitude of neurons ( $>60 \mu\text{V}$ ) within the gray cylinder ( $50 \mu\text{m}$  radius), containing  $\sim 100$  neurons, is large enough for separation using available clustering methods. Although the extracellularly recorded spike amplitude decreases rapidly with distance, neurons within a radius of  $140 \mu\text{m}$  (containing  $\sim 1000$  neurons in the rat cortex) can be detected. Improved recording and clustering methods are therefore expected to record from larger number of neurons in the future. Reprinted with permission from Buzsáki (2004), his Fig. 1.

corresponds to hypothetical cortical modules with mostly vertically organized layers of principal cells and numerous interneuron types. For example, in a cylinder of cortical tissue with a diameter corresponding to the extent of the dendritic tree of a pyramidal cell, hundreds to several thousand of other neurons cell bodies are located. Understanding such local computation requires improved methods that would allow for simultaneous recording of representative members of this closely spaced community but with minimal damage to neurons and wiring.

### Unit Isolation by Triangulation

Monitoring neurons from a distance has a major advantage: stability. A disadvantage is that with only one recording site, signals from many neurons that are the same distance from the tip provide the same magnitude signal, making single-cell isolation difficult. The use of two or more recording sites allows for the triangulation of distances because the amplitude of the recorded spike is a function of the distance between the neuron and the electrode (Fig. 2). Often, this task is accomplished with four spaced wires (dubbed “tetrodes”). Ideally, the tips are separated in three-dimensional space so that unequivocal triangulation is possible in a volume. Unfortunately, in practice the wires are cut flat, providing only two-dimensional (2D) monitoring of neurons, usually perpendicular to the main dipole generated by the action potential.

Cortical pyramidal cells generate extracellular currents that flow mostly parallel to their somadendritic axis. Nevertheless, tetrodes can “hear” hippocampal CA1 pyramidal cells as far as  $140 \mu\text{m}$  lateral to the cell body, although the extracellular spike amplitude decreases rapidly as a function of distance from the neuron. A cylinder with this radius contains  $\sim 1000$  neurons, which is the number of theoretically recordable cells by a single tetrode. Even so, in practice, only 5–15 neurons can be reliably separated using available algorithms. The remaining neurons may be damaged by the electrode, are silent, or are too small in amplitude, thus preventing reliable separation with only four monitoring sites. Nevertheless, wire tetrodes have numerous advantages over sharp-tip single electrodes, including a larger yield of units, low-impedance recording tips, and mechanical stability.

### Recording with Silicon Probes

An ideal recording electrode has a very small volume, so tissue injury is minimized. A wire electrode has only one useful part: the conductive tip; the rest consists of just ohmic conductor and inconvenient bulk. However, recording from large number of neurons with many tetrodes is possible only at the expense of extensive cell damage. The desire for large-scale monitoring of neurons from a small volume competes with the tissue damage inflicted by the electrodes.

Micro-Electro-Mechanical Systems (MEMS)–based recording devices can reduce the technical limitations inherent in wire electrodes because, by using the same amount of tissue displacement, the number of monitoring sites can be substantially increased. Whereas silicon probes keep the advantages of tetrode recording principles, they are substantially smaller. Further, multiple sites can be arranged over a longer distance, allowing for the simultaneous recording of neuronal activity in the various cortical layers. Six- to 8-shank probes with 8–32 sites on each probe can record from >100 well-separated neurons (Fig. 3). Because the geometrical distribution of the recording sites is known, the spatial relationship of the isolated single units can be determined. This latter feature is advantageous for studying the spatiotemporal representation and transformation of inputs by neuronal ensembles. Ideally, every part of a probe surface placed in the brain should have monitoring sites. However, this possibility is limited mainly by the width of the interconnect between the recording tips and the extracranial connector (although with the advent of signal multiplexers and on-chip active circuits, substantial volume and weight reduction can be achieved).

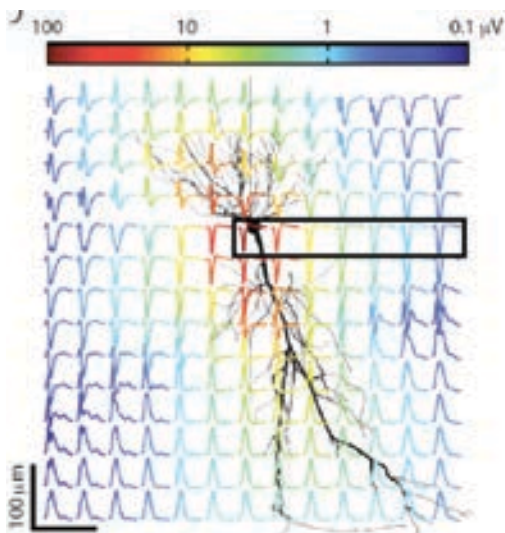


**Figure 3.** Extracellular contribution of an action potential (“spike”) to the LFP in the vicinity of the spiking hippocampal CA1 pyramidal cell. The peak-to-peak voltage range is indicated by the color of the traces. Note that the spike amplitude decreases rapidly with distance from the soma, without a change in polarity within the pyramidal layer (approximately the boxed area), in contrast to the quadrupole (i.e., reversed polarity signals both above and below the pyramidal layers) formed in the somatodendritic axis. Reprinted with permission from Buzsáki et al. (2012), their Fig. 2*d*.

A further advantage of silicon probes is their ability to sample the extracellular current effectively (Fig. 4). A requirement for understanding the transformation of inputs by a neuron or neuronal assemblies is information about both their input and output. Unfortunately, no simple method is available for monitoring all inputs at the resolution of dendrites and spines of single neurons in behaving animals. However, membrane currents generated by neurons pass through the extracellular space. These currents then can be measured by electrodes placed outside the neurons. The local field potential (LFP, or more correctly, the mean local voltage) recorded at any given site reflects the linear sum of numerous overlapping fields generated by current sources (current from the intracellular space to the extracellular space) and sinks (current from the extracellular space to the intracellular space) distributed along multiple cells. LFP measurements, combined with recording of neuronal discharges, are an efficient tool for studying the influence of cytoarchitectural properties (e.g., cortical lamination, distribution, size, network connectivity) of neural elements on electrogenesis. However, a large number of observation points, combined with decreased distance between the recording sites, is required to achieve high spatial resolution and for interpreting the underlying cellular events. Recording the voltage gradients by geometrically arranged sites of silicon probes allows current densities to be calculated in order to estimate the mean input to the neuron group in the recorded volume.

### Isolation and Identification of Neurons by Extracellular Signatures

An indispensable step in spike-train analysis is the isolation of single neurons on the basis of extracellular features. Spike-sorting methods fall into two broad classes. The first class attempts to separate spikes on the basis of amplitude and waveform variation; the second, triangulation method separates units on the basis of their spatial location. Unfortunately, neither method is satisfactory. When neurons are strongly activated, their amplitude, rise time, decay time, and spike width change as a function of both the membrane potential before the spike and the immediate firing history of the neurons. The spike amplitude variation is most substantial during complex spike-burst production, with as much as 80% amplitude reduction, primarily because of  $\text{Na}^+$  channel inactivation. Therefore, amplitude and waveform-based classification programs will separate action potentials from a single neuron as if they were emitted by many. The amplitude and waveform variability of the extracellularly recorded spike is the major cause of unit isolation errors.

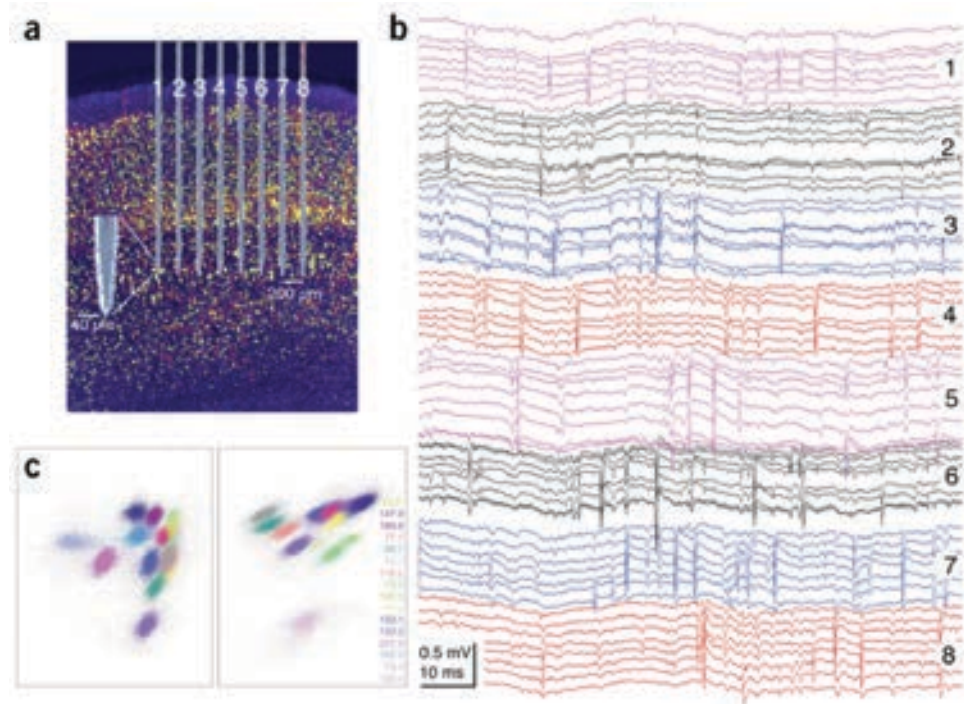


**Figure 4.** High-density recording of unit activity in the somatosensory cortex of the rat. *a*, Placement of an 8-shank silicon probe in layer 5. The 8 recording sites at the edges of the tip (inset) are connected to the extracranial electronics via 2  $\mu\text{m}$  interconnects. Scale bars, 200  $\mu\text{m}$  and 40  $\mu\text{m}$ . *b*, A short epoch of raw recording, illustrating both field and unit activity (1 Hz–5 kHz). Note the presence of spikes on several sites of the same shank (color-coded) and the lack of spikes across the different shanks, indicating that electrodes placed  $\geq 200$   $\mu\text{m}$  laterally record from different cell populations. *c*, 2D views of unit clusters (out of 28 possible views from an 8-site probe) from one shank. Clusters are color-coded. Numbers on right in *c* represent “isolation distance”; i.e., larger numbers indicate better neuron isolation. Reprinted with permission from Buzsáki (2004), his Fig. 2.

The second, triangulation approach is based on the tacit assumption that the extracellularly recorded spikes emanate from point sources. However, every part of the neuronal membrane is capable of generating action potentials, and what is observed in the extracellular space results from the complex geometry of neuron and spike propagation within the neuron. The extent of the somadendritic back-propagation of the action potential varies as a function of the excitatory and inhibitory inputs impinging on the neuron, as well as the state of various other conductances. The spike recorded in the extracellular space sums up the integrated signals from both soma and large proximal dendrites. Thus, the extent of somadendritic spike back-propagation can affect the estimation of the neuron’s virtual “point source” location and may place the same neuron at different locations, resulting in omission errors of unit isolation.

A further problem with the point-source assumption for action potentials is that the somatic origin is not always resolvable with distant recording sites. For example, in the rat neocortex, extracellular spikes can be recorded from the apical shaft of layer 5 pyramidal neurons as far as 500  $\mu\text{m}$  from the cell body. As a consequence, electrodes placed in layer 4, for example, can equally

record from layer 4 cell bodies or apical dendrites of deeper neurons. Large neurons in the primate cortex are especially prone to such misclassification errors because their spikes can be recorded from several hundred micrometers from the cell bodies.

To a large extent, these sources of unit separation errors can be reduced by recording at multiple sites parallel with the axodendritic axis of the neurons. However, most triangulation methods visually analyze 2D projected datasets simultaneously. With multiple site-recorded data, successive comparisons of the various possible projections generate cumulative errors of human judgment. As a result, a major motivation behind the development of efficient automatic clustering methods of high-dimensional data is to eliminate cumulative human errors.

The geometrically defined recording sites of silicon probes have additional advantages because, in addition to the output spikes, they can record the mesoscopic LFP signal that reflects the cooperative nature of input and synchronous activity of nearby neurons. With high enough density of recording sites, the afferents to the neurons can be precisely identified in architecturally regular structures (Fig. 5).

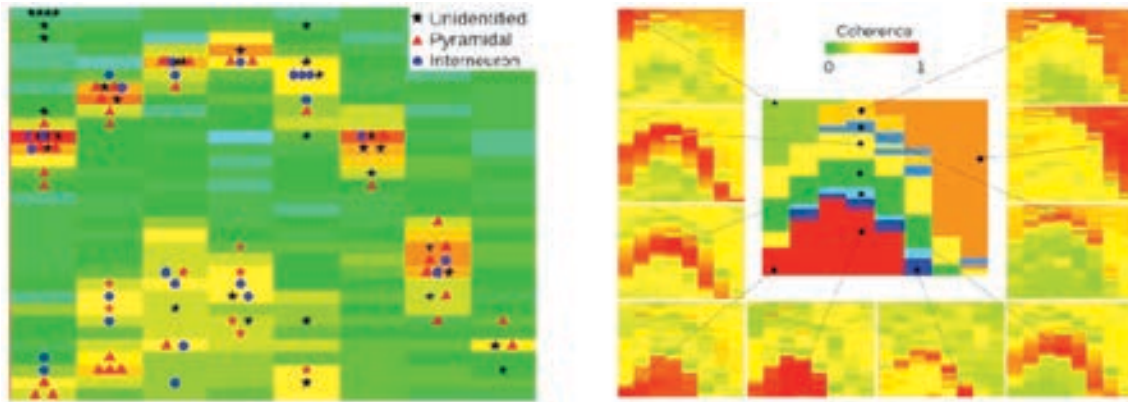


**Figure 5.** Generation of extracellular field potentials. Left, Distribution of high-frequency power ( $300 \pm 10$  Hz) outlines the cell body layers of the hippocampus. The  $32 \times 8$  color matrix represents the power values on the 256 sites of the silicon probe. Each rectangle represents a  $300 \mu\text{m}$  (intershank distance)  $\times$   $50 \mu\text{m}$  (vertical intersite distance) area to mimic the 2D geometry of the probe coverage of the CA1 and dentate areas. Clustered neurons, assigned to the largest amplitude recording sites, are superimposed on the power map. Right, outer squares: Coherence maps of gamma activity (30–90 Hz). The 10 example sites (black dots) served as reference sites, and coherence was calculated between the reference site and the remaining 255 sites. Note how gamma coherence effectively outlines dendritic layers. Middle, composite figure of the combined coherence and power maps. Recordings were made from a freely behaving rat during foraging. Reprinted with permission from Berényi et al. (2014), their Fig. 5.

## Local Circuit Analysis Using Combined Silicon Probe Recordings and Optogenetics

After isolating single neurons, the units should be classified into known cell groups of the cortex. This is a very important requirement because cortical networks consist of several neuronal classes, each having a specific computation task. Such classification will greatly improve the interpretation of hard-earned physiological data. The recent advent of optogenetics offers a solution for identifying specific, genetically defined neuronal subtypes in blind extracellular recordings by expressing light-sensitive opsins in a given neuronal population. Both activation and silencing strategies can be used for this purpose while implementing transgenic or virus infection methods. One important task for local circuit analysis is the simultaneous monitoring of all light-responsive neurons near the recording electrodes and estimating the fraction of the optogenetically responsive neurons (Royer et al., 2012; Stark et al., 2012). Integrated recording–optogenetic methods can be used to accomplish at least three goals:

- (1) Identifying genetically labeled neurons (optical “tagging”),
- (2) Characterizing and classifying neuron types physiologically, and
- (3) Testing the causal roles of the identified neurons on the performance of local circuits.

Because neurons are both embedded in circuits and contribute to circuit function, perturbing them can bring about secondary changes that need to be separated from the primary action of optical stimulation. A major problem with most available methods for identifying neurons and analyzing local circuits arises from the use of large-diameter optical fibers for brain surface illumination at high light power. Such technical problems can be significantly reduced by etching small-core ( $\leq 50 \mu\text{m}$ ) optical fibers to a point ( $\leq 10 \mu\text{m}$ ) and mounting them close ( $< 40\text{--}50 \mu\text{m}$ ) to the recording sites (Fig. 6). Hybrid devices that combine silicon probes with etched optical fibers allow the use of extremely low-power stimulation, eliminate photoelectric artifacts, and reduce artificially induced overlapping spikes. Experiments have shown that  $< 5 \mu\text{W}$  of light ( $\leq 0.1 \text{ mW/mm}^2$ ) is sufficient to activate ChR2-expressing neurons *in vivo*. Synchronous spiking can be minimized by using sinusoid or Gaussian waveform stimulation, as opposed to pulses. That is because neurons that express different amounts of opsins and experience different intensities at varying distances from the light source are expected to have variable thresholds for spike generation and, therefore, respond at shifting phases of the light stimulus.

The low light-intensity requirement can eliminate the need for benchtop lasers and optical cables that restrain the freedom of the animal’s movement. Instead, miniature light emitting diodes (LEDs) and/or laser diodes can be coupled to short, small-diameter ( $50 \mu\text{m}$ ) multimode fibers and attached directly to the shanks of

## NOTES

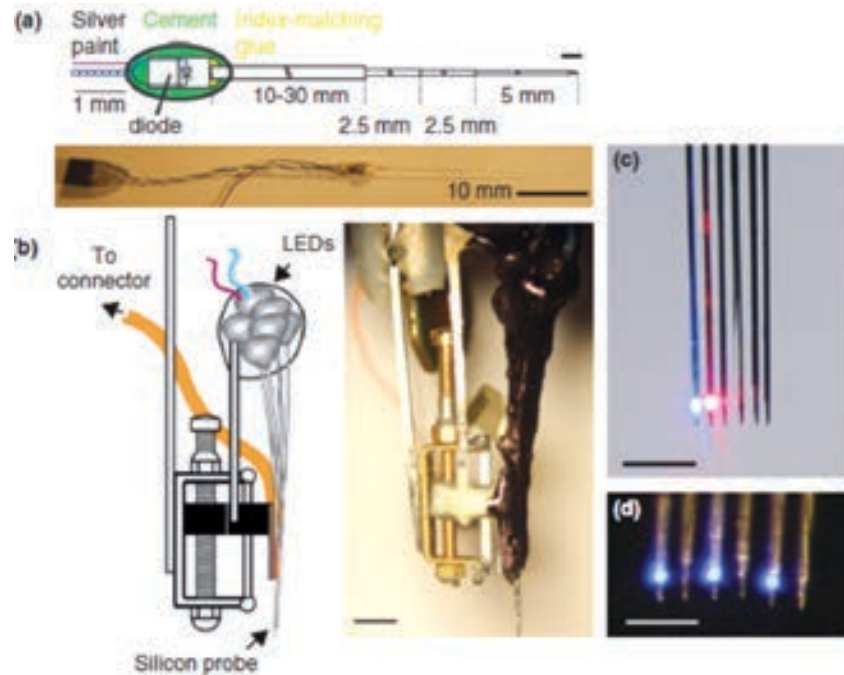


**Figure 6.** Diode probes for optogenetically identifying interneurons. *a*, Schematic of a single LED-fiber assembly. The LED is coupled to a 50 mm multimode fiber, etched to a point at the distal (brain) end. Scale bar, 10 mm. *b*, Left, Schematic of a drive equipped with a 6-shank diode probe with LED-fibers mounted on each shank. Etched optical fibers are attached ~40 mm above the recordings sites on the silicon probe shanks. Right, Picture of the drive depicted on the left. Scale bar, 3 mm. *c* and *d*, Local delivery of light. Magnified frontal view of the 6-shank diode probe equipped with diode-coupled optical fibers. *c*, Two adjacent shanks are illuminated with blue and red light. Scale bar, 1 mm. *d*, 3 shanks are illuminated with blue light. Scale bar, 0.5 mm. Reprinted with permission from Roux et al. (2014), their Fig. 1.

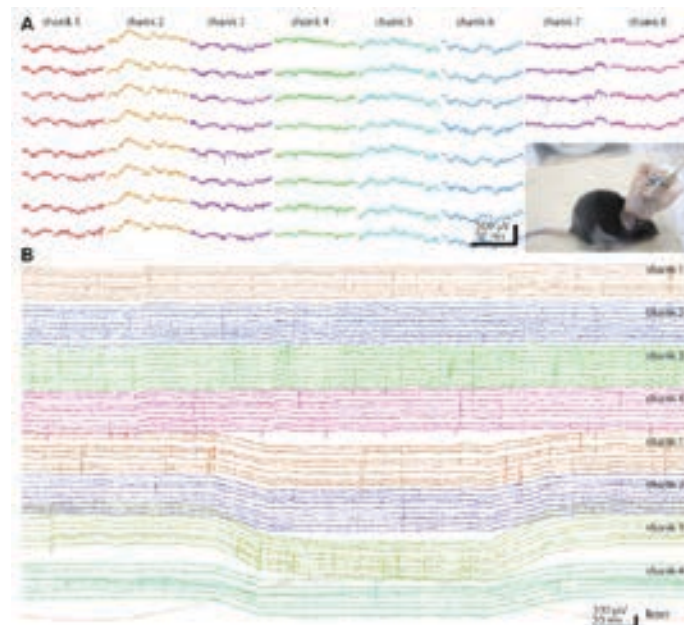


**Figure 7.** Unit and LFP recordings from the mouse. *A*, Chronic recordings from a mouse using an 8-shank 64-site silicon probe (diode probe). 100 ms epochs from each shank are shown. Inset: head stage with silicon probe, microdrive, and 64-channel signal multiplexer, surrounded by copper mesh shielding. The freely moving mouse is connected to the equipment by an ultra-flexible cable. *B*, Two 4-shank, 32-site probes were placed in the nucleus accumbens (top shanks 1–4) and ventral tegmental area (VTA; bottom shanks 1–4) in a TH-Cre;Ai32 mouse, expressing ChR2 in tyrosine hydroxylase-expressing neurons. One of the shanks in the VTA also contained an optical fiber for light delivery. Note VTA neuronal responses to 472 nm (bottom red trace) laser light stimulation. Reprinted with permission from Berenyi et al. (2014), their Fig. 13.

a silicon probe or tetrode (Fig. 6). The small size and light weight of these integrated “diode probes” (1.0–2.5 g) enable fast, multisite, and multicolor optogenetic manipulations in freely moving animals with concurrent monitoring of the manipulated neurons (Fig. 7).

In addition to optogenetics, numerous classification schemes based on a variety of physiological criteria have been developed to assign extracellular spikes to putative interneurons and pyramidal cells and their putative subtypes. These include waveform

features, firing rate statistics in different brain states, embeddedness in various population activities, firing patterns characterized by their autocorrelograms, and putative monosynaptic connections to other neurons. However, the “ground truth” of these classifying methods is essentially missing. An important goal of the optogenetic approach is to assist in the identification of distinct subtypes of neurons within individual, molecularly identified classes. However, in a single experiment, optogenetic methods can assist in the identification of only one or

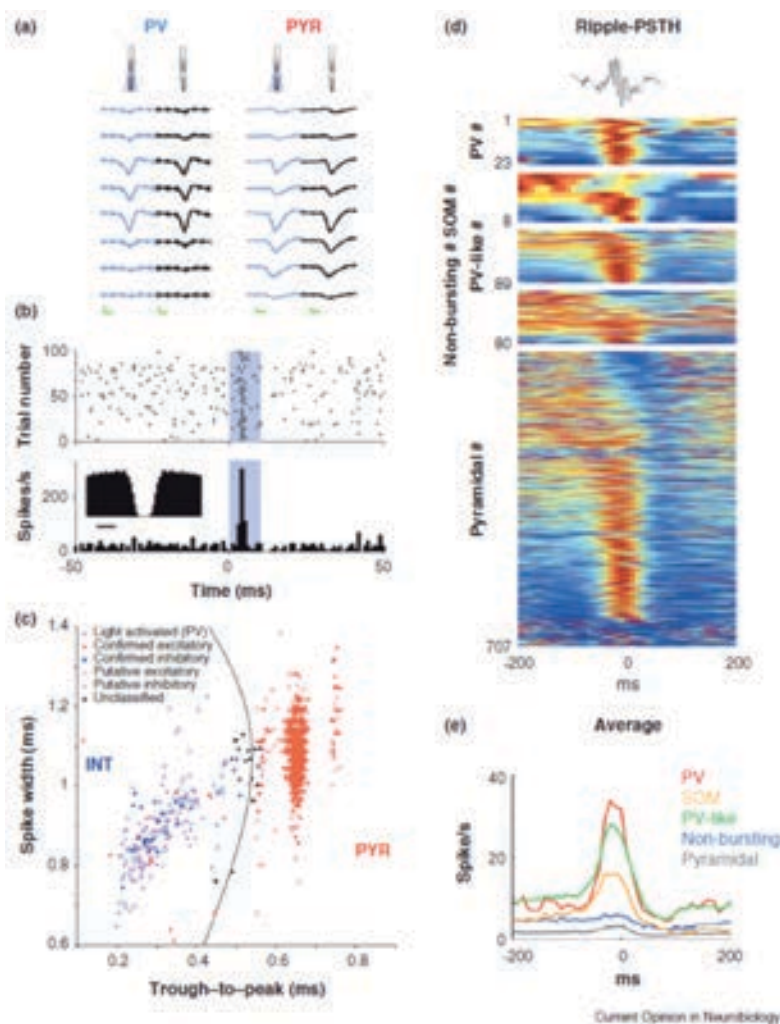


**Figure 8.** Optogenetic identification of interneurons. *a*, Right, Unfiltered spontaneous (black) and light-induced (blue) waveforms of a parvalbumin-expressing interneuron (PV) and a pyramidal cell (PYR) at 8 recording sites. Note the similarity of the waveforms with and without illumination. Mean and SD; calibration, 0.25 ms, 50  $\mu$ V. *b*, Diode-probe-induced unit firing in the hippocampal CA1 region (blue shaded area superimposed on the raster plot [top] and the histogram [bottom]; 4 mW at fiber tip). Inset: Autocorrelogram shows a shape typical for fast-spiking PV interneurons. *c*, Clustered units are tagged as excitatory or inhibitory on the basis of monosynaptic peaks/troughs in cross-correlation histograms (filled blue and red symbols) and/or response to locally delivered 50–70 ms light pulses (filled violet symbols) in transgenic mice expressing ChR2 in PV cells. Untagged units (empty symbols) are classified as putative excitatory pyramidal cells (PYRs) or inhibitory interneurons (INTs) according to waveform morphology; untagged units with low classification confidence are also shown in black (“unclassified”). *d*, Optogenetic identification of interneuron classes, including here PV-expressing and somatostatin (SOM)-expressing interneurons, allows studying their relationships to network patterns such as sharp-wave ripple events. Top, Single ripple. Each row represents the color-coded peri-ripple histogram of the firing rate computed for individual neurons. PSTH, peristimulus time histogram. *e*, Average firing rate observed for the different cell categories (PV, SOM, PV-like, nonbursting, and pyramidal). Reprinted with permission from Royer et al. (2012), their Supplementary Figs. 5a–d.

## NOTES

two neuron types. To be able to identify more diverse components of circuits, an iterative refinement of a library of physiological parameters is needed so that, subsequently, the various neurons can be recognized reliably by using purely physiological criteria without the need for optogenetics (Fig. 8).

Dramatic reduction in light intensity, combined with dense recording of the surrounding neurons, allows one to perform single-neuron stimulation and to estimate the absolute numbers of directly driven neurons in a small illuminated volume. Being able to assess the fraction of neurons that can affect a particular physiological pattern, perception, memory, or overt behavior is an important goal of circuit analysis.

## References

*Extensive and excellent technical reviews, written by various experts in the field, are available for further reading, most of which are listed below.*

- Berényi A, Somogyvári Z, Nagy AJ, Roux L, Long JD, Fujisawa S, Stark E, Leonardo A, Harris TD, Buzsáki G (2014) Large-scale, high-density (up to 512 channels) recording of local circuits in behaving animals. *J Neurophysiol* 111:1132–1149.
- Buzsáki G (2004) Large-scale recording of neuronal ensembles. *Nat Neurosci* 7:446–451.
- Buzsáki G, Anastassiou CA, Koch C (2012) The origin of extracellular fields and currents—EEG, ECoG, LFP and spikes. *Nat Rev Neurosci* 13:407–420.
- Gold C, Henze DA, Koch C, Buzsáki G (2006) On the origin of the extracellular action potential waveform: a modeling study. *J Neurophysiol* 95:3113–3128.
- Harris KD, Henze DA, Csicsvari J, Hirase H, Buzsáki G (2000) Accuracy of tetrode spike separation as determined by simultaneous intracellular and extracellular measurements. *J Neurophysiol* 84:401–414.
- Hazan L, Zugaro M, Buzsáki G (2006) Klusters, NeuroScope, NDManager: a free software suite for neurophysiological data processing and visualization. *J Neurosci Methods* 155:207–216.
- Henze DA, Borhegyi Z, Csicsvari J, Mamiya A, Harris KD, Buzsáki G (2000) Intracellular features predicted by extracellular recordings in the hippocampus *in vivo*. *J Neurophysiol* 84:390–400.
- Roux L, Stark E, Sjulson L, Buzsáki G (2014) *In vivo* optogenetic identification and manipulation of GABAergic interneuron subtypes. *Curr Opin Neurobiol* 26C:88–95.

Royer S, Zemelman BV, Losonczy A, Kim J, Chance F, Magee JC, Buzsáki G (2012) Control of timing, rate and bursts of hippocampal place cells by dendritic and somatic inhibition. *Nat Neurosci* 15:769–775.

Stark E, Koos T, Buzsáki G (2012) Diode probes for spatiotemporal optical control of multiple neurons in freely moving animals. *J Neurophysiol* 108:349–363.



